REPORT NO. FAA-RD-73-112,I

NORTH ATLANTIC (NAT) AIDED INERTIAL NAVIGATION SYSTEM SIMULATION

Volume I: Technical Results

William C. Hoffman
Walter M. Hollister
Kenneth R. Britting

JULY 1973

FINAL REPORT

Prepared for
DEPARTMENT OF TRANSPORTATION
FEDERAL AVIATION ADMINISTRATION
Systems Research and Development Service
Washington DC 20590

TECHNICAL REPORT STANDARD TITLE PAGE

1. Report No.	2. Government Accession No.	3. Recipient's Catalog No.
FAA-RD-73-112,I		

4. Title and Subtitle
NORTH ATLANTIC (NAT) AIDED INERTIAL NAVIGATION SYSTEM SIMULATION. Volume I: Technical Results

5. Report Date
July 1973

6. Performing Organization Code

7. Author(s)
*William C. Hoffman, Walter M. Hollister, Kenneth R. Britting

8. Performing Organization Report No.
DOT-TSC-FAA-73-23, I

9. Performing Organization Name and Address
Aerospace Systems, Inc.
One Vine Brook Park
Burlington MA 01803

10. Work Unit No.
FA314/R3144

11. Contract or Grant No.
DOT-TSC-473-73-1

12. Sponsoring Agency Name and Address
Department of Transportation
Federal Aviation Administration
Systems Research and Development Service
Washington DC 20590

13. Type of Report and Period Covered
Final Report
June 1972 to January 1973

14. Sponsoring Agency Code

15. Supplementary Notes
*Under Contract to: Department of Transportation
Transportation Systems Center
Kendall Square
Cambridge MA 02142

16. Abstract
Current air traffic operations over the North ATlantic (NAT) and the application of hybrid navigation systems to obtain more accurate performance on these NAT routes are reviewed. A digital computer simulation program (NATNAV — North ATlantic NAVigation) is developed to evaluate the performance of navigation systems for future commercial NAT aircraft operations. Error models are developed for aided-inertial navigation systems with external measurements from Doppler radar, Omega, satellite-ranging or air data. The covariance matrix error analysis method is used to simulate the navigation error histories, using the recursive navigation technique to incorporate measurements. A 34th-order error state vector is defined, requiring the numerical integration of up to 585 independent, first-order differential equations to propagate the covariance matrix. NATNAV has a highly modular structure for maximum flexibility to analyze a variety of likely hybrid navigation system configurations, to allow for contingencies such as subsystem failures and blunders, and to enable evaluation of variable update rates, suboptimal filtering schemes, aircraft maneuvers, etc. The program provides for an optimum initial alignment of the INS prior to taxi. A dead-reckoning option; i.e., no INS, is also available. Independent measurements using Doppler radar, Omega or satellite-ranging may be used to update the position and velocity estimates using the optimum recursive Kalman filter. As an alternative, suboptimum filter gains may be used instead. The outputs of the simulation are the standard deviations of the position and velocity errors, resolved into along-track, cross-track and vertical components. A number of computer results are presented for a typical eastbound North Atlantic flight. These results illustrate the performance of unaided-inertial systems; dead-reckoning; inertial systems with Omega, Doppler or satellite-ranging updates; sub filtering; and example malfunctions or blunders.

17. Key Words
Simulation; Computer Program; Navigation; Error Analysis; North Atlantic Air Traffic; Kalman Filtering; Inertial Navigation System; Doppler; Omega; Satellite-Ranging; Air Data.

18. Distribution Statement

19. Security Classif. (of this report)	20. Security Classif. (of this page)	21. No. of Pages	22. Price
Unclassified	Unclassified	204	

PREFACE

This report was prepared by Aerospace Systems, Inc. (ASI), Burlington, Massachusetts, for the Department of Transportation under Contract No. DOT-TSC-473. The study was sponsored by the Traffic Programs Division of the Transportation Systems Center (TSC), Cambridge, Massachusetts. Mr. Gilbert A. Gagne served as Technical Monitor on the contract.

This is the first volume of the two-volume final report which documents the results of research performed during the contract period June 1972 to January 1973. Volume I is the final technical report; Volume II is a user's manual for the digital computer simulation program NATNAV.

The effort was directed by Mr. John Zvara, President and Technical Director of ASI. Mr. William C. Hoffman served as Principal Investigator. Dr. Walter M. Hollister and Dr. Kenneth R. Britting, both in the Department of Aeronautics and Astronautics at the Massachusetts Institute of Technology (MIT), contributed to the study as technical consultants and co-investigators. Dr. Robert W. Simpson, Director of the MIT Flight Transportation Laboratory, and Dr. Arthur E. Bryson, Jr., Chairman, Department of Aeronautics and Astronautics, Stanford University, also served as technical consultants.

The authors are indebted to Mr. James Hauser, of the Naval Research Laboratory (NRL) Electromagnetic Propagation Branch, for his assistance during the final implementation of the program on the NRL CDC-3800 computer. We are also grateful to the staff of the NRL Research Computation Center for their support and cooperation.

LIST OF TABLES

TABLE OF CONTENTS

TABLE OF CONTENTS (Cont.)

TABLE OF CONTENTS (Cont.)

LIST OF FIGURES

LIST OF FIGURES (Cont.)

LIST OF FIGURES (Cont.)

NOMENCLATURE

a	=	local speed of sound
$b_{(\ )}$	=	random bias or scale factor error in indicated measurement
c	=	sensitivity of g to latitude
d_{wn}, d_{we}	=	correlation distances of north and east wind uncertainties
f	=	flattening of reference earth ellipsoid
f_N, f_E, f_D	=	north, east and down components of specific force
f_{ij}	=	i-th row, j-th column element of F
g	=	gravitational force per unit mass
g_e	=	equatorial, sea level reference value of g
h	=	altitude above reference earth ellipsoid
$\underline{h}$	=	measurement vector for covariance matrix update
h_a	=	barometric altimeter altitude
h_i	=	INS indicated altitude
k	=	propagation speed of light, 983.567 ft/μsec
ℓ	=	terrestrial longitude
$m, m_{(\ )}$	=	value of indicated external measurement
$n_{(\ )}$	=	colored noise in indicated measurement

$\underline{q}$	=	forcing vector of inertial system errors
r	=	magnitude of geocentric radius vector to aircraft
$^{r}(\;)$	=	white noise in indicated measurement
r_e	=	equatorial Earth radius
t	=	elapsed time
t_{cr}	=	time of reaching cruise conditions
$\underline{u}$	=	unit vector along satellite-ranging line of sight
u_N, u_E, u_D	=	north, east and down components of $\underline{u}$
$(u)[\;]$	=	uncertainty in indicated quantity
$^{v}(\;)$	=	driving white noise of indicated colored noise
$\underline{w}$	=	vector of white noises
$^{w}(\;)$	=	additive white noise
x	=	along-track position coordinate
$\underline{x}$	=	error state vector
y	=	cross-track position coordinate
$\underline{y}$	=	state vector of INS attitude and position errors
A	=	9×13 matrix; see Equation (33)
B	=	9×9 matrix; see Equation (34)
C_{ij}	=	i-th row, j-th column of matrix C_p^n

C_e^n	=	transformation matrix from earth to navigation coordinates
C_p^n	=	transformation matrix from platform to navigation coordinates
D	=	13 × 13 matrix; see Equation (35)
E	=	13 × 10 matrix; see Equation (36)
F	=	system response matrix
G	=	system forcing matrix
I	=	identity matrix
$\underline{K}$	=	vector of measurement filter gains
K_N, K_E, K_D	=	INS gyrocompassing gains
$\underline{K}_{opt}$	=	vector of optimum filter gains
L	=	latitude
M	=	Mach number
P	=	$<\underline{x}\,\underline{x}^T>$ = error covariance matrix
Q	=	diagonal matrix of driving white noise strengths
R	=	random measurement error variance
$\underline{R}^e_{EP}, \underline{R}^e_{ES}$	=	geocentric position vectors to aircraft and satellite, in earth coordinates
$\underline{R}^n_{PS}$	=	line-of-sight range from aircraft to satellite in navigation coordinates
V	=	velocity

V_a	=	airspeed
V_g	=	groundspeed
V_w	=	wind speed
V_N, V_E	=	north and east components of V_g
V_{wn}, V_{we}	=	north and east components of V_w
α	=	covariance of measurement
$\alpha_x, \alpha_y, \alpha_z$	=	exponentially-correlated accelerometer uncertainties
$\beta_x, \beta_y, \beta_z$	=	correlation distances of geodetic uncertainties
γ	=	0 for 3-accelerometer INS; 1 for 2-accelerometer INS
δ	=	wind correction angle
$\delta_x, \delta_y, \delta_z$	=	exponentially correlated gyro drift errors
$\delta(t)$	=	Dirac delta function
$\delta[\ ]$	=	error in indicated quantity
$\underline{\epsilon}$	=	state vector of INS attitude, position and velocity errors
$\epsilon_N, \epsilon_E, \epsilon_D$	=	north, east and down INS platform misalignment angles
η	=	east deflection of local vertical
θ_w	=	wind direction
κ	=	inertial altitude weighting parameter
λ	=	celestial longitude

υ = phase velocity of Omega signals, 986.123 ft/μsec

ξ = north deflection of local vertical

ρ = geodesic distance between Omega transmitter and receiver

σ = standard deviation of indicated error

τ = correlation time

θ_{Ai}, θ_{Bi} = azimuth angles to Omega stations for i-th line of position measurement

τ_x, τ_y, τ_z = gyro torquer scale factor errors

$\tau_h, \tau_{\dot{h}}$ = altimeter and rate of climb indicator scale factor errors

$\tau_{(\ )}$ = correlation time of indicated colored noise

ϕ = INS platform heading angle

χ = ground track angle of nominal flight path

ψ = heading angle

$\omega_x, \omega_y, \omega_z$ = components of $\underline{\omega}^p_{ip}$

$\tilde{\omega}_N, \tilde{\omega}_E, \tilde{\omega}_D$ = INS gyrocompass torquing commands

ω_s = Schuler frequency

ω_{ie} = Earth rotation rate

$\underline{\omega}^p_{ip}$ = INS platform torquing rate

Δg = magnitude of gravitation anomaly

Δt_a	=	INS alignment time
Δt_t	=	taxi time
$\Delta G_{(\ )}$	=	components of geodetic uncertainties
Λ	=	generalized INS characteristic matrix

Subscripts

a	=	actual error quantities in malfunction/blunder situation
a_x, a_y, a_z	=	INS accelerometers
aln, ale	=	north and east alignment
cl	=	climb phase
cr	=	cruise phase
fwd, side	=	forward and side Doppler radar measurements
g_x, g_y, g_z	=	INS platform gyros
h	=	barometric altimeter
m	=	measured value
n	=	nominal value
0	=	initial value
s1, s2	=	first and second satellite-ranging measurements
wn, we	=	north and east wind components
x, y, z	=	components in INS platform frame

A, B	=	Omega stations for each line of position
INS	=	inertial navigation system
N, E, D	=	components in navigation frame (north, east, down)
P	=	aircraft
S	=	satellite
$\Omega 1, \Omega 2$	=	first and second Omega line-of-position measurements

<u>Miscellaneous</u>

$\hat{[\ ]}$	=	estimated value
$\langle[\ ]\rangle$	=	expected value
$[\ ]^T$	=	transpose of matrix or vector
$[\ ]^+$	=	value after incorporating a measurement
$\dot{[\ ]}$	=	time derivative
$\underline{[\ ]}$	=	vector quantity

SECTION 1

INTRODUCTION

A parallel track routing structure is presently in effect for commercial aircraft operating across the North ATlantic (NAT). The tracks, centered about a weather-dependent Minimum Time Track (MTT), are assigned on a twice daily basis. The air traffic controller specifies a particular track to each aircraft entering the enroute region. Aircraft safety is maintained by assigning large separations between tracks and between aircraft in the tracks such that, in the absence of any positive control, the probability of collision between proximate aircraft is kept within acceptable limits.

The anticipated increase in traffic density has generated pressure to expand the capacity of the track routing structure; however, economic considerations associated with operation of the system preclude any expansion of the total area encompassed by the structure. Consequently, means must be found to increase capacity of the present track structure without adversely affecting acceptable collision risk levels. The desired result can be achieved by use of higher accuracy guidance and navigation aids such as augmented inertial navigation systems, satellite surveillance and positive Air Traffic Control (ATC) systems. Accordingly, the quantitative impact of such systems on all aspects of the capacity-cost-safety tradeoff must be thoroughly researched and analyzed.

The objective of this program has been the development of a digital computer simulation program NATNAV (NAT NAVigation) for evaluating the performance of various aided-inertial navigation system configurations which might be used by commercial aircraft operating in the North Atlantic region. Aided-inertial navigation/guidance systems have the inherent capability of providing multi-mode performance through use of independent position fix updating. By simulating these multi-mode navigation/guidance systems, Program NATNAV provides the information needed for subsequent analyses relating achievable performance of feasible navigation system configurations to ATC separation standards and collision risk.

This report presents the analysis techniques and mathematical models which are implemented in Program NATNAV. Volume II of this report (Ref. 1) is a user's manual for NATNAV, which is separately bound for convenience. It contains a complete discussion of the organization and programming details of NATNAV, instructions for the operation of the simulation and suggestions on possible applications of the program.

To provide more background on the problem, Section 2 describes the present mode of commercial aircraft operations over the North Atlantic routes. Section 3 then discusses some theoretical and practical aspects of hybrid aircraft navigation systems. The covariance error analysis technique and the use of Kalman filtering to update the error covariance matrix are presented in Section 4; the error models for the inertial navigation system (INS), Doppler radar, Omega, satellite-ranging and air data (dead-reckoning) are described in Section 5. Section 6 contains a brief description of the simulation program NATNAV. A number of results obtained with the program for various navigation system configurations are presented in Section 7. The principal conclusions from the study are summarized in Section 8, along with several recommendations for future research. A list of References follows Section 8. An extensive Bibliography which contains literature on various aspects of North Atlantic operations, hybrid navigators, optimum filtering, error models and error propagation is also included. Finally, Appendix A gives latitude and longitude expressions for constant track angle.

SECTION 2

NORTH ATLANTIC OPERATIONS

This section discusses several aspects of commercial aircraft operations across the North Atlantic to provide a background for the simulation of aided-inertial navigation systems. The present procedures of NAT air traffic planning and control are described, and a linearized model is developed for the simulation.

2.1 NORTH ATLANTIC ROUTES

North Atlantic traffic is distributed over a number of main routes shown in Figure 1. The total traffic is subject to considerable seasonal variation with

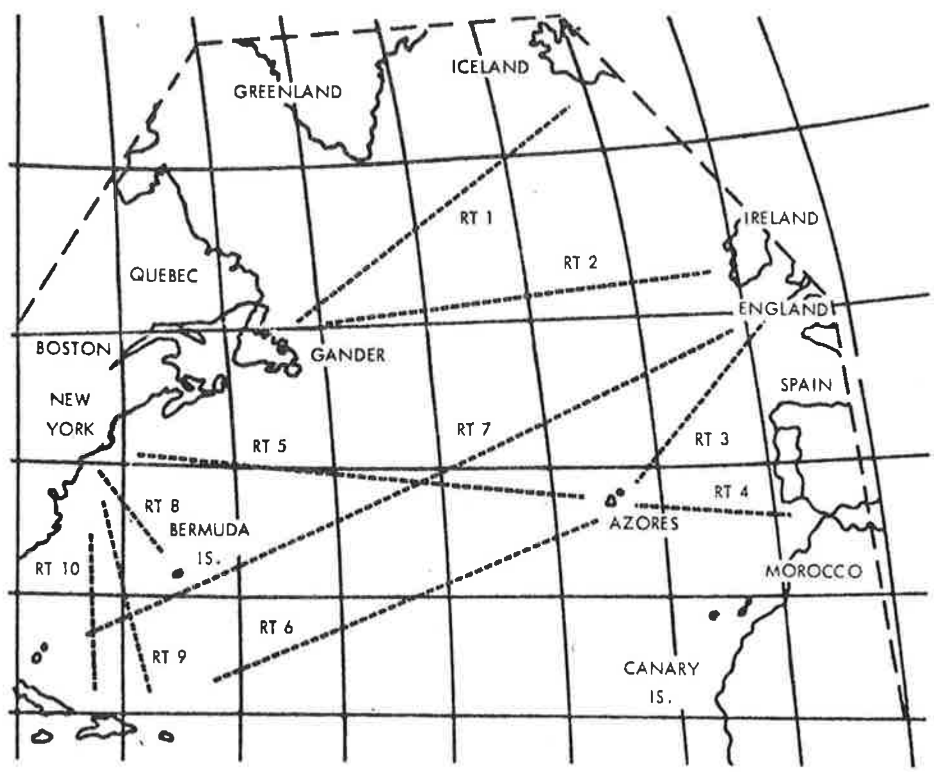

Figure 1. Main North Atlantic Routes.

the peak occurring in July and August. During these two months several hundred aircraft are handled each day, representing about 25 percent of the annual total flights. The traffic flow is nearly unidirectional with the eastbound flow peaking between 0400 and 0600 Z (Greenwich time) and the westbound flow peaking between 1500 and 1700 Z. An example of the weekly distribution of the traffic over the main routes (Figure 1) is presented in Table 1 (Ref. 2). The heavy concentration of traffic

Table 1. Traffic Distribution Over North Atlantic Routes (for the summer of 1969).

Route	No. of Flights
1	160
2	2,900
3	60
4	120
5	625
6	175
7	57
8	346
9	975
10	680

on certain routes, particularly Route 2, may be seen from this table. These peak traffic situations provide the motivation for reducing separation standards to increase capacity while maintaining high levels of safety.

Routing of air traffic over the above tracks is governed by the principle of minimum interference with the intent of the pilot. In general, this dictates that the pilot should be cleared on his requested route, unless that route conflicts with the assigned or requested routes of others. Thus, in lightly traveled areas it is relatively easy to route air traffic. In areas of heavy traffic, however, the task requires various conflict checks and aircraft are frequently required to take routes other than those requested. Consequently, the most heavily traveled routes of the North Atlantic have been organized into a system of parallel tracks designed to ease the controllers' job of assigning conflict-free paths, and to provide more efficient use of the airspace.

Today's system of organized parallel tracks handles approximately 500 flights on a peak day, with a peak hourly flow near 50. The present lane separation standards for the NAT region are (Ref. 3):

- Lateral separation — 120 nautical miles (nm)
- Longitudinal separation — 15 minutes
- Vertical separation — 2,000 feet

Although International Civil Aviation Organization (ICAO) standards officially allow a lateral separation of 90 nm, this distance is not implemented (Refs. 4, 5 and 6) in practice. The longitudinal separation criteria for a faster jet following a slower one requires three minutes additional separation at the oceanic entry fix for each Mach 0.01 speed difference. The jet traffic operating in the NAT area today consists primarily of DC-8's and 707's, which cruise at Mach 0.82, and 747's which have an optimum cruise speed of Mach 0.84. As a result, during peak traffic periods the 747 frequently gets penalized by assignment to less desirable flight levels, because of the six minute additional spacing required if following a Mach 0.82 aircraft.

An exception to the above separation standards is the composite track system where separation on adjacent but staggered tracks is 60 nm laterally and 1,000 ft in altitude (Figure 2). A typical four-track system has a theoretical capacity of 64 aircraft per hour (4 tracks × 4 aircraft/hour × 4 flight levels = 64); the composite track system effectively doubles the system capacity by doubling the number of tracks

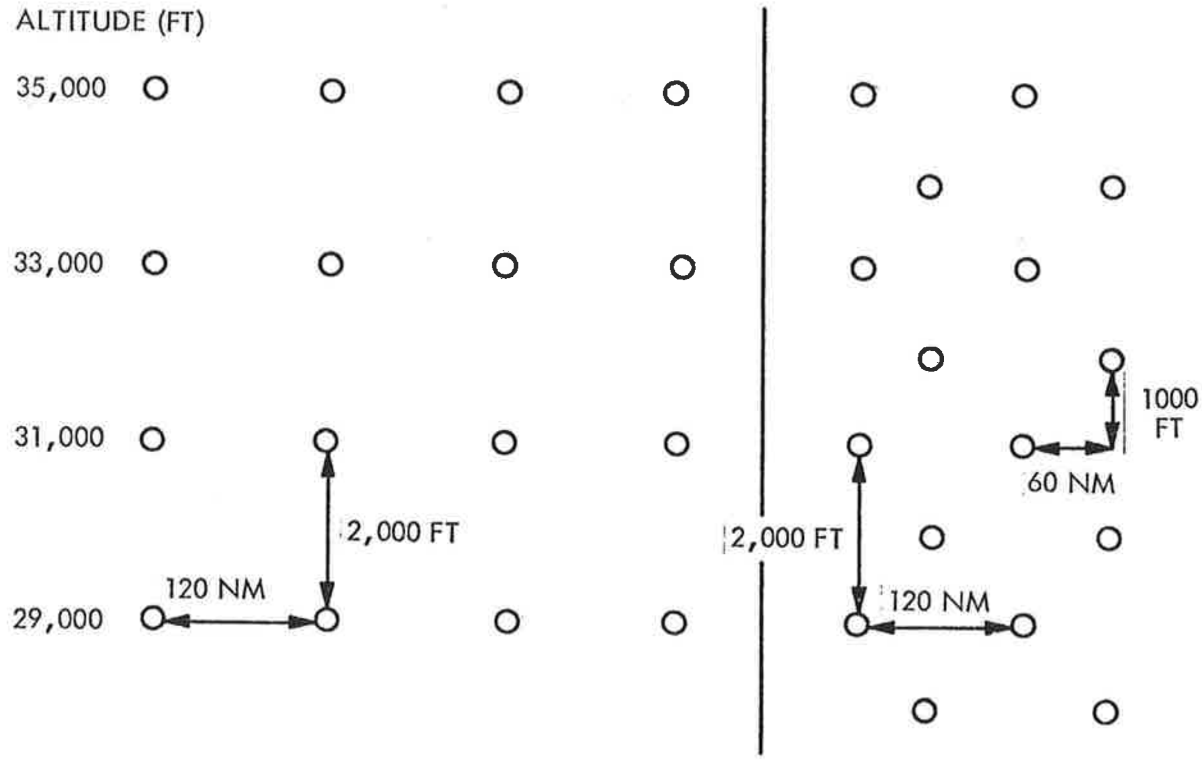

Figure 2. Conventional and Composite Track Systems for North Atlantic Operations.

that can be accommodated in approximately the same airspace. Thus, the capacity of the eight track system is 128 aircraft per hour. Due to the random arrival of aircraft over the entry points into the system, the actual realized capacity is about half the theoretical capacity so the composite track system will be able to handle approximately 64 aircraft per hour with the same ATC imposed penalties as today's system.

2.2 TRACK PLANNING

The responsibility of track planning for the busiest NAT route (Route 2 in Figure 1) is shared by the Gander and Prestwick oceanic control centers. Gander has the prime responsibility for the heavy eastbound flow of traffic, from 2300 Z to 0800 Z, and Prestwick has the prime responsibility for the heavy westbound flow, from 1000 Z to 2100 Z. The track planner determines the minimum time track from several trial tracks based on the New York to London great circle route and his knowledge of the weather and traffic flow characteristics. The track structure is based not only on the weather data but also on users' desires, as indicated by proposed routes submitted by the airlines based on their flight planning rationale. The track planner plots these routes and defines the track structure so as to harmonize the minimum time track with users' desires. This structure consists of from three to five parallel tracks spaced 2° (120 nm) apart with defined flight levels from 29,000 to 37,000 (in 2,000 ft increments) for each track. The Gander and Prestwick planners then negotiate a few flight levels on the fixed tracks for opposite flow traffic depending on the winds and the filed flight plans. The westbound route structure for a typical summer day is shown in Figure 3. Note that no eastbound flights exist on Tracks A, D and E.

2.3 AIR TRAFFIC CONTROL

Air traffic control of flights over the North Atlantic is exercised by oceanic control centers located at Gander, Newfoundland; Prestwick, Scotland; New York City; Lisbon, Portugal; Miami, Florida; and San Juan, Puerto Rico (Ref. 2). The areas of responsibility for each center are shown in Figure 4. These centers provide essentially strategic control of traffic by assigning conflict-free tracks to aircraft while still within radar and VHF radio range. Limited tactical control is exercised by these centers based on voice position reports received via HF (high frequency) radio.

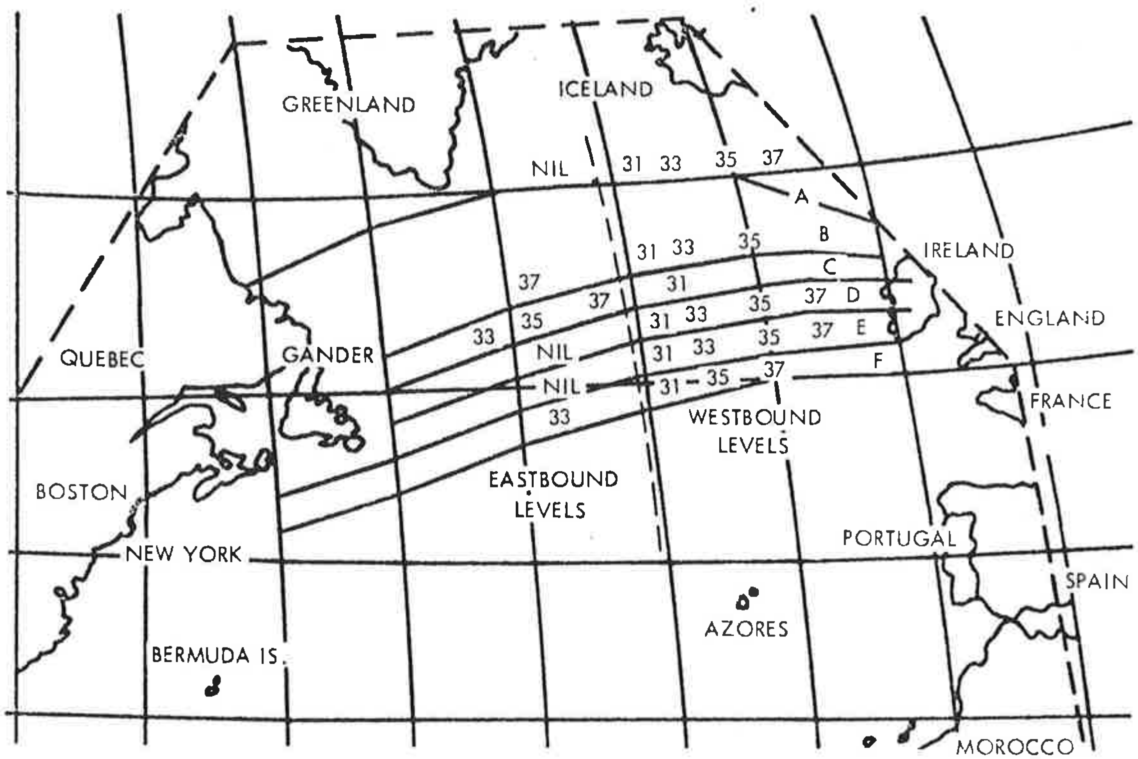

Figure 3. Westbound Route Structure for a Typical Summer Day.

The traffic control procedure begins when a pilot files a flight plan stating the desired route, speed and altitude for his flight. Upon notification of flight departure, the center estimates the time at which the flight will pass over the last domestic fix as well as the first oceanic fix. This estimate is based on the aircraft's departure time, airspeed and wind forecasts. The oceanic controller examines the proposed route,

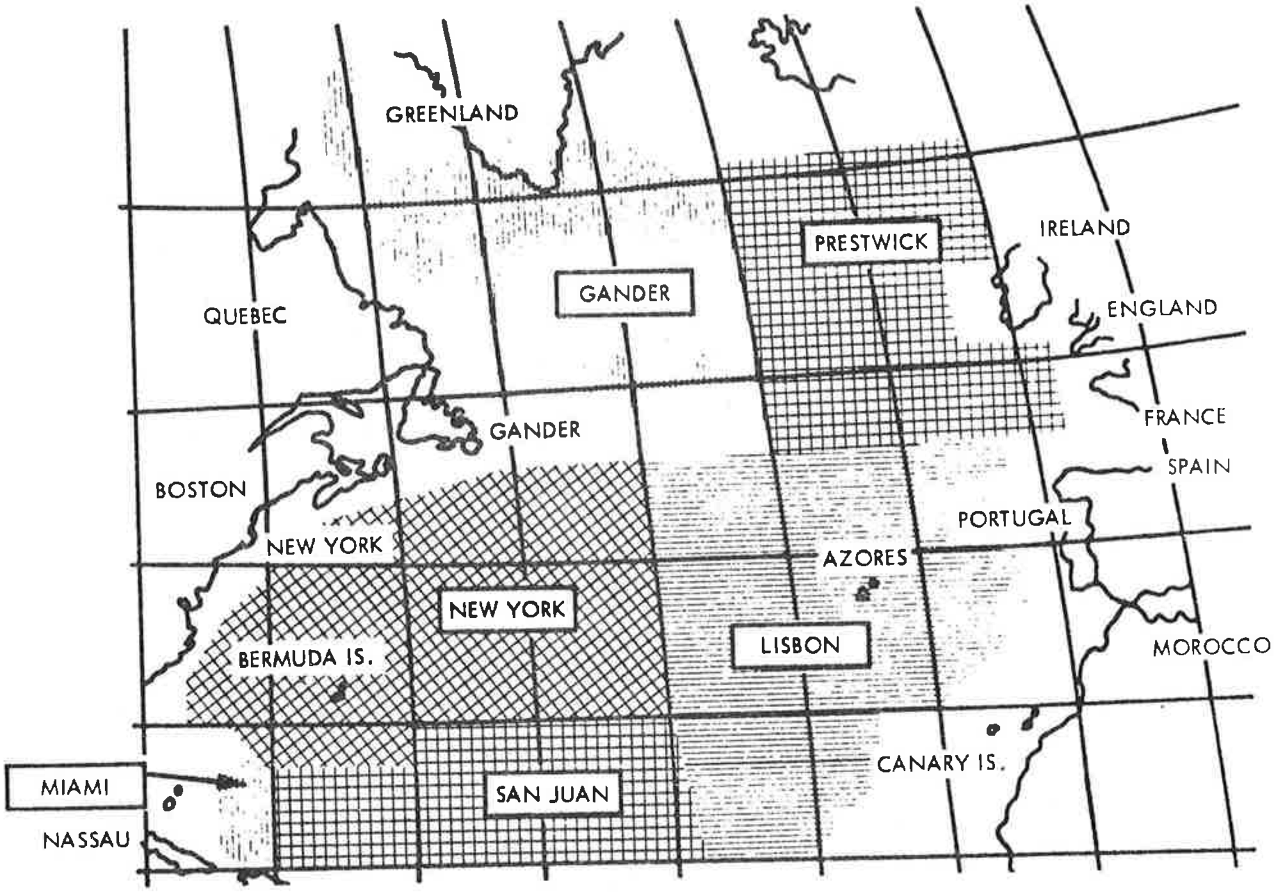

Figure 4. Control Areas for North Atlantic Oceanic Control Centers.

altitude and fix times to tentatively determine if the flight will conflict with other flights. As the flight approaches the boundary between the domestic and oceanic control areas, updated fix estimates are forwarded to the oceanic controller so that he may actively plan the aircraft's oceanic route in conjunction with other active flights.

2.5 AIR TRAFFIC CONTROL SYSTEM MODEL

A general model for analyzing air traffic control systems was developed by ASI in Reference 12. A block diagram of that general model applied to the oceanic ATC system is shown in Figure 5. The oceanic controller issues a flight

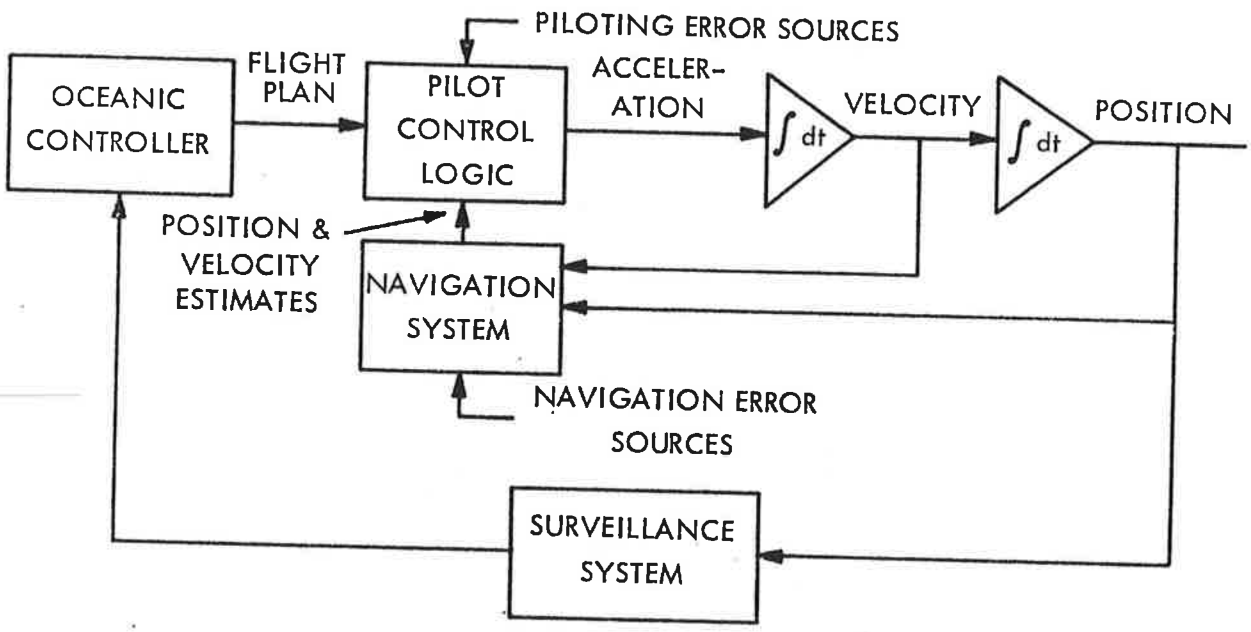

Figure 5. Oceanic Air Traffic Control System.

plan to the pilot who regulates the forces acting on the aircraft through the engine and aerodynamic surface controls. These forces produce aircraft accelerations which are integrated into velocity and position. The pilot uses the navigation system to close the loop on the commands provided in the flight plan. The oceanic controller observes the aircraft by means of a surveillance system (which includes radio position reporting) and issues flight plan corrections to maintain safe separations. A linear model is obtained by assuming that the flight plan determines a nominal trajectory for the aircraft, and departures from the nominal are described by linear equations. The resulting linearized model is shown in Figure 6.

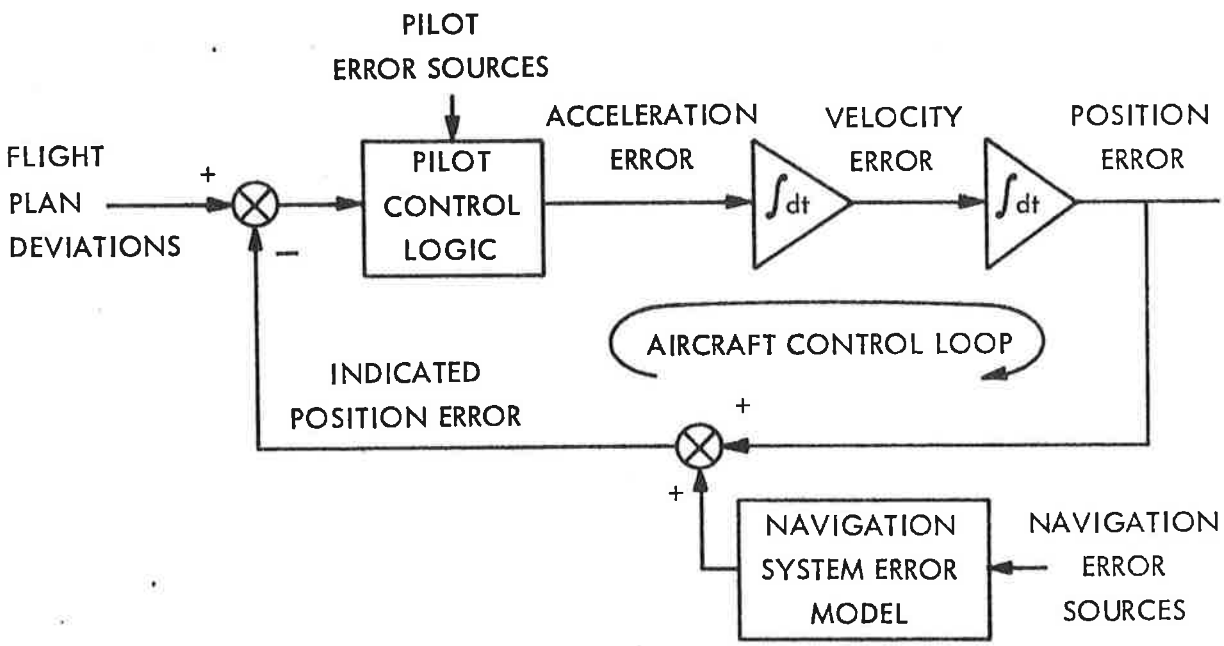

Figure 6. Linear Model of Aircraft Position Errors.

Since the model is linear, the position error due to each source may be treated separately and summed to determine the total position error due to all sources. The position error due to pilot error sources is termed "flight technical error". The aircraft control loop can be approximated as a second order system with near critical damping and characteristic response times of about 60 seconds or less. The navigation system error models have typical characteristic response times of the order of the Schuler period (84 minutes). Furthermore, the closed-loop gain from the navigation error input to the position error output is unity. Consequently, the aircraft dynamics can be ignored in the model for position error as a function of the navigation error sources. (The nominal trajectory of the aircraft strongly influences the navigation error model, but not the small piloting corrections.) The position error caused by the pilot error sources (flight technical error) is influenced by the navigation system error model since that is external to the aircraft control loop. Consequently, navigation errors and flight technical errors can be considered independently to determine their effect on the total position error. This is a significant advantage which results from the development of a linear error model.

SECTION 3

HYBRID NAVIGATION SYSTEMS

Presently, most commercial aircraft navigate the NAT with self-contained dead-reckoning devices such as Doppler and inertial systems, which are subject to long-term drift. The future use of position fixes from satellite or Omega signals is a promising means for bounding either human or equipment errors associated with the present systems. When two, or more, sources of navigational information are available, an optimum combination of the information is possible such that the resultant estimates of position and velocity are more accurate than those available from either source alone. The resultant hybrid navigator is more reliable because the loss of either source of information still permits navigation with the remaining source.

The present study is concerned with hybrid navigators which combine inertial information with the following four navigational aids:

- Doppler radar
- Air data
- Omega
- Satellite ranging

Figure 7 illustrates the data flow for the "aided-inertial" hybrid configuration. The data processing box in Figure 7 is not necessarily an optimal scheme, since it is not clear at the present that optimal data processing techniques will necessarily be used. Indeed, excessive computer requirements may well dictate that suboptimal schemes be used, although the future availability of low-cost, large-scale integrated circuits will probably alter this situation.

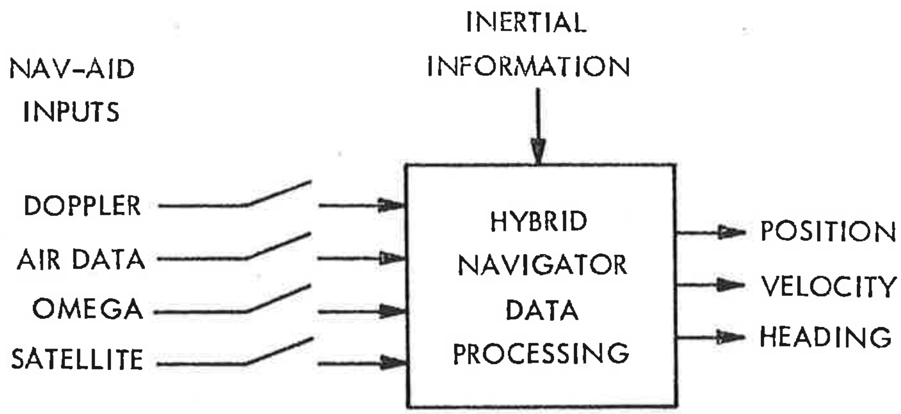

Figure 7. Hybrid Navigator Data Flow.

3.1 KALMAN FILTERS FOR HYBRID NAVIGATION

The study of hybrid navigators has been accelerated in recent years by the advent of powerful navigation computers which have the capability of processing the statistical filtering equations. The idea of combining Doppler and inertial systems to damp the Schuler oscillation (Ref. 13) preceded the introduction of modern estimation theory by Kalman and Bucy (Refs. 14 and 15) around 1960. Since that time most investigators have used Kalman filtering as the basis for the statistical estimation. Interest in applying Kalman's technique to terrestrial navigation systems surfaced from the applications developed for the Apollo guidance system at MIT (Ref. 16) around the mid 1960's.

Figure 8 is presented to describe the application of Kalman filtering for an example hybrid system. The INS is considered to be the primary source of required navigation information (i.e., aircraft position, velocity and heading). For illustration, Doppler radar and Omega are shown as auxiliary systems supplying independent velocity and position information. The indicated INS position information is comprised of true aircraft position plus an error, δP. The external Omega position fix provides

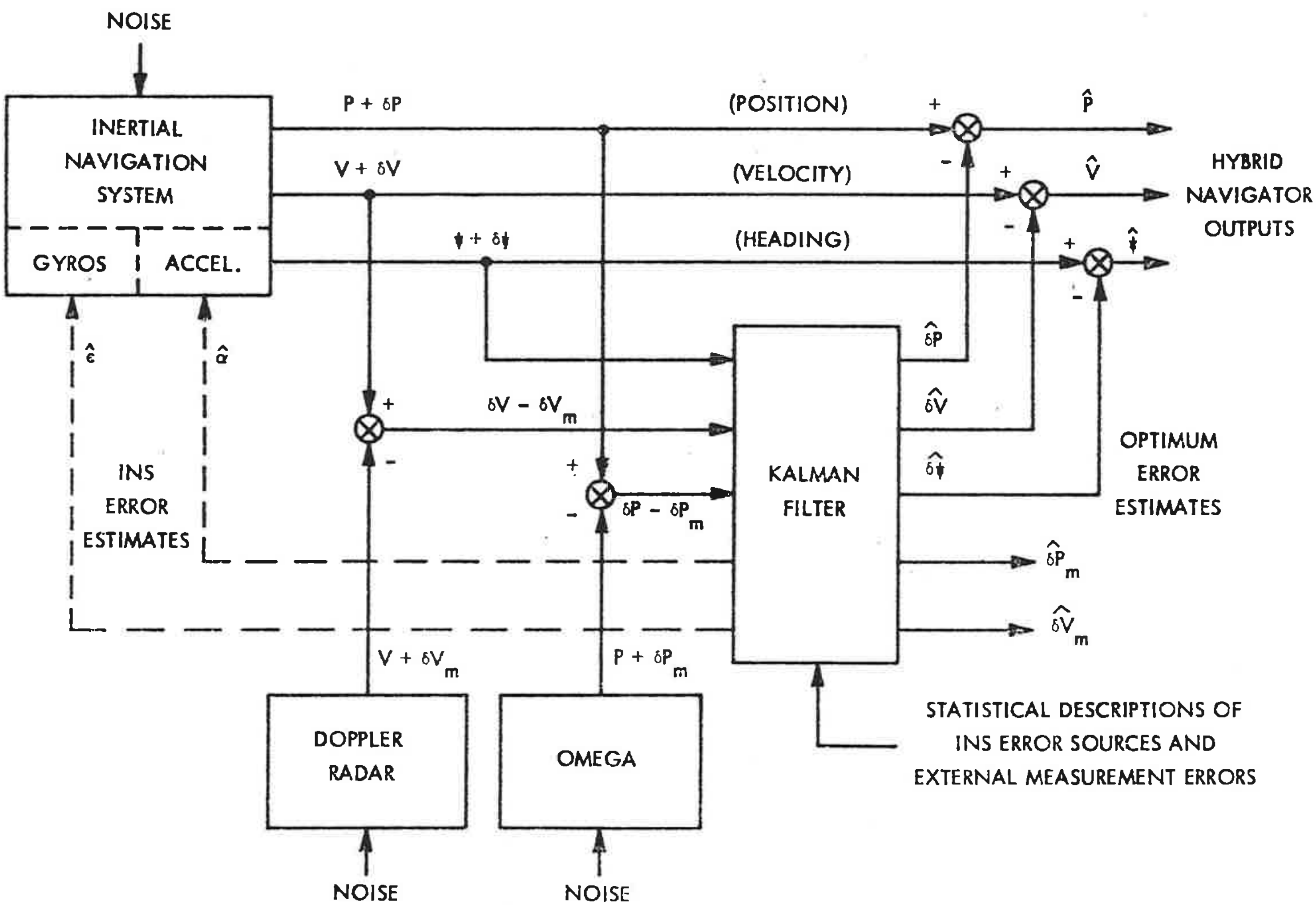

Figure 8. Block Diagram of Kalman Filter for Hybrid Navigation System.

an independent indication of the aircraft's true position subject to a measurement error, δP_m. Subtracting the reference position information from the INS-indicated position results in the error difference $\delta P - \delta P_m$ which is an input to the Kalman filter. In a similar manner $\delta V - \delta V_m$ is also an input to the Kalman filter from the Doppler radar measurement.

The position and velocity fixes can be thought of as measurements of the present errors in the INS. Viewed in this manner, the error difference information constitutes the "measurement" with δP and δV being the quantities to be estimated, and with δP_m and δV_m being the noises in the measurements. Therefore, the Kalman filter being considered here is modeled not on total quantities (P, V) but on error quantities (δP, δV). In order for the Kalman filter to be effective, knowledge of the statistical properties of each error source is required, and is generally obtained from system and component testing and from theoretical considerations.

Processing of the measurement information by the Kalman filter results in optimum estimates (in the sense of satisfying a minimum variance criterion) of the error states, which are denoted in Figure 8 by the "caret" quantities ($\delta\hat{P}$, $\delta\hat{V}$, etc.). As mentioned earlier, instrument and equipment errors can be estimated as well as subsystem output errors. The filter outputs $\hat{\varepsilon}$ and $\hat{\alpha}$ denote estimates of the INS instrument errors, while $\delta\hat{P}_m$ and $\delta\hat{V}_m$ indicate estimates of measurement errors in the Doppler and Omega reference information source.

The final step of the process is to perform the update; i.e., to correct for errors in the subsystem outputs and component errors. This can be done in a closed-loop manner by a mechanical or electrical reset of the equipment, as shown in Figure 8. An alternate approach is an open-loop reset, in which the individual subsystems and components are not physically corrected but rather externally compensated in the computer. In either case, the result is an optimum hybrid system using inputs from all available navigation subsystems and equipments and providing a continuous display of the best possible navigation information.

3.2 ADVANTAGES/DISADVANTAGES OF KALMAN FILTERS

Several advantages of the Kalman filtering approach to hybrid navigation systems were implied in the previous discussion. Some specific benefits are summarized below (ref. 17):

- Optimum integration of subsystems provides more accurate navigation information than is available from any individual subsystem.
- The Kalman filter technique provides the most efficient use of all available navigation information, since a statistical description of each subsystem is modeled in the filter.
- Optimum filtering does not depend on the availability of any one source of navigation information, since the measurement time for any source is independent of all others.
- An optimally integrated navigation system can provide calibration of the subsystems and their components. This was clearly illustrated in Figure 8 where it was shown how the gyros and accelerometers of INS were corrected for internal errors. Similarly, a bias error in the Doppler radar, for example, could be estimated. The real advantage of this is in the event of a subsystem failure, or the unavailability of reference information, the remaining subsystems can continue to function with greater accuracy than they originally were capable of providing.
- A fully computerized hybrid navigation system can relieve the pilot of certain decisions. Since statistical descriptions of the navigation subsystem error models are required, the hybrid system can provide a means of subsystem checkout and failure detection by placing confidence limits on the accuracy of the navigation information indicated by the various subsystems. Further, if the expected limits are far exceeded, it may be indicative of a subsystem failure.

The use of Kalman filtering for hybrid navigation has a great many theoretical advantages; however, the practical implementation of such a system does have limitations. Sensitivity to inaccurate error models and statistics, and the inherent computational burden are among the most important of these. Discussed below are certain aspects of the limitations (Ref. 18).

Implementation of the Kalman filter equations presumes exact knowledge of the linear state dynamics of the navigation system and measurement errors, and the statistics of the random processes involved. Because exact a priori information is impossible, a sensitivity analysis is necessary to ensure adequate performance. Furthermore, most practical systems involve nonlinear dynamics or measurements, and cannot be directly treated by the Kalman filter. Techniques which have been used to overcome this difficulty include linearization about a nominal trajectory, inclusion of the nonlinear behavior in the filter implementation but basing the error covariance calculations on linear approximations, and iterative procedures which attempt to reduce the effect of the nonlinearity. In each case the validity of the resulting error calculations, and the accuracy and stability of the resulting filter must be established by exhaustive simulation techniques.

Since the filter equations must be solved in real time on a computer of finite capability, it is nearly always necessary to approximate the system or its statistics or to otherwise simplify the filter implementation. The largest computer burden of the Kalman filter is imposed by the calculation of the error covariance matrix as a prelude to determining the filter gains. This problem is often circumvented by determining filter gains in an approximate or altogether different manner. For example, typical gain histories are observed during the design of the filter and may be approximated in the actual system by simple functions of time — constants, staircases, exponentials, etc. Again, it is necessary to verify that the modified estimator will not experience a significant loss of accuracy.

The implementation of a hybrid inertial navigator employing a Kalman filter must also consider the finite word length and speed of the navigation computer. In many applications the use of fixed-point arithmetic compounds the accuracy problem. Errors are also introduced by numerical algorithms used to approximate mathematical operations such as trigonometric functions.

In many practical uses of the Kalman filter in aided-inertial systems the filter gains decrease as the number of independent measurements grows. Consequently, the filter tends to reject or discount the most recent measurements in favor of those obtained early in the estimation procedure. Since the error covariance and filter gain calculations do not normally take into account estimation errors introduced by computer roundoff and numerical algorithms, these effects often cause the estimator accuracy to deteriorate.

Another difficulty is sometimes encountered when the external measurements are very accurate, whereas initial estimates of the state contain large errors. In this situation the estimation error covariance decreases very rapidly as the first few measurements are incorporated. The finite accuracy of the computer may permit the calculated error covariance matrix to lose its positive definite characteristic, thereby introducing the possibility of divergent estimation errors.

Measurements are sometimes available more frequently than the computer is capable of processing them. For example, Doppler radar indications of velocity can be obtained several times per second. Rather than reject many of the measurements, the information may be processed by a separate algorithm which is capable of very rapid operation and then passed on to the Kalman filter in a modified form. Here the effects of distortion of information in the measurement due to averaging must also be evaluated.

3.3 A PROBABLE HYBRID SYSTEM CONFIGURATION

A probable aided-INS configuration for near future NAT operations is expected to be the INS-Omega system. The best hybrid combination is a dead-reckoning device plus a position fixing device. Inertial systems have proven to be the best dead-reckoning devices, and are presently the most advanced method of navigation on the North Atlantic. The future promises inertial systems of higher accuracy, higher reliability and lower cost, so there is little motivation to using Doppler radar as the dead-reckoning system.

Omega holds the most promise as the favored position fixing device primarily because of its low cost and world-wide coverage. Furthermore, it is rapidly becoming operational. Although satellites offer potentially better accuracy, they do so at greater costs, and the coverage cannot be made world-wide without a number of satellites. At the present time there is not even international agreement on a frequency band for satellite navigation systems, and the operational implementation of any new navigational system is usually a ten-year evolution. The Department of Defense will probably be the first to test such a system, and their current plan is for a secure, limited-access system. In contrast, there is no constraint on the use of Omega. It also appears more probable that satellites will ultimately be used in the oceanic areas for surveillance as opposed to navigation, since in the interests of safety and reliability, it is better to have the navigation system and surveillance system independent.

The computer program NATNAV developed under this study is capable of simulating an INS or air data, dead-reckoning system alone or with updates provided by Doppler, Omega and/or satellite-ranging measurements. This program provides a tool for evaluating the performance of those navigators which might be used over the NAT in the next few years. A comparison of several such systems is presented in Section 7 of this report.

SECTION 4

ERROR ANALYSIS

Two basic approaches are available for analyzing the errors of hybrid navigation systems: covariance matrix ensemble error analysis and Monte Carlo simulation. For the type of analysis anticipated with this program, the covariance matrix approach is the only feasible method. Monte Carlo simulation allows nonlinear systems to be treated directly, and can also be used to investigate performance for a specific set of deterministic errors (e.g., worst case situations). Monte Carlo simulations can also provide more details of the error distribution (such as 3rd and higher order statistics) and are not restricted to normal Gaussian error distributions. However, one ensemble simulation can provide the equivalent of a large number of Monte Carlo simulations which are both time consuming and costly. The number of runs required to obtain meaningful statistics by Monte Carlo for a spectrum of operating conditions is prohibitive.

4.1 THE COVARIANCE METHOD

The covariance error analysis approach (Ref. 19) was selected for the NATNAV simulation program over a Monte Carlo simulation for economy of computer time. The method requires that all the navigation system errors be described by a set of linear differential equations, with the first and second order statistics of the forcing functions specified a priori. The error equations are linearized about an assumed flight path, and the system errors are then mathematically described by a covariance matrix. The purpose of the simulation is to determine how the covariance matrix changes with time while the maneuvering aircraft takes fixes with its several sensors. The required output of the navigation system model is a time history of the distribution of position errors caused by the navigation system.

In order to apply the covariance technique, the error equations for the hybrid navigation system are written in the first-order linear form:

$$\dot{\underline{x}} = F\underline{x} + G\underline{w} \qquad (1)$$

where

$\underline{x}$ = augmented state vector of navigation system errors

$\underline{w}$ = vector of white noise forcing functions

F = augmented system dynamics matrix

G = white noise forcing matrix

The matrices F and G are time-varying quantities which depend upon the characteristics of the INS being modeled and the aiding systems being used, and the nominal flight path of the aircraft. These must all be specified by the simulation user. As indicated by the above equation, the requirement is imposed that the system be driven by white (uncorrelated) noise. Because the system errors are not necessarily modeled as white noise, a "shaping filter" is introduced which converts white noise inputs into appropriately shaped "colored" noise which describes the correlated statistical behavior of the error sources (Ref. 19). Thus Equation (1) represents the hybrid navigator state augmented by the shaping filter state.

The position and velocity errors will be determined by propagating an error covariance matrix along the flight plan route. The error covariance matrix is defined by

$$P = \langle \underline{x}\,\underline{x}^T \rangle = \text{error covariance matrix} \qquad (2)$$

where < > indicates the expected value. The error state vector $\underline{x}$ contains the basic INS errors, plus additional elements for each contributing error source in the complete system. A maximum dimension of 34 was selected to accommodate the situation of a space-stabilized INS augmented by Doppler, Satellite and Omega measurements. The error models will be described in the next section. The possible elements of the state vector are as follows:

9 INS errors	3 platform misalignment angle errors 3 inertial position errors 3 inertial velocity errors
13 INS component error sources	3 gyro drifts — scale factor 3 gyro drifts — colored noise 3 accelerometer errors — colored noise 3 geodetic uncertainties — colored noise 1 altimeter error — scale factor
12 position and velocity measurement errors	2 Doppler velocity errors — scale factor 2 Doppler velocity errors — colored noise 2 hyperbolic position fix errors — bias 2 hyperbolic position fix errors — colored noise 2 range measurement errors — bias 2 range measurement errors — colored noise

All colored noise sources can be varied from white noise ($\tau \rightarrow 0$) to random walk ($\tau \rightarrow \infty$) by choice of the correlation time τ. Selected INS error sources can be neglected by making the strength of the noise small, and failures can be simulated by making the INS noise sources very strong.

The analysis is based on the minimum variance estimator as derived by Kalman for the discrete measurement case (Refs. 14, 15). The discrete filter is chosen for this application to deal with the questions raised by non-periodic and incomplete measurements. If desired, a simulation of the continuous filter can be obtained in the limit as the sampling time becomes small compared with the Schuler period.

a suboptimal system will result. Useful comparisons can be drawn as a function of filter implementation. The performance of a proposed suboptimum filtering technique can be evaluated by comparing the navigation error magnitudes with those obtained with $\underline{K}_{opt}$. When a suboptimal gain is used, the updated covariance matrix is given by Equation 9:

$$P^{+} = (I - \underline{K}\,\underline{h}^{T})P - [P\underline{h} - \alpha\underline{K}]\underline{K}^{T}$$

$$= P - \alpha[\underline{K}\,\underline{K}_{opt}^{T} + (\underline{K}_{opt} - \underline{K})\underline{K}^{T}] \qquad (14)$$

The simulation program is capable of accepting suboptimum gain histories, $\underline{K}(t)$, and updating the covariance matrix as shown above. The suboptimum gain is obtained by linear interpolation from an input table of $\underline{K}(t_i)$.

4.3 MALFUNCTIONS AND BLUNDERS

Malfunctions and blunders are essentially the same type of phenomenon; one is an equipment failure while the other is a human failure. Both types of failure will be treated similarly in the simulation. The suboptimum filtering option will be used to account for the fact that the statistics of the actual error sources encountered in a blunder or malfunction situation are different from the statistics of the error sources assumed in processing the measurements. Suboptimum filters are characterized by the fact that the model of the system used to determine the filter gains is different from the actual model which best represents the system. Both cases are treated together here.

The normal mode of operating the simulation is to assume that the system is properly modeled and the specified error sources are the actual error sources encountered. In this mode, the program starts with the initial uncertainties in all the estimated quantities and propagates them in time by means of the covariance matrix and its associated differential equation as described above. When a measurement is taken, the appropriate optimum filter gain is calculated and used to update the covariance matrix. Thus the simulation generates time histories of the covariance matrix P_n and the corresponding optimal filter gain K_n based on the assumed nominal error models.

The evaluation of malfunctions/blunders involves a second pass through the simulation. In this pass, the initial uncertainties and error models for the actual malfunction/blunder situation are input to the program. However, during this run the covariance matrix P_a based on the actual error models is updated by means of the filter gains K_n calculated previously for the nominal error models. In other words, the optimum gains for the nominal situation are used as suboptimum gains in the malfunction/blunder situation. The process is shown functionally in Figure 9. To summarize:

- For the normal mode; P_n gives the uncertainty in the error estimates assuming optimum filtering.
- For the suboptimum mode; P_n gives the uncertainty assumed by the suboptimum filter and allows determination of the suboptimum filter gain.
- For the suboptimum mode; P_a gives the actual uncertainty in each estimated variable.

Most blunders or equipment failures are treated by increasing the corresponding elements of P_a and Q_a at the time of the failure without changing P_n and Q_n. For example, to simulate a skipped Omega lane count, the strength of the Omega error source would be increased in Q_a and the uncertainty in the estimate of the Omega error would be increased in P_a. A difference in the spectral content

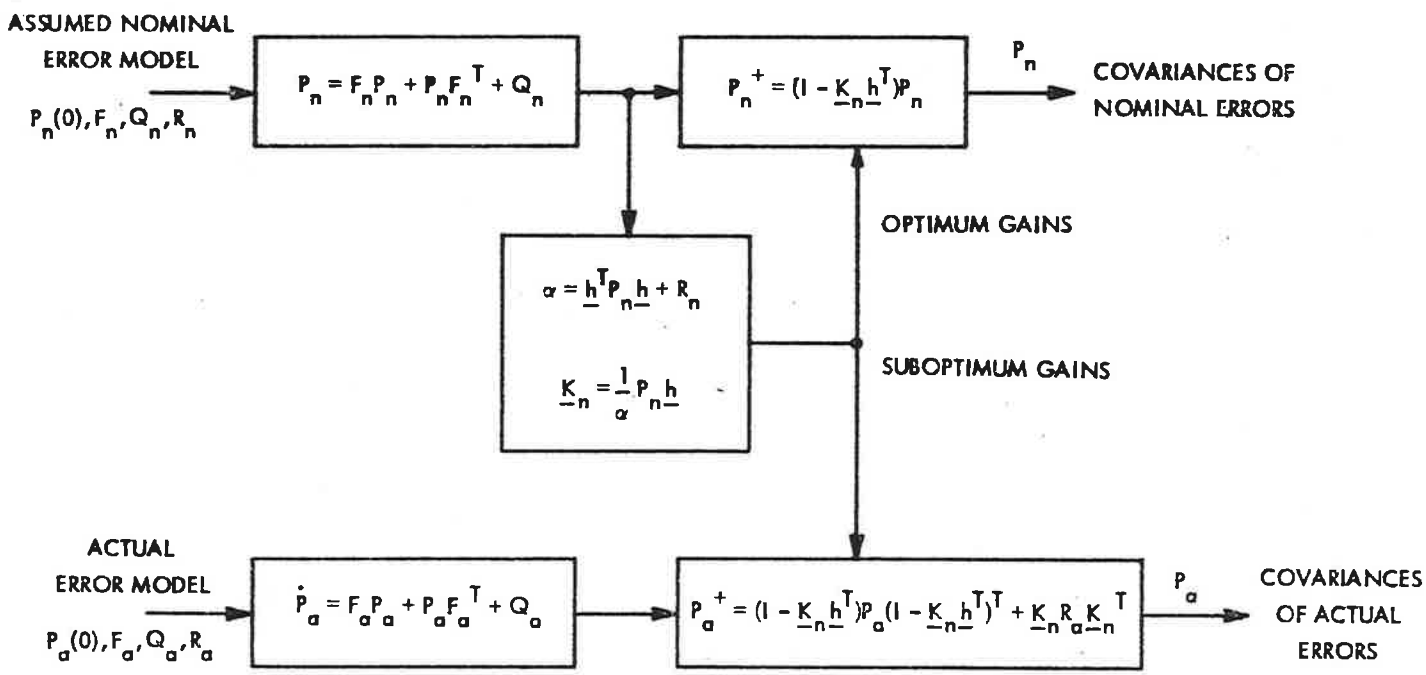

Figure 9. Functional Diagram for Blunder/Malfunction Evaluation.

of the assumed measurement errors and the actual measurement errors would be reflected by a difference between F_n and F_a.

Although most blunders would be treated as described, some would be handled specially. A waypoint input incorrectly, for example, would take the aircraft to the wrong waypoint with the distribution as predicted by the program. A fast alignment would be handled automatically, since the alignment time is a program input. Input of the wrong initial position would be simulated by increasing the initial position uncertainty in $P_a(0)$. Alignment while the vehicle was moving would be simulated by making a velocity measurement that had the assumed velocity error uncertainty zero in P_n while the actual velocity uncertainty was finite in P_a.

SECTION 5

ERROR MODELS

5.1 INERTIAL NAVIGATION SYSTEM

The INS is becoming the principal navigation device for transoceanic aviation since it provides an accurate means of completely self-contained navigation. Once the initial position is known by the navigation computer, accelerometers mounted on an inertial platform determine the movement of the aircraft from this initial position. The inertial platform is partially isolated from aircraft motions by being suspended in a set of supporting gimbals. The gimbals may be changed to compensate for the rotational movement of the aircraft over the surface of the rotating earth. Gyroscopes detect any angular motions of the platform and generate signals to a servo system which provides torque to keep the platform stabilized with respect to the reference coordinate frame. For strapdown systems the inertial instruments are fixed to the aircraft, and the effective isolation is provided computationally.

When the inertial system is turned on, it must be aligned so that the computer knows the initial position and groundspeed of the aircraft, and so that the stable platform has the correct initial orientation relative to the earth. The platform is typically aligned in such a way that its accelerometer input axes are horizontal, often with one of them pointed north. As the aircraft accelerates, maneuvers, and cruises, the accelerometers measure changes in velocity, and the computer faithfully records the motion. The navigation errors which result from using inertial systems are due to the following primary sources:

- Initial misalignment of the inertial platform.
- Initial position error of the aircraft.

- Gyro torquer motor scale factor.
- Gyro drift.
- Accelerometer bias and scale factor error.
- Gyro and accelerometer misalignment on the platform.
- Velocity quantizer error.
- Random noise.

Three inertial navigation systems currently in use in commercial aircraft are the Litton LTN-51 (Ref. 21), the Delco Electronics Carousel IV (Ref. 22), and the Collins INS-61B (Ref. 23). Overall system accuracies without updates are on the order of one nautical mile per hour. In the LTN-51 system, the platform is aligned with the initial heading of the aircraft, and the local vertical component of the platform angular rate with respect to an earth-fixed reference frame is constrained to be zero. In this system, the input axes of the horizontal gyros move about the local vertical axis of the platform (due to motion of the aircraft over the earth's surface) and are not constrained with respect to local north and east. The horizontal gyros are torqued to keep the platform locally level. The Carousel IV system is similar except that the horizontal instruments are rotated about the local vertical axis at a rate of one rpm. This rotation provides modulation of some of the unknown navigation errors related to the sensitive axes of the horizontal instruments which minimizes their effect on system performance. The INS-61B is a more recent system and is standard equipment on the DC-10. In this system, the azimuth axis is torqued with the longitude rate, thus keeping the horizontal axis aligned with the north and east directions. The INS-61B also has a vertical accelerometer to provide instantaneous vertical speed indications and to smooth the barometric altitude indication.

5.1.1 BASIC INS ERROR MODEL

A general error analysis theory applicable to a very broad class of aided-inertial navigation systems has been used in developing the simulation program. This theory is described in detail in Reference 24 and is summarized in Reference 25.

Most of the inertial navigation systems in operation today are local-level (two-dimensional) and thus require only a seventh-order model to adequately describe their performance. However, a three-dimensional (ninth-order) INS has been modeled in the simulation to provide the capability for evaluating these classes of systems in the future.

The general model of inertial navigation systems is given by the following matrix equation (Refs. 24, 25):

$$\Lambda \underline{y} = \underline{q} \tag{15}$$

where

$\underline{y} = [\epsilon_N, \epsilon_D, \epsilon_E, \delta L, \delta \ell, \delta h]^T$

= error state vector of attitude and position errors

Λ = system characteristic matrix, identical for all INS configurations

$\underline{q} = [q_1, q_2, q_3, q_4, q_5, q_6]^T$ = forcing vector of inertial system errors

It is important to emphasize that a computer simulation program developed in accordance with Equation (15) is valid for all possible INS configurations; local level, wander-azimuth, space-stabilized, strapdown, etc. Both the coordinate frame mechanized by the inertial instruments and the computation frame are completely arbitrary. It is only the forcing function, $\underline{q}$, which depends on the system configuration through the angular velocity and orientation of the inertial instruments.

In order to rewrite this equation as a first order vector-differential equation, we define the error state of the INS to be (Ref. 26)

$$\epsilon^T(t) = [\epsilon_N, \epsilon_E, \epsilon_D, \delta L, \delta \ell, \delta \dot{L}, \delta \dot{\ell}, \delta h, \delta \dot{h}] \tag{16}$$

where the nine basic INS errors are:

$\epsilon_N, \epsilon_E, \epsilon_D$ — north, east and down platform tilt errors

$\delta L, \delta \ell, \delta h$ — latitude, longitude and altitude position errors

$\delta \dot{L}, \delta \dot{\ell}, \delta \dot{h}$ — latitude, longitude and altitude rate errors

This allows Equation (15) to be written as

$$\dot{\epsilon} = F_\epsilon \underline{\epsilon} + G_\epsilon \underline{q} \tag{17}$$

where

$$F_\epsilon = \begin{bmatrix} 0 & f_{12} & f_{13} & f_{14} & 0 & 0 & f_{17} & 0 & 0 \\ f_{21} & 0 & f_{23} & 0 & 0 & -1 & 0 & 0 & 0 \\ f_{31} & f_{32} & 0 & f_{34} & 0 & 0 & f_{37} & 0 & 0 \\ 0 & 0 & 0 & 0 & 0 & 0 & 0 & 0 & 0 \\ 0 & 0 & 0 & 0 & 0 & 0 & 1 & 0 & 0 \\ 0 & f_{62} & f_{63} & f_{64} & 0 & f_{66} & f_{67} & f_{68} & f_{69} \\ f_{71} & 0 & f_{73} & f_{74} & 0 & f_{76} & f_{77} & f_{78} & f_{79} \\ 0 & 0 & 0 & 0 & 0 & 0 & 0 & 0 & 0 \\ f_{91} & f_{92} & 0 & f_{94} & 0 & f_{96} & f_{97} & f_{98} & 0 \end{bmatrix} \tag{18}$$

$$
G_\varepsilon = \begin{bmatrix}
1 & 0 & 0 & 0 & 0 & 0 \\
0 & 1 & 0 & 0 & 0 & 0 \\
0 & 0 & 1 & 0 & 0 & 0 \\
0 & 0 & 0 & 0 & 0 & 0 \\
0 & 0 & 0 & 0 & 0 & 0 \\
0 & 0 & 0 & 1/r & 0 & 0 \\
0 & 0 & 0 & 0 & 1/r \cos L & 0 \\
0 & 0 & 0 & 0 & 0 & 0 \\
0 & 0 & 0 & 0 & 0 & -1
\end{bmatrix} \tag{19}
$$

and the non-zero elements F_{ij} will be defined in Section 5.6.

Neglecting both gyro and accelerometer non-orthogonality errors, the forcing functions are comprised of 13 INS component errors:

$$
\begin{bmatrix} q_1 \\ q_2 \\ q_3 \end{bmatrix} = C_p^{\ n} \begin{bmatrix} (u)\omega_x \\ (u)\omega_y \\ (u)\omega_z \end{bmatrix} + C_p^{\ n} \begin{bmatrix} \tau_x & 0 & 0 \\ 0 & \tau_y & 0 \\ 0 & 0 & \tau_z \end{bmatrix} \underline{\omega}_{ip}^{p}
$$

$$
\begin{bmatrix} q_4 \\ q_5 \\ q_6 \end{bmatrix} = C_p^{\ n} \begin{bmatrix} (u)f_x \\ (u)f_y \\ (u)f_z \end{bmatrix} + \begin{bmatrix} -\xi g \\ \eta g \\ -\Delta g \end{bmatrix} + \begin{bmatrix} 0 \\ 0 \\ -\kappa\omega_s^{\ 2} h \tau_h \end{bmatrix} \tag{20}
$$

The component error models are described in the following section. The platform-to-navigation frame transformation matrix, C_p^n, and the platform torquing rate, $\underline{\omega}_{ip}^p$, depend upon the INS configurations discussed in Section 5.1.4.

5.1.2 INS COMPONENT ERROR MODELS

The 13 INS component errors consist of three gyro drift uncertainties, three accelerometer measurement uncertainties, three gyro torquer scale factor errors, three geodetic uncertainties, and an altimeter uncertainty.

- GYRO DRIFT UNCERTAINTIES

The three gyro drift uncertainties, $(u)\omega_i$, are each modeled as an exponentially-correlated (colored) noise plus an additive random (white) noise:

$$(u)\omega_i = \delta_i + w_{g_i} \quad ; \quad i = x,y,z \tag{21}$$

where w_{g_i} is a white noise, of specified strength, and the colored noise is determined by

$$\dot{\delta}_i = -\frac{1}{\tau_{g_i}}\delta_i + v_{g_i} \tag{22}$$

The correlation time of the colored noise is τ_{g_i}, and the strength of the driving white noise v_{g_i} is obtained from Equation (6), using the specified variance of the colored noise $\sigma^2_{\delta_i}$.

- ACCELEROMETER MEASUREMENT UNCERTAINTIES

The accelerometer measurement uncertainties, $(u)f_i$, are also modeled as colored noise plus white noise:

$$(u)f_i = \alpha_i + w_{a_i} \quad ; \quad i = x,y,z \tag{23}$$

where w_{a_i} is the white noise of specified strength, and the colored noise is given by

$$\dot{\alpha}_i = -\frac{1}{\tau_{a_i}} \alpha_i + v_{a_i} \tag{24}$$

with correlation time τ_{a_i}, and covariance $\sigma^2_{a_i}$. Again, the strength of v_{a_i} is calculated from Equation (6).

- GYRO TORQUER SCALE FACTOR ERRORS

The three gyro torquer scale factor errors, τ_i, are modeled as random constants:

$$\dot{\tau}_i = 0 \quad ; \quad i = x,y,z \tag{25}$$

- GEODETIC UNCERTAINTIES

The uncertainties in the three components of the local gravity vector, ΔG_i, are modeled as colored noises:

$$\Delta\dot{G}_i = -\frac{V_g}{\beta_i} \Delta G_i + v_i \quad ; \quad i = x,y,z \tag{26}$$

The gravity vector anomaly is

$$\Delta G^T = [\xi g, \eta g, \Delta g]$$

where ξ, η are deflections of the local vertical and Δg is the gravity disturbance.

Here β_i is the correlation distance and V_g is the nominal aircraft speed; the effective correlation time is β_i/V_g, and the noise strength for v_i is, from Equation (6),

$$Q_{vi} = 2\sigma^2_{G_i} V_g/\beta_i \tag{27}$$

- ALTIMETER SCALE FACTOR ERROR

A combination of inertial and barometric altitude indications is used to estimate the gravity in a three-dimensional INS (Ref. 24). In Equation (20), the altimeter scale factor error, τ_h, produces a vertical acceleration uncertainty, which is proportional to altitude, h, the nonlinear altitude weighting parameter, κ, and the square of the Schuler period, ω_s^2. τ_h is a random constant:

$$\dot{\tau}_h = 0 \tag{28}$$

5.1.3 AUGMENTED INS ERROR MODEL

Each of the component INS errors discussed above requires an additional element in the INS error state vector. By augmenting the basic INS error state vector in Equation (16) with the 13 component errors, we obtain the complete 22-element INS error state vector shown in Equation (29).

$$
\underline{x}_{INS} = \begin{bmatrix} \epsilon_N \\ \epsilon_E \\ \epsilon_D \\ \delta L \\ \delta \ell \\ \delta \dot{L} \\ \delta \dot{\ell} \\ \delta h \\ \delta \dot{h} \\ \hdashline \delta_x \\ \delta_y \\ \delta_z \\ \alpha_x \\ \alpha_y \\ \alpha_z \\ \tau_x \\ \tau_y \\ \tau_z \\ \xi_g \\ \eta_g \\ \Delta g \\ \tau_h \end{bmatrix} \begin{array}{l} \left.\begin{array}{l} \\ \\ \\ \\ \\ \\ \\ \\ \\ \end{array}\right\} \text{Basic INS errors } (= \underline{\varepsilon}) \\ \left.\begin{array}{l} \\ \\ \\ \\ \\ \\ \\ \\ \\ \\ \\ \\ \\ \end{array}\right\} \text{INS component errors} \end{array} \tag{29}
$$

Taking the derivative of Equation (29), and substituting with Equations (16-26, 28), we obtain the following first-order, vector-differential equation describing the augmented INS error model:

$$\dot{\underline{x}}_{INS} = F_{INS}\underline{x}_{INS} + G_{INS}\underline{w}_{INS} \tag{30}$$

where

$$F_{INS} = \left[\begin{array}{c|c} F_\epsilon & G_\epsilon A \\ (9 \times 9) & (9 \times 13) \\ \hline 0 & D \\ (13 \times 9) & (13 \times 13) \end{array}\right] \tag{31}$$

$$G_{INS} = \left[\begin{array}{c|c} G_\epsilon B & 0 \\ (9 \times 6) & (9 \times 9) \\ \hline 0 & E \\ (13 \times 6) & (13 \times 9) \end{array}\right] \tag{32}$$

with the following definitions

$$A \triangleq \left[\begin{array}{c|c|c|ccc|c} C_p^{\,n} & 0 & \omega_x C_{11}, \omega_y C_{12}, \omega_z C_{13} & & 0 & & 0 \\ & & \omega_x C_{21}, \omega_y C_{22}, \omega_z C_{23} & & & & 0 \\ (3 \times 3) & (3 \times 3) & \omega_x C_{31}, \omega_y C_{32}, \omega_z C_{33} & & (3 \times 3) & & 0 \\ \hline 0 & C_p^{\,n} & 0 & -1 & 0 & 0 & 0 \\ & & & 0 & 1 & 0 & 0 \\ (3 \times 3) & (3 \times 3) & (3 \times 3) & 0 & 0 & 1 & -\kappa\omega_s^{\,2}h \end{array}\right]$$

(33)

$$
B \triangleq \left[\begin{array}{c:c}
\begin{matrix} C_p^{\,n} \\ (3 \times 3) \end{matrix} & \begin{matrix} 0 \\ (3 \times 3) \end{matrix} \\
\hdashline
\begin{matrix} 0 \\ (3 \times 3) \end{matrix} & \begin{matrix} C_p^{\,n} \\ (3 \times 3) \end{matrix}
\end{array}\right] \tag{34}
$$

$$
D \triangleq - \begin{bmatrix}
\tau_{g_x}^{-1} & & & & & & & & & & & & \\
& \tau_{g_y}^{-1} & & & & & & & & & & & \\
& & \tau_{g_z}^{-1} & & & & & & & 0 & & & \\
& & & \tau_{a_x}^{-1} & & & & & & & & & \\
& & & & \tau_{a_y}^{-1} & & & & & & & & \\
& & & & & \tau_{a_z}^{-1} & & & & & & & \\
& & & & & & 0 & & & & & & \\
& & & & & & & 0 & & & & & \\
& & & & & & & & 0 & & & & \\
& & & & & & & & & \beta_x^{-1} & & & \\
& & 0 & & & & & & & & \beta_y^{-1} & & \\
& & & & & & & & & & & \beta_z^{-1} & \\
& & & & & & & & & & & & 0
\end{bmatrix} \tag{35}
$$

$$
E \triangleq \begin{bmatrix}
1 & 0 & 0 & \cdots & \cdots & \cdots & \cdots & \cdots & 0 \\
0 & 1 & 0 & & & & & & \vdots \\
0 & 0 & 1 & 0 & & & & 0 & \vdots \\
\vdots & & 0 & 1 & 0 & & & & \vdots \\
\vdots & & & 0 & 1 & 0 & & & \vdots \\
\vdots & & & & 0 & 1 & 0 & & \vdots \\
\vdots & & & & & 0 & 0 & & \vdots \\
\vdots & & & & & 0 & 0 & & \vdots \\
\vdots & & & & & 0 & 0 & & \vdots \\
\vdots & & & & & 0 & 1 & 0 & \vdots \\
\vdots & & 0 & & & & 0 & 1 & 0 \\
\vdots & & & & & & & 0 & 1 \\
0 & \cdots & \cdots & \cdots & \cdots & \cdots & \cdots & \cdots & 0
\end{bmatrix} \tag{36}
$$

where

$$\underline{\omega}_{ip}^{p} = [\omega_x, \omega_y, \omega_z]^T \tag{37}$$

$$C_p{}^n = \begin{bmatrix} C_{11} & C_{12} & C_{13} \\ C_{21} & C_{22} & C_{23} \\ C_{31} & C_{32} & C_{33} \end{bmatrix} \tag{38}$$

The vector $\underline{w}_{INS}$ contains the 15 driving white noises of the INS component errors (see Section 5.1.2):

$$
\underline{w}_{INS} = \begin{bmatrix} w_{g_x} \\ w_{g_y} \\ w_{g_z} \\ w_{a_x} \\ w_{a_y} \\ w_{a_z} \\ v_{g_x} \\ v_{g_y} \\ v_{g_z} \\ v_{a_x} \\ v_{a_y} \\ v_{a_z} \\ v_x \\ v_y \\ v_z \end{bmatrix} \tag{39}
$$

5.1.4 INS CONFIGURATIONS

The INS platform torquing rate $\underline{\omega}_{ip}^{p}$ and the platform-to-navigation transformation matrix $C_p^{\,n}$ depend upon the mechanization of the INS being simulated. Seven different INS configurations have been incorporated into the error analysis program. These are described below.

1. Space Stabilized System (Ref. 24).

By definition, the platform is stabilized with respect to the inertial frame:

$$\underline{\omega}_{ip}^{p} = \underline{0} \tag{40}$$

If it is assumed that the platform frame is nominally aligned with the inertial frame, then:

$$C_p^{\,n} = \begin{bmatrix} -\sin L \cos \lambda & -\sin L \sin \lambda & \cos L \\ -\sin \lambda & \cos \lambda & 0 \\ -\cos L \cos \lambda & -\cos L \sin \lambda & -\sin L \end{bmatrix} \tag{41}$$

where λ is the celestial longitude.

2. Local-Level System (Ref. 24).

It will be assumed that the platform frame is nominally aligned with the navigation frame. Thus

$$C_p^{\,n} = I \tag{42}$$

and

$$\underline{\omega}_{ip}^{p} = \begin{bmatrix} \dot{\lambda} \cos L \\ -\dot{L} \\ -\dot{\lambda} \sin L \end{bmatrix} \tag{43}$$

3. Free Azimuth System.

Free azimuth systems are essentially local-level systems with a space stabilized vertical or azimuth channel; i.e., the platform is commanded to remain in the local horizontal plane but is uncommanded in azimuth. The relationship between the platform coordinate frame and the navigation frame is specified by defining an azimuth rotation angle measured clockwise from indicated north to a fiducial line on the platform. Thus:

$$C_p^{\,n} = \begin{bmatrix} \cos\psi & -\sin\psi & 0 \\ \sin\psi & \cos\psi & 0 \\ 0 & 0 & 1 \end{bmatrix} \tag{44}$$

where $\dot{\psi} = \lambda \sin L$.

The angular velocity of the platform frame with respect to the inertial frame is found by transforming $\underline{\omega}_{ip}^{n}$ given by Equation (43), without the vertical component, into the platform frame using Equation (44); i.e.,

$$\underline{\omega}_{ip}^{p} = C_n^{\,p} \begin{bmatrix} \dot{\lambda}\cos L \\ -L \\ 0 \end{bmatrix} \qquad C_n^{\,p} = (C_p^{\,n})^T \tag{45}$$

Because the platform of the free azimuth system is inertially non-rotating, the system has the obvious advantage of being insensitive to azimuth gyro torquing uncertainty.

4. Strapdown System (Refs. 24, 26).

Strapdown systems are characterized by their lack of gimbal support structure. The system is mechanized by mounting three gyros and three accelerometers directly to the vehicle for which the navigation function is to be provided. An onboard digital computer keeps track of the vehicle's attitude with respect to some reference frame based on information from the gyros. The computer is thus able to provide the coordinate transformation necessary to transform the accelerometer outputs to a computational reference frame.

The specification of $C_p^{\ n}$ and $\underline{\omega}_{ip}^{p}$ cannot be accomplished without a complete time history of the vehicle's attitude for a given flight. By neglecting the pitch and roll attitudes of the aircraft, a quasi-stationary strapdown system can be modeled as a type of local-level system:

$$C_p^{\ n} \approx \begin{bmatrix} \cos\psi & -\sin\psi & 0 \\ \sin\psi & \cos\psi & 0 \\ 0 & 0 & 0 \end{bmatrix} \tag{46}$$

where ψ = aircraft heading, and

$$\underline{\omega}_{ip}^{p} \approx C_n^{\ p} \begin{bmatrix} \dot{\lambda}\cos L \\ -\dot{L} \\ -\dot{\lambda}\sin L \end{bmatrix} \tag{47}$$

5. Rotating Azimuth System (Ref. 25).

The rotating azimuth mechanization (e.g. the AC Carousel INS) is basically a local-level navigator with relatively high speed azimuth rotation. Because the level gyros and accelerometers are rotating relative to the navigation frame, the instrument uncertainties will be frequency modulated at the azimuth rotation rate. It will be assumed that the inertial angular velocity of the platform is given by:

$$\underline{\omega}_{ip}^{p} = C_n^{\ p} \begin{bmatrix} \dot{\lambda} \cos L \\ - L \\ - \dot{\lambda} \sin L \end{bmatrix} + \begin{bmatrix} 0 \\ 0 \\ \dot{\phi} \end{bmatrix} \tag{48}$$

Thus the constant azimuth rotation rate, $\dot{\phi}$, is defined as relating the platform and navigation coordinates through the relationship:

$$C_p^{\ n} = \begin{bmatrix} \cos \dot{\phi} t & - \sin \dot{\phi} t & 0 \\ \sin \dot{\phi} t & \cos \dot{\phi} t & 0 \\ 0 & 0 & 0 \end{bmatrix} \tag{49}$$

As a practical matter, the azimuth gyro is torqued at the variable inertial rate given by $\dot{\phi} - \dot{\lambda} \sin L$. Note that initial platform alignment with the geographic frame has been assumed.

6. Unipolar System (Ref. 23).

This system has been defined to represent the Collins INS-61B navigation system. It can be considered a special case of the rotating azimuth system above, with the azimuth rotation rate equal to the terrestrial longitude rate. Thus, Equations (48) and (49) apply, with

$$\dot{\phi} = \dot{\ell} \tag{50}$$

7. Wander Azimuth System (Ref. 21).

This system is another special type of rotating azimuth system, which represents the Litton LTN-51 inertial navigator. Again, Equations (48) and (49) apply, but using the azimuth rotation rate

$$\dot{\phi} = \dot{\ell} \sin L \tag{51}$$

5.1.5 INS ALIGNMENT

A variety of alignment and calibration schemes have been developed for the many inertial navigation systems which have evolved over the years. Nevertheless, the vast majority of operational commercial inertial navigation systems employ self-alignment and calibration methods. The basic concept is to utilize two accelerometers and gyroscopes as sensing elements in a closed-loop control system which either physically or analytically determines the angular orientation between the instrument axes and the local geographic frame. These systems take advantage of the fact that at a known, fixed, location on the earth, the earth's gravity and angular velocity vectors are known a priori in the geographic frame and can be measured in instrument axes. The comparison of these physical vectors is sufficient to uniquely specify the orientation between the two axes sets.

The precision of the various self-alignment and calibration methods is determined by the precision of the system implementation; i.e., the angular velocity and specific force uncertainties. Because of the commonality of concept, the resulting steady-state alignment and calibration methods will be basically the same, independent of the details of the mechanization scheme. The use of Kalman filtering techniques does not alter the above conclusion, although optimal methods allow a more rapid attainment of steady-state conditions than conventional gyrocompassing

The use of system self-alignment techniques such as platform leveling and gyrocompass techniques leads to errors in the initial system state vector which depend on the instrument uncertainties. This results in very significant cross-correlation terms in the initial covariance matrix (Ref. 27).

- GYROCOMPASSING

For the purposes of modeling representative inertial systems, it is sufficient to assume that the alignment and calibration schemes employ an acceleration coupled gyrocompassing scheme (Ref. 24) which aligns the instrument axes with geographic axes. The signal flow diagram associated with such a scheme is illustrated in Figure 10, where

K_N, K_E, K_D	are the north, east, and azimuth channel proportional gains, respectively.
$\delta f_N, \delta f_E$	are the north and east specific force uncertainties, respectively.
$\delta\omega_N, \delta\omega_E, \delta\omega_D$	are the north, east, and azimuth angular velocity uncertainties, respectively.
ω_{ie}	is the inertial angular velocity of the earth.
$\tilde{\omega}_N, \tilde{\omega}_E, \tilde{\omega}_D$	are the north, east, and azimuth gyro torquing commands, respectively.

The initial attitude errors at the beginning of alignment have a strong effect on the required solution time, but do not alter the steady-state alignment errors.

With typical values for the proportional alignment gains and reasonable values for the specific force and angular velocity uncertainties, the steady-state alignment errors can be approximated.

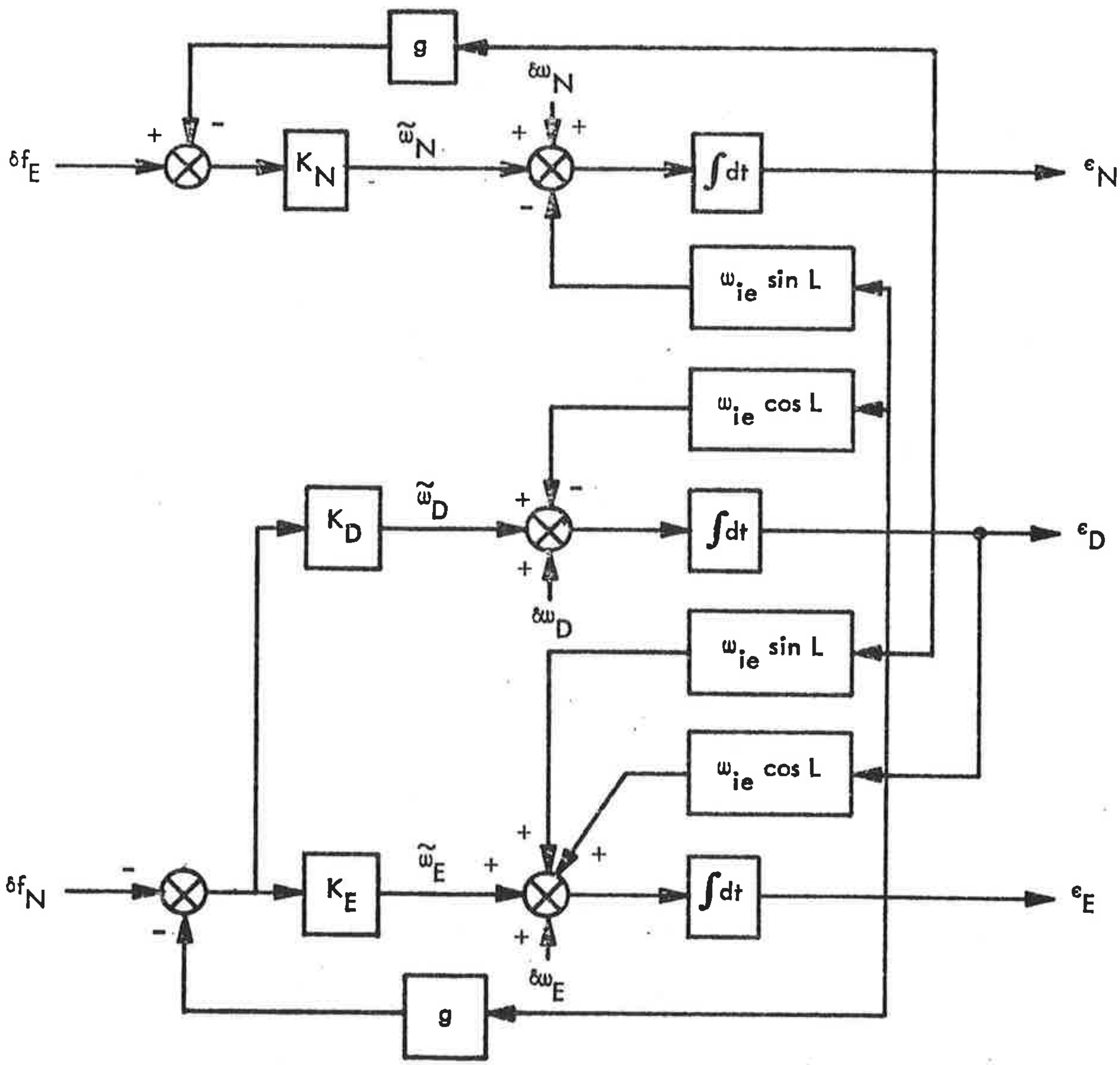

Figure 10. Signal Flow Diagram — Acceleration Coupled Gyrocompass.

$$\epsilon_N \approx \frac{\delta f_E}{g} \tag{52}$$

$$\epsilon_E \approx -\frac{1}{g}\,\delta f_N \tag{53}$$

$$\epsilon_D \approx -\frac{1}{\omega_{ie}\cos L}\,\delta\omega_E - \frac{\tan L}{g}\,\delta f_E \tag{54}$$

The steady-state gyro torquing commands are obtained directly from Figure 10, using the above steady-state attitude errors:

$$\tilde{\omega}_N \approx -\,\delta\omega_N - \frac{\delta f_N}{g}\,\omega_{ie}\sin L \tag{55}$$

$$\tilde{\omega}_E \approx 0 \tag{56}$$

$$\tilde{\omega}_D \approx -\,\delta\omega_D - \frac{\delta f_N}{g}\,\omega_{ie}\cos L \tag{57}$$

Having obtained the initial attitude errors as a function of the angular velocity and specific force uncertainties, it is now a relatively simple matter to compute the initial covariance matrix. The implementation of this method of approach in the context of error analysis is outlined in Reference 26.

- KALMAN FILTERING

The above approach is convenient for initializing the covariance matrix of a simple error simulation of an inertial navigation system. However, in the present program, where the Kalman filter equations are available for updating the hybrid system, these equations can be used to simulate the alignment and calibration process as well. The measurements would consist of almost perfect knowledge of the system's velocity, since the INS would normally be aligned with the aircraft parked at the gate. Blunders such as entering the incorrect aircraft position, and error effects due to aircraft motion, inadequate alignment time, etc. are easily incorporated using the optimal approach for alignment.

The simulation is initialized with very large uncertainties in the INS misalignment angles, remaining after the coarse platform erection process. During the assumed alignment time, the filter uses the velocity measurements to reduce the diagonal elements of the covariance matrix. In doing this, it will also introduce the appropriate cross-correlation terms. Under the same assumptions the steady-state errors would be identical to those obtained with the physical gyrocompass scheme, but the simulation will now have generated its own initial covariance matrix to use at the outset of the navigation mode.

During the simulated INS alignment phase, the two horizontal velocity components are measured. Since these are nominally zero, each measurement consists of INS errors, plus disturbances of the parked aircraft from wind gusts, fueling, loading, etc. The latter are represented as white noises with specified variances. The measurements of northerly and easterly velocities are

$$m_{a\ell n} = r\delta\dot{L} + r_{a\ell n} \tag{58}$$

$$m_{a\ell e} = r \cos L \;\delta\dot{\ell} + r_{a\ell e} \tag{59}$$

where $r_{a\ell n}$ and $r_{a\ell e}$ are the noises in the measurements. The corresponding measurement vectors are (c.f. Equation (7)):

$$\underline{h}^T_{a\ell n} = [0\ 0\ 0\ 0\ 0\ r\ 0\ \ldots\ 0] \tag{60}$$

$$\underline{h}_{a\ell e}^{T} = [0\ 0\ 0\ 0\ 0\ 0\ (r \cos L)\ 0\ \ldots\ 0] \tag{61}$$

Each of these measurements is used, as described in Section 4.2, to update the error covariance matrix. The result obtained using this method will be the same as that obtained using physical gyrocompass techniques, since both systems approach the same steady-state conditions.

5.1.6 TYPICAL INS ERROR MODEL PARAMETERS

The specification of the typical INS error parameter values has been based primarily on an operational inertial navigation system, the Collins INS-61B which is installed in the Douglas DC-10. Table 2 (from Ref. 23) presents a set of component specifications for the Collins system. The required data inputs for the INS model have been discussed above. The process of translating the Collins specifications into the simulation model format will be described in some detail where it is thought that the techniques might not be obvious. This description is intended to be a guide for program users who are not familiar with INS terminology and statistical error descriptions.

The resulting values for the INS model simulation inputs are summarized in Table 3. The names of the corresponding FORTRAN variables referred to in the NATNAV Input Description (Volume 2, Section 7) are included in Table 3 for convenient reference.

- INS CONFIGURATION

The manufacturer labels this mechanization "unipolar". Per the system descriptions, the platform is locally level, but with the platform heading rate equal

Table 2. Error Parameters Used in INS Error Analysis.

Error Parameter	Standard Deviation	*Correlation Time
Accelerometer scale factor		
Level axes	0.075 %	**NA
Vertical axis	0.075 %	**NA
Accelerometer bias		
Level axes	100 μg	**NA
Vertical axis	500 μg	**NA
Accelerometer random		
Level axes	10 μg	20 min
Vertical axis	200 μg	2 hr
Gyro scale factor	0.05 %	**NA
Gyro mass unbalance	0.075 deg/hr/g	**NA
Gyro anisoelastic drifts	0.03 deg/hr/g^2	**NA
Gyro bias		
North axis	0.01 deg/hr	**NA
East axis	0.01 deg/hr	**NA
Vertical axis	0.015 deg/hr	**NA
Gyro random drifts	0.0075 deg/hr	1 hr
Axes misalignment		
Y-accelerometer to Y-gyro	0.15 mrad	**NA
X-Y gyro plane to X-Y accelerometer plane	0.25 mrad	**NA
Z-gyro to X-accelerometer	0.5 mrad	**NA
Z-gyro to Y-accelerometer	0.5 mrad	**NA

*All random errors are assumed to be exponentially correlated.

**NA - Not Applicable.

Table 3. Typical INS Model Inputs.

INS Parameter	NATNAV Input	Value
INS Configuration		
Unipolar Mechanization	ISYS	6
Two-Axis Accelerometer	TWOACC	TRUE
Gyro Drift Errors Present	GYROS	TRUE
Accelerometer Uncertainties Present	ACCEL	TRUE
Gyro Torquer Errors Present	TORQ	TRUE
Geodetic Errors Present	GRAV	TRUE
Altimeter Uncertainty Present	ALTSF	TRUE
*Azimuth Rotation Rate, $\dot{\phi}$	PHIDOT	1. rpm
**Inertial Altitude Weighting Parameter, κ	AKAP	3.
Initial Conditions		
Platform Misalignment Angles (1σ)		
North, ϵ_N	ENØ	1°
East, ϵ_E	EEØ	1°
Down, ϵ_D	EDØ	5°
Position Errors (1σ)		
Latitude, δL	DLAØ	0.2 ft
Longitude, $\delta \ell$	DLOØ	0.2 ft
**Altitude, δh_i	DHØ	2 ft
Rate Errors (1σ)		
Latitude, $\delta \dot{L}$	RDLAØ	0
Longitude, $\delta \dot{\ell}$	RDLOØ	0
**Altitude, $\delta \dot{h}_i$	RDHØ	0

*Required only for rotating azimuth INS mechanization.

**Not required for two-accelerometer model.

Table 3. (Continued).

INS Parameter	NATNAV Input	Value
Gyro Drift Uncertainties		
Correlated Noises (1σ)		
δ_x	SGX	0.0125 °/hr
δ_y	SGY	0.0125 °/hr
δ_z	SGZ	0.0769 °/hr
Correlation Times		
τ_{g_x}	TGX	2 hr
τ_{g_y}	TGY	2 hr
τ_{g_z}	TGZ	2 hr
Strengths of White Noises		
$Q_{w_{g_x}}$	QWGX	9×10^{-8} °/hr
$Q_{w_{g_y}}$	QWGY	9×10^{-8} °/hr
$Q_{w_{g_z}}$	QWGZ	9×10^{-8} °/hr
Accelerometer Uncertainties		
Correlated Noises (1σ)		
α_x	SAX	10^{-4} g
α_y	SAY	10^{-4} g
** α_z	SAZ	1.2×10^{-4} g

**Not required for two-accelerometer model.

Table 3. (Continued).

INS Parameter	NATNAV Input	Value
Accelerometer Uncertainties (Cont.)		
Correlation Times		
τ_{a_x}	TAX	40 min
τ_{a_y}	TAY	40 min
** τ_{a_z}	TAZ	240 min
Strengths of White Noises		
$Q_{w_{a_x}}$	QWAX	0
$Q_{w_{a_y}}$	QWAY	0
** $Q_{w_{a_z}}$	QWAZ	0
Gyro Torquer Uncertainties		
Scale Factors (1σ)		
τ_x	TAUX	0.05 %
τ_y	TAUY	0.05 %
τ_z	TAUZ	0.05 %
Geodetic Uncertainties		
Correlated Noises (1σ)		
North Deflection, ξg	SVX	2.4×10^{-5} g
East Deflection, ηg	SVY	2.4×10^{-5} g
**Magnitude, Δg	SVZ	2.4×10^{-5} g

**Not required for two-accelerometer model.

Table 3. (Continued).

INS Parameter	NATNAV Input	Value
Geodetic Uncertainties (Cont.)		
Correlation Distances		
North Deflection, β_x	DX	20 nm
East Deflection, β_y	DY	20 nm
**Magnitude, β_z	DZ	20 nm
Alignment Uncertainties		
Velocity Measurement Errors (1σ)		
North, $r_{a\ell n}$	SALIN1	0.0222 kt
East, $r_{a\ell e}$	SALIN2	0.0222 kt
Altimeter Uncertainty		
**Scale Factor, τ_h	TAUH	0.3 %

**Not required for two-accelerometer model.

to the terrestrial longitude rate. The system utilizes two 2-degree-of-freedom gyros, a two-axis accelerometer for level specific force sensing, and a single axis vertical accelerometer which is used to provide instantaneous vertical speed. The vertical accelerometer information is not used for computing altitude, the earth's radius, or the earth's gravitational field. Thus this system is, in effect, a two-accelerometer system. All INS component errors are present in the model. The azimuth rotation rate is not required for this mechanization; $\dot{\phi} = 1$ rpm is a typical value for a rotating azimuth system. The inertial altitude weighting parameter κ is only required for three-accelerometer systems; a reasonable value is $\kappa = 3$ (Ref. 24).

- INITIAL CONDITIONS

The initial conditions shown for the INS errors are typical for the aircraft parked at the gate, prior to self-alignment and subsequent to the coarse platform leveling and slewing.

- GYRO DRIFT UNCERTAINTIES

In Table 2, the sources of gyro errors are listed as scale factor, mass unbalance, anisoelastic, bias and random. Scale factor errors are accommodated directly in the program. The gyro drift uncertainties are modeled in the simulation as a combination of uncorrelated and correlated noises. It is therefore necessary to derive an equivalent gyro drift rate standard deviation. The anisoelastic drifts will be inserted as white noise as explained below. Thus the equivalent gyro drift will account for the combined effects of mass unbalance, bias and random drifts.

The effective drift due to gyro mass unbalance can be approximated as a bias, since for systems which utilize locally level platforms, the orientation relative to the gravity field is constant. Moreover, it will be assumed that the spin axis of the level gyro is vertical, effectively eliminating its error due to mass unbalance. Thus, the level gyro bias is 0.01 deg/hr. The mass unbalance effect for the vertical gyro is 0.075 deg/hr in the assumed 1g field. To find the total vertical gyro drift rate, we take the root-sum-squared (RSS) of the mass unbalance and bias drifts to obtain 0.765 deg/hr. The effective bias drifts are now combined with the specified random drift of 0.0075 deg/hr with a one-hour correlation time. The autocorrelation functions for the bias and random effects are sketched in Figure 11. The effects

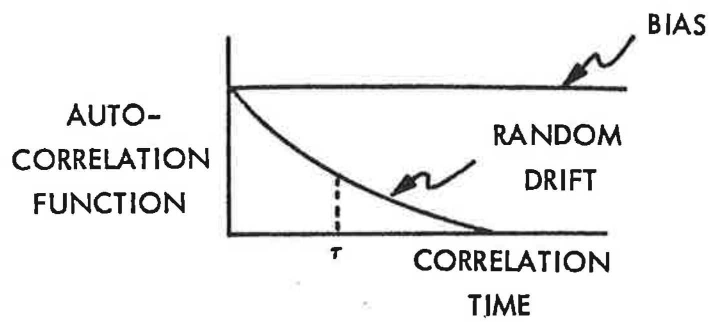

Figure 11. Autocorrelation of Gyro Bias and Random Drift.

of the bias and random components are approximated by RSSing the standard deviations of the two and extending the correlation time by a factor of two from the value of one hour in Table 2. Thus for the level gyros (δ_x, δ_y) we have:

$$[0.01^2 + 0.0075^2]^{1/2} = 0.0125 \text{ deg/hr} \qquad (1\sigma)$$

and for the vertical gyro (δ_z):

$$[0.0765^2 + 0.0075^2]^{1/2} = 0.0769 \text{ deg/hr} \qquad (1\sigma)$$

The white noise in the gyro drift model will be used to account for the effects of the gyro anisoelastic drifts. For systems with local-level platforms, the anisoelastic drifts result from aircraft vibrations and maneuvers. In Table 2 this sensitivity is given as 0.03 deg/hr/g^2. If we assume an excitation level of 0.01 g^2, this gives an effective drift rate of 3×10^{-4} deg/hr. By approximating this error source as white noise, we are taking into account the uncorrelated nature of the maneuver and vibration-caused drifts. The specification of the noise strength presents a problem with units since white noise possesses the dimensions of the quantity squared per unit bandwidth, in this case $(\text{deg/hr})^2/(\text{rad/hr})$. The problem is resolved by equating the mean-squared angular deviations due to the white gyro drift and the anisoelastic drift after a given period of time:

$$Q_{w_{g_i}} t = (3 \times 10^{-4} \text{ deg/hr})^2$$

If this period is taken as one hour,

$$Q_{w_{g_i}} = 9 \times 10^{-8} \text{ deg}^2/\text{hr}$$

It has been empirically determined that for gyroscopes where conservation of angular momentum plays a dominant role, the uncorrelated gyro drift rate is insignificant. However for gyros that may be developed in the future, such as the laser gyro, uncorrelated drift may be more important.

- ACCELEROMETER UNCERTAINTIES

In the same manner as the above, the accelerometer scale factor, bias, and random uncertainties must be combined into an equivalent colored noise for the

INS model. Since the level accelerometer nominally senses zero g's, the accelerometer measurement uncertainties are taken to be equal to the bias uncertainties of 1×10^{-4} g. For the vertical accelerometer, which nominally senses 1g, the scale factor error is combined with the bias error in an RSS fashion. The resulting equivalent biases are 1×10^{-4} g and 9×10^{-4} g for level and vertical accelerometers, respectively. The equivalent bias and the specified random errors are RSSed to obtain the values specified in Table 3 for α_x, α_y and α_z. Again, the two specified random correlation times are increased by a factor of two. No significant white noise is present in the accelerometer specifications.

- GYRO TORQUER UNCERTAINTIES

The gyro scale factor errors in Table 2 are used directly in the simulation model.

- GEODETIC UNCERTAINTIES

The three gravitational uncertainties are assumed to be independent of one another. The values shown in Table 3 were obtained from Reference 27.

- ALIGNMENT UNCERTAINTIES

The measurement noise in sensing velocity during the alignment phase were obtained from Reference 28.

- ALTIMETER UNCERTAINTY

The scale factor error in Table 3 is representative of calibrated commercial-quality altimeters (Ref. 29). The air data system errors will be elaborated upon in Section 5.5.

5.2 DOPPLER RADAR

A Doppler radar determines the velocity of the aircraft with respect to the ground in a reference coordinate system fixed to the aircraft. It operates by measuring the Doppler shift experienced by microwave energy which has been transmitted towards the earth by means of three or more suitably oriented beams, back scattered by the surface, and received at the aircraft. The system requires either an internal or an external vertical reference for conversion of its velocity information into earth coordinates; however, this reference information need not be of high quality. A Doppler navigator is dependent for azimuth information on an external directional sensor, such as a gyromagnetic compass, heading-attitude platform, or astrocompass. For hybrid operation, the INS can provide the necessary attitude angles. The error contributed by the heading reference has a major effect on the overall system error; for example, a 1° error in heading represents a 1.75 percent cross-track position error.

The outputs of the Doppler radar are generally groundspeed, drift angle and, sometimes altitude rate. The principal uncertainties in the Doppler radar data are due to a scale factor error in the groundspeed reading, a bias in the antenna boresight alignment relative to the aircraft, and for oceanic flights the effects of over-water errors. A typical error budget for a high-performance Doppler radar is shown in Table 4 (Ref. 30).

In typical modern Doppler radars the most significant errors are those which occur during operation over water. There are three types of over-water errors. Two of them are due to actual water transport motion; the larger of these is due

Table 4. Typical Error Budget of High Performance Doppler Radar.

Error	Type	Value	Correlation Time
Fluctuation (After 10 nm)	Random	0.073 %	0.25 - 1 sec
Beam Direction (Antenna and Radome)	Bias & Random	0.065 %	1 sec - ∞
Sea Bias (Residual. After Lobe-Switching)	Bias	0.035 %	∞
Altitude Hole (Residual. After Lobe-Switching & Modulation Wobbling)	Bias & Random	0.02 %	1 sec - ∞
Readout (Data Conversion)	Bias	0.02 %	∞
Installation and Calibration	Bias	0.03 %	∞
Frequency Tracker	Bias	0.1 knot	∞
Total Ground Speed Error	0.11 % + 0.1 knot (1σ)		
Total Drift Angle Error	6 min (1σ)		

to surface wind-induced water droplet motion, and the other is due to sea currents. The third over-water error is the calibration shift or sea bias error, which is caused by the large change of the scattering coefficient with incidence angle, within the beamwidth. Several techniques have been developed to greatly reduce this error, the most widely used one being the "lobe-switching" technique (Ref. 31). One limitation of the lobe-switching technique is that it requires a physically azimuth (drift) stabilized antenna in most applications. On the other hand, the trend in modern hybrid systems is in the direction of a fixed Doppler radar antenna, since this leads to smaller size, lower cost and more direct data conversion requirements.

Therefore, other over-water bias compensation techniques have been developed which are useable with fixed antennas, such as the m-tracking technique (Ref. 31).

5.2.1 DOPPLER ERROR MODEL

The Doppler radar measures the forward and sidewise components of the aircraft velocity over the earth's surface, V_{fwd} and V_{side} (see Figure 12):

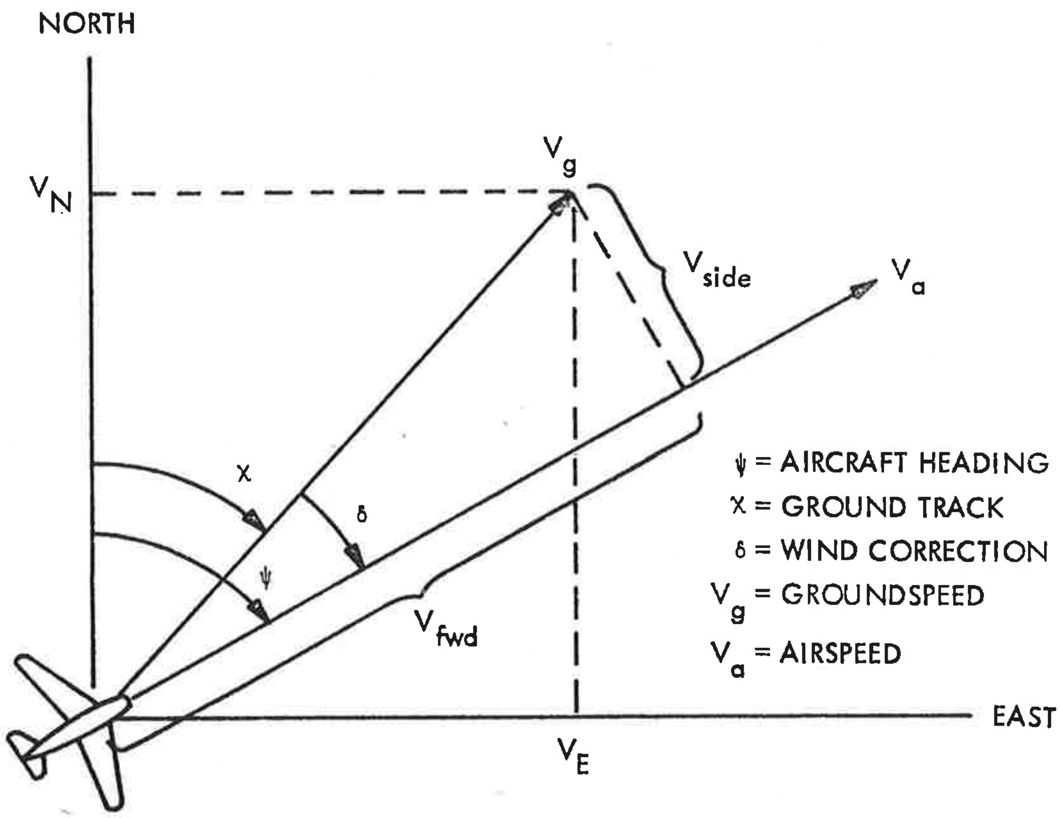

Figure 12. Geometry and Nomenclature for Doppler Radar Measurements.

$$V_{fwd} = V_N \cos \psi + V_E \sin \psi = V_g \cos \delta \tag{62}$$

$$V_{side} = - V_N \sin \psi + V_E \cos \psi = V_g \sin \delta \tag{63}$$

where ψ = aircraft heading angle, and

$$V_N = r \dot{L} \tag{64}$$

$$V_E = r \cos L \, \dot{\ell} \tag{65}$$

$$V_g = \sqrt{V_N^2 + V_E^2} = \text{groundspeed} \tag{66}$$

δ = wind correction angle

The errors in the indicated Doppler velocities are due to INS errors and independent Doppler measurement uncertainties. By taking first-order perturbations of the measured velocities, we obtain the error measurements

$$m_{fwd} = \delta V_N \cos \psi + \delta V_E \sin \psi - (V_g \sin \delta)\epsilon_D + \text{independent forward Doppler measurement errors} \tag{67}$$

$$m_{side} = - \delta V_N \sin \psi + \delta V_E \cos \psi + (V_g \cos \delta)\epsilon_D + \text{independent sidewise Doppler measurement errors} \tag{68}$$

where

$$\epsilon_D = \delta\psi = \text{azimuth error}$$

To obtain the Doppler errors in terms of the INS error state vector, we must convert δV_N and δV_E to latitude and longitude components by using Equations (64) and (65):

$$\delta V_N = r \, \delta\dot{L} + \dot{L} \, \delta h \tag{69}$$

$$\delta V_E = - r\dot{\ell} \sin L \ \delta L + r \cos L \ \delta\dot{\ell} + \dot{\ell} \cos L \ \delta h \tag{70}$$

where $\delta h = \delta h_i$ in a three-accelerometer system, and $\delta h = \delta h_a = \tau_h h$ in a two-accelerometer, local-level system.

The independent errors in the Doppler velocity measurements, Equations (67) and (68), can be generally modeled as a random bias proportional to groundspeed; i.e., a random scale factor error, plus exponentially-correlated noise at the velocity level, plus a white noise in each axis. Thus, using Equations (69) and (70), Equations (67) and (68) can be written as

$$\begin{aligned} m_{fwd} = (V_g \sin \delta)\epsilon_D &- (r\dot{\ell} \sin L \cos \psi)\delta L + (r \cos \psi)\delta\dot{L} \\ &+ (r \cos L \sin \psi)\delta\dot{\ell} + (\dot{L} \cos \psi + \dot{\ell} \cos L \sin \psi)\delta h \\ &+ b_{fwd} V_{fwd} + n_{fwd} + r_{fwd} \end{aligned} \tag{71}$$

$$\begin{aligned} m_{side} = - (V_g \cos \delta)\epsilon_D &- (r\dot{\ell} \sin L \cos \psi)\delta L - (r \sin \psi)\delta\dot{L} \\ &+ (r \cos L \cos \psi)\delta\dot{\ell} + (\dot{\ell} \cos L \cos \psi - \dot{L} \sin \psi)\delta h \\ &+ b_{side} V_{side} + n_{side} + r_{side} \end{aligned} \tag{72}$$

where b_{fwd} and b_{side} are the respective scale factor errors which satisfy:

$$\dot{b}_{fwd} = 0 \tag{73}$$

$$\dot{b}_{side} = 0 \tag{74}$$

The colored noises in the measurements are expressed by

$$\dot{n}_{fwd} = - n_{fwd}/\tau_{fwd} + v_{fwd} \tag{75}$$

$$\dot{n}_{side} = - n_{side}/\tau_{side} + v_{side} \tag{76}$$

where $\tau_{(\,)}$ indicates the correlation time, and the strength of the driving noise $v_{(\,)}$ is determined from Equation (6). The white measurement noises are r_{fwd} and r_{side}.

The four non-white Doppler measurement errors must be augmented to the INS error state vector in Equation (29) to model the hybrid system. Thus, the new 26-element error state vector is

$$\underline{x} = \begin{bmatrix} \underline{x}_{INS} \\ b_{fwd} \\ n_{fwd} \\ b_{side} \\ n_{side} \end{bmatrix} \tag{77}$$

The two Doppler measurement vectors can be obtained by comparing Equation (7) with (71) or (72):

$$\underline{h}_{fwd} = \left[\begin{array}{c} 0 \\ 0 \\ -V_{side} \\ -r\dot{\ell}\sin L\sin\psi \\ 0 \\ r\cos\psi \\ r\cos L\sin\psi \\ (1-\gamma)[\dot{L}\cos\psi+\dot{\ell}\cos L\sin\psi] \\ 0 \\ \vdots \\ \gamma h[\dot{L}\cos\psi+\dot{\ell}\cos L\sin\psi] \\ V_{fwd} \\ 1 \\ 0 \\ \vdots \end{array}\right] \begin{array}{l} \\ \\ \leftarrow \epsilon_D \text{ term} \\ \leftarrow \delta L \text{ term} \\ \\ \leftarrow \delta\dot{L} \text{ term} \\ \leftarrow \delta\dot{\ell} \text{ term} \\ \leftarrow \delta h_i \text{ term} \\ \\ \\ \leftarrow \tau_h \text{ term} \\ \leftarrow b_{fwd} \text{ term} \\ \leftarrow n_{fwd} \text{ term} \\ \\ \\ \end{array} \tag{78}$$

and

$$
\underline{h}_{side} = \left[\begin{array}{c}
0 \\
0 \\
V_{fwd} \\
- r\dot{\ell} \sin L \cos \psi \\
0 \\
- r \sin \psi \\
r \cos L \cos \psi \\
(1 - \gamma)[\dot{\ell} \cos L \cos \psi - \dot{L} \sin \psi] \\
0 \\
\vdots \\
\gamma h[\dot{\ell} \cos L \cos \psi - \dot{L} \sin \psi] \\
0 \\
0 \\
V_{side} \\
1 \\
0 \\
\vdots
\end{array} \right]
\begin{array}{l}
\\
\\
\leftarrow \epsilon_D \text{ term} \\
\leftarrow \delta L \text{ term} \\
\\
\leftarrow \delta \dot{L} \text{ term} \\
\leftarrow \delta \dot{\ell} \text{ term} \\
\leftarrow \delta h_i \text{ term} \\
\\
\\
\leftarrow \tau_h \text{ term} \\
\\
\\
\leftarrow b_{side} \text{ term} \\
\leftarrow n_{side} \text{ term} \\
\\
\\
\end{array}
\qquad (79)
$$

where $\gamma = 0$ for three-accelerometer systems and $\gamma = 1$ for two-accelerometer systems.

5.2.2 TYPICAL DOPPLER ERROR MODEL PARAMETERS

The Doppler radar errors are strongly dependent upon the quality of the airborne equipment. The following estimates are based principally on Reference 31, which is optimistic about future Doppler equipment. Table 5 summarizes some typical values for the Doppler model parameters; the corresponding NATNAV inputs are also presented for convenient reference.

Table 5. Typical Doppler Model Inputs.

Doppler Parameter	NATNAV Input	Value
Scale Factor Errors (1σ)		
Forward, b_{fwd}	SBDF	0.25 %
Side, b_{side}	SBDS	0.50 %
Colored Measurement Noises (1σ)		
Forward, n_{fwd}	SNDF	0.5 kt
Side, n_{side}	SNDS	0.5 kt
Correlation Times		
Forward, τ_{fwd}	TDF	5 min
Side, τ_{side}	TDS	5 min
White Measurement Noises (1σ)		
Forward, r_{fwd}	SRDF	0.1 kt
Side, r_{side}	SRDS	0.1 kt
Update Interval	DTDOP	10 min

The major Doppler error sources are the scale factor errors, which are due to a summation of receiver errors and boresight errors. The colored noises in the Doppler measurements are due to wave motion and propagation shifts. The random noises in the Doppler measurements come from the limit of ability to resolve groundspeed. It is difficult to specify the interval between Doppler updates of the INS because the optimum update time involves many tradeoffs. However, for the purposes of the simulation, a reasonable estimate of 10 minutes has been indicated.

5.3 OMEGA

Omega is a very low frequency (VLF) radio navigation system capable of covering the entire globe with only eight ground stations. Although Omega was developed primarily as a radio navigation system for marine applications, the system has many desirable features which make it suitable for aircraft navigation use. The use of Omega in hybrid navigation systems for the NAT is attractive because of the world-wide coverage, relatively low cost, and relatively constant accuracy when compared to typical INS error growth for oceanic flights. Four Omega stations, covering most of the western hemisphere, are in operation at North Dakota, Hawaii, Trinidad and Norway. By 1974 four more stations should be located in Japan, Argentina, Tasmania and Reunion Island, off the southeast coast of Africa. The total system should be operational by 1975. The eight Omega stations and their actual or assumed locations are shown in Table 6.

The VLF Omega signals, in the range of 10 to 14 kHz, travel for exceptionally long distances — in part because the nature of the signal does not permit it to penetrate the ionosphere and thus become dissipated in space. Very simply, an Omega navigator operates as follows: the Omega receiver compares the phase of signals received from two stations against a local oscillator. The measurement represents the difference in the time of arrival of the signals or, equivalently, the difference in distance to the two stations. The locus of such measurements is a line of position (LOP) on the surface of the earth. The intersection of two such

Table 6. Omega Transmitter Station Locations.

Name	Latitude L	Longitude ℓ
A. Norway	66.4208°N	13.1528°E
B. Trinidad	10.7017°N	61.6390°W
C. Hawaii	21.4057°N	157.8299°W
D. North Dakota	46.3645°N	98.3350°W
E. Reunion*	21.5°S	55.5°E
F. Argentina*	43.2°S	65.3°W
G. N. Tasmania*	42°S	147°E
H. Japan*	34.7°N	129.5°E

*Exact station locations not determined.

loci provides a position fix. Unfortunately, each LOP is not unique, but is determined relative to the nearest zero-phase contour of the two stations. In an Omega system using phase comparison at 10.2 kHz, isophase lines (or lanes) are formed about every 8 nm. Therefore, it is necessary for the Omega navigator to keep track of position to within one lane width. Eventually all Omega stations will use three basic frequencies: 10.2 kHz, 11.33 kHz, and 13.6 kHz. The number of frequencies is intended to solve the ambiguity problem. A two-frequency receiver, using also the 13.6 kHz lines of position, can provide lanes 24 miles apart, by using the beat between 10.2 and 13.6 kHz (3.4 kHz). A three-frequency receiver improves this ambiguity to 72 miles, using the beat between 10.2 and 11.33 kHz (1.13 kHz).

The phase of the VLF signals is remarkably stable, but diurnal variation in the velocity of propagation requires compensation. The primary Omega system errors are due to inaccuracies in the signals measured by the aircraft. An extensive list and description of the Omega error sources, the resulting error magnitudes, and their general time-varying character has been compiled by Scott (Ref. 32). The most significant errors in Omega come from variations in the velocity of propagation, due primarily to changes in the reflecting properties of the ionosphere. Since these depend upon solar radiation, the errors are a strong function of the path, time of day, and time of year. Skywave correction models have been developed which can reduce the RMS error magnitude to less than one nm. However, sudden ionospheric disturbances can cause unpredicted phase anomalies corresponding to several miles in position. Ultimately, it is hoped that at least the diurnal correction can be applied automatically, using a small computer at the receiver.

Another major source of error is broad-band atmospheric noise at the receiver. The long integration times needed to cope with poor signal-to-noise ratios makes implementation difficult in fast aircraft. The accuracy with which the relative phase is determined may be improved by tracking with a long characteristic time. However, the tracker has to be fast enough to keep up with the phase drift due to the aircraft's changing position, to prevent unlocking of the phase tracking loop. Consequently the airborne Omega receiver must be augmented with external velocity information or else decrease the filtering time to prevent unlock and thereby suffer loss of accuracy. The required accuracy of the external velocity information is modest. An inertial sensor may be employed to provide short-term corrections, or this may be provided by inputs from the aircraft's heading and Doppler navigator or airspeed.

5.3.1 OMEGA ERROR MODEL

Each LOP measurement is based on the difference in propagation times of signals from two Omega stations. Denoting these stations as A and B for one LOP, this time difference is

$$t_{AB} = (\tilde{\rho}_A - \rho_B)/\nu \tag{80}$$

where

ν = phase velocity of Omega signals ($\simeq$986.123 ft/μsec)

ρ = geodesic distance between transmitter and receiver

The error in the time difference is

$$\delta t_{AB} = (\delta\rho_A - \delta\rho_B)/\nu \tag{81}$$

The great circle geometry for a single station is shown in Figure 13. The azimuth

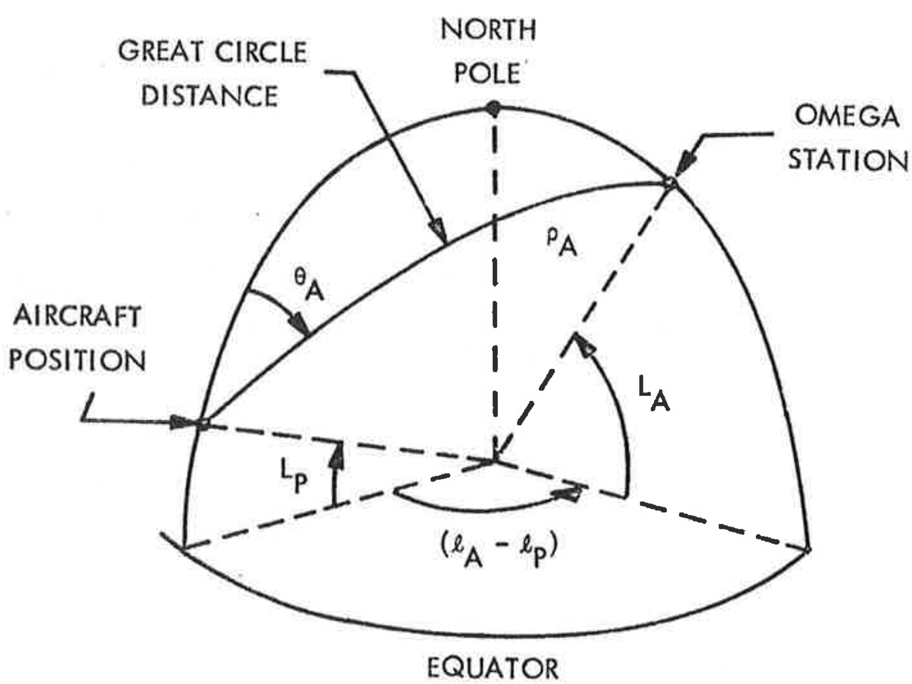

Figure 13. Geometry of Omega Measurement.

of the Omega station (A) measured from the aircraft (P) is

$$\theta_A = \tan^{-1}\left\{\frac{\cos L_A \sin(\ell_A - \ell_P)}{\sin L_A \cos L_P - \cos L_A \cos(\ell_A - \ell_P) \sin L_P}\right\} \tag{82}$$

The azimuth to the second station is obtained using subscript B in Equation (82). The sign of the azimuth is determined as follows:

Quadrant of θ_A	$\tan \theta_A$	$\ell_A - \ell_P$
1	+	+
2	-	+
3	+	-
4	-	-

The error in the great circle distance in terms of latitude and longitude errors is

$$\delta\rho_A = r(\cos\theta_A \ \delta L + \cos L \sin\theta_A \ \delta\ell) \tag{83}$$

Each Omega LOP measurement is assumed to be corrupted by a combination of colored noise, a bias and a white noise. Therefore, using Equation (81), the error in the i-th Omega LOP information is

$$m_{\Omega i} = \frac{r}{\nu}\left[(\cos\theta_{Ai} - \cos\theta_{Bi})\delta L + \cos L(\sin\theta_{Ai} - \sin\theta_{Bi})\delta\ell\right]$$

$$+ b_{\Omega i} + n_{\Omega i} + r_{\Omega i} \tag{84}$$

The independent Omega bias is a random constant for each LOP:

$$\dot{b}_{\Omega i} = 0 \tag{85}$$

The colored noise has a correlation time $\tau_{\Omega i}$:

$$\dot{n}_{\Omega i} = - n_{\Omega i}/\tau_{\Omega i} + v_{\Omega i} \tag{86}$$

and the strength of $v_{\Omega i}$ is again determined from Equation (6).

Assuming two LOP measurements, we must again augment the INS error state vector in Equation (29):

$$\underline{x} = \begin{bmatrix} \underline{x}_{INS} \\ b_{\Omega 1} \\ n_{\Omega 1} \\ b_{\Omega 2} \\ n_{\Omega 2} \end{bmatrix} \tag{87}$$

Thus, from Equations (7), (84) and (87), the measurement vector for each Omega line of position is:

$$
\underline{h}_{\Omega i} = \left[\begin{array}{c} 0 \\ 0 \\ 0 \\ r(\cos\theta_{Ai} - \cos\theta_{Bi})/\nu \\ r\cos L\,(\sin\theta_{Ai} - \sin\theta_{Bi})/\nu \\ 0 \\ \vdots \\ 1 \\ 1 \\ 0 \\ \vdots \end{array}\right] \begin{array}{l} \\ \\ \\ \delta L \text{ term} \\ \delta \ell \text{ term} \\ \\ \\ \text{two Omega measurement} \\ \text{errors} \\ \\ \\ \end{array} \tag{88}
$$

5.3.2 TYPICAL OMEGA ERROR MODEL PARAMETERS

The Omega errors seem to be relatively well-known and documented (e.g., Refs. 32 – 34). At the present time the predominant errors are not greatly affected by the quality of the airborne equipment. Table 7 summarizes some typical Omega error model inputs for NAT applications.

For routes across the North Atlantic, the Omega stations most likely to be used for position fixes are North Dakota-Norway and Trinidad-North Dakota. The bias errors are principally due to station location uncertainties and station syn-

Table 7. Typical Omega Model Inputs.

Omega Parameter	NATNAV Input	Value
Omega Station Pairs		
LOP #1 Norway (A)	IOM1	1
LOP #1 North Dakota (D)	IOM2	4
LOP #2 Trinidad (B)	IOM3	2
LOP #2 North Dakota (D)	IOM4	4
Bias Errors (1σ)		
LOP #1, $b_{\Omega 1}$	SBOM1	1 μsec
LOP #2, $b_{\Omega 2}$	SBOM2	1 μsec
Colored Measurement Noises (1σ)		
LOP #1, $n_{\Omega 1}$	SNOM1	5 μsec
LOP #2, $n_{\Omega 2}$	SNOM2	10 μsec
Correlation Times		
LOP #1, $\tau_{\Omega 1}$	TOM1	30 min
LOP #2, $\tau_{\Omega 2}$	TOM2	30 min
White Measurement Noises (1σ)		
LOP #1, $r_{\Omega 1}$	SROM1	1 μsec
LOP #2, $r_{\Omega 2}$	SROM2	1 μsec
Update Interval	DTOM	20 min

chronization errors. The correlated noises in the Omega measurements are due to errors in predicting diurnal shifts in the propagation velocity, as discussed above. The value for LOP #1 is typical of daytime, while LOP #2 is typical of nighttime propagation. Thus, this selection might be representative of an eastbound flight passing through the terminator. The random error is due to the limit of the receiver to measure phase in the presence of radio noise. Again, the interval between updates cannot be established without additional studies. An initial estimate of 15 minutes seems to provide reasonable results. A comparison of different update intervals is presented in Section 7.

5.4 SATELLITE RANGING

Satellite ranging is a proposed radio navigation system which will provide position, and perhaps velocity, information based on the aircraft's measured distance from two or more satellites. A popular concept is illustrated in Figure 14. The

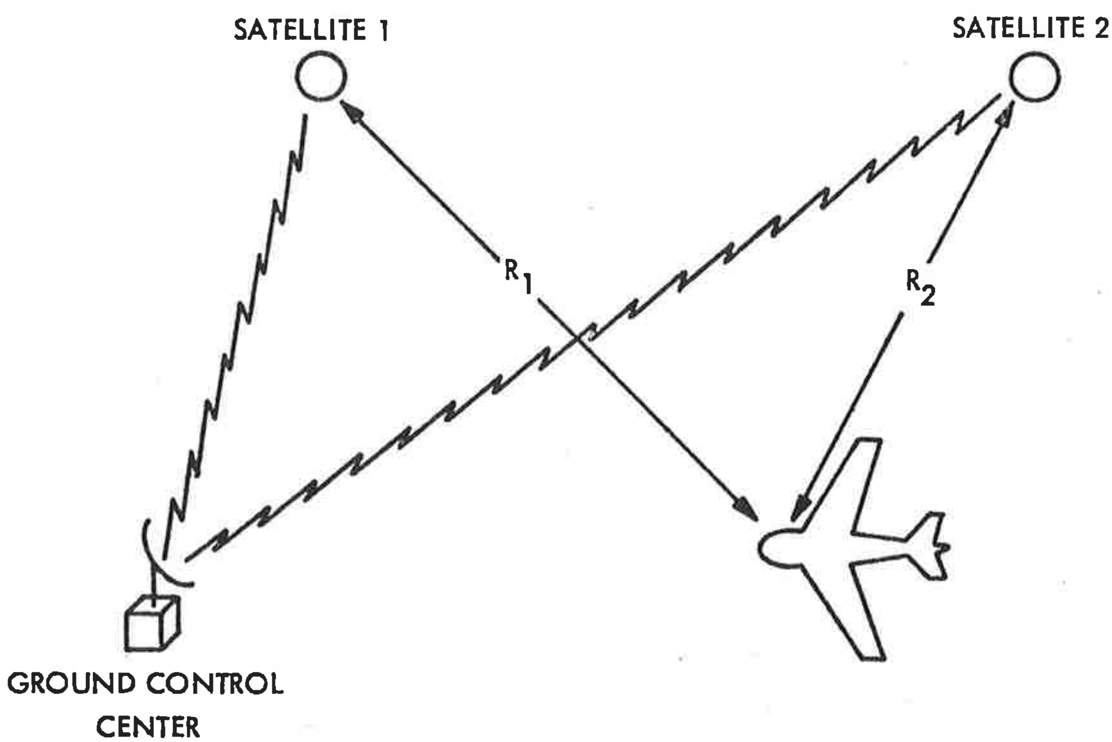

Figure 14. Two-Satellite Ranging System.

ground control center sends coded signals to the aircraft via two or more satellites. A transponder in the aircraft returns these signals to the control center also via the satellites. The lengths of the two paths traveled by the signal are calculated by measuring the time between the emission of the outgoing signal and the receipt of the two returning signals. The ground computer estimates position from the known locations of the satellites and the measured values of R_1 and R_2. It then transmits the position fix to the aircraft and to the ATC center. In order to measure position and aircraft altitude, a system of three satellites is required. In a two-satellite system the aircraft is required to measure its own altitude.

Two alternative systems have been proposed for this navigation-satellite concept (Ref. 35). One system involves 24 satellites at 5,600 nm altitude and 51° inclination. The second system involves only six satellites at synchronous altitudes. The computer program and angle-tracking requirements are somewhat simpler for the synchronous satellite system because of the comparatively slow motion of the satellite. The low-altitude system involves a large number of satellites, and both systems are handicapped by loss of accuracy directly beneath the satellites. One disadvantage of the system is the high peak power required of the satellite transmitter (35 kW). The synchronous system could use directional antennas on the receiving aircraft in order to improve signal characteristics.

Two major factors contribute to uncertainty in a fix determination: satellite position errors and range measurement errors. The accuracy of predicting the position of a satellite in view of all perturbative disturbances depends considerably upon the orbital altitude. With the present knowledge of the earth's gravitational field, the orbits of satellites at 200- to 1,000-km altitude can be predicted 12 hours ahead with a position accuracy on the order of 0.1 to 0.2 nm (Ref. 31). After a full day, extrapolation errors on the order of 0.5 to 0.75 nm can be expected; after four days, the error increases to about three miles. At altitudes of 1,100 km the orbital elements can be predicted one year ahead within 600 ft, but the time at which the satellite arrives at the predicted position is unpredictable within 100 sec per month, because of air drag.

The range measurement contains both a bias error and a random error. The bias error, of the order of 100 ft, includes equipment biases which cannot all be calibrated out and some propagation errors over short time periods that cannot be removed. The random error, which includes equipment noise, atmospheric noise and interference, is approximately 200 ft. Timing errors of one millisecond at worst are expected which, in effect, produce very small satellite shifts along their orbits. Current clock accuracy corresponds to a random drift rate in the range estimate of around 100 feet per day.

Errors in range measurement are also caused by propagation effects, especially refraction in the ionosphere, and by instrumental errors in the measurement of propagation times. Propagation effects are given in Table 8 for normal sunspot

Table 8. Propagation Effects on Satellite-Ranging Measurement Error.

Elevation	Range Error
0 deg	1,620 ft
5 deg	1,550 ft
10 deg	1,450 ft
20 deg	1,130 ft
30 deg	900 ft
40 deg	755 ft

activity and for various elevation angles from user to satellite (Ref. 35). However, this error is predictable and therefore reducible, to the extent that the ionospheric characteristics can be predicted over the region of interest. The seasonal, daily and diurnal variations in the integrated electron density would require continuous ionospheric monitoring.

The frequency of navigation fixes will probably be a function of aircraft velocity stored in the computer at the control center. For example, a supersonic transport would probably require fixes at least every three minutes if it had no dead-reckoning capability. Round-trip travel time to a satellite in synchronous orbit is about 0.4 sec which sets the maximum update rate at about two fixes per second for the satellite system.

5.4.1 SATELLITE-RANGING ERROR MODEL

Satellite ranging provides a position fix by measuring the range from the aircraft to two or more known satellite positions. Figure 15 depicts the geometry for a single satellite-ranging measurement.

In an earth-centered frame, the position vectors to the satellite and the aircraft are

$$\underline{R}^e_{ES} = \begin{bmatrix} \sin L_S \\ \cos L_S \sin (\ell_S - \ell_P) \\ - \cos L_S \cos (\ell_S - \ell_P) \end{bmatrix} (r + h_S) \tag{89}$$

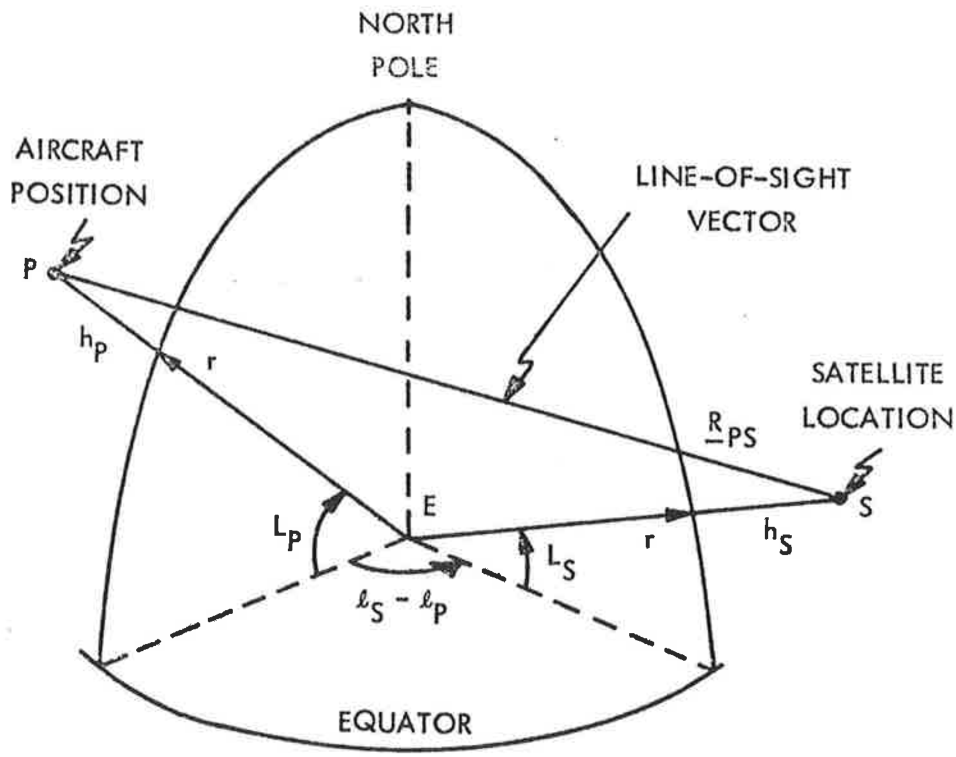

Figure 15. Geometry for Satellite-Ranging Measurement.

$$\underline{R}_{EP}^{e} = \begin{bmatrix} \sin L_P \\ 0 \\ -\cos L_P \end{bmatrix} (r + h_P) \tag{90}$$

The line of sight range to the satellite in the North, East, Down navigation frame is

$$\underline{R}_{PS}^{n} = C_e{}^{n} \left(\underline{R}_{ES}^{e} - \underline{R}_{EP}^{e} \right) \tag{91}$$

where the transformation matrix from the earth to the navigation frame is

$$C_e^{\,n} = \begin{bmatrix} \cos L_P & 0 & \sin L_P \\ 0 & 1 & 0 \\ -\sin L_P & 0 & \cos L_P \end{bmatrix} \tag{92}$$

A unit vector along the range measurement is defined by

$$\underline{u} = \frac{\underline{R}^n_{PS}}{|\underline{R}^n_{PS}|} = \begin{bmatrix} u_N \\ u_E \\ u_D \end{bmatrix} \tag{93}$$

Consequently, the total error in the i-th satellite-ranging measurement is

$$m_{si} = u_{Ni} r\ \delta L + u_{Ei} r \cos L_P\ \delta \ell + u_{Di}\ \delta h + k[b_{si} + n_{si} + r_{si}] \tag{94}$$

where the measurement is assumed to be corrupted by independent timing errors consisting of a bias b_{si}, a colored noise n_{si}, and a white noise r_{si}. The propagation speed of light is:

$$k = 983.567 \text{ ft}/\mu\text{sec} \tag{95}$$

The timing bias and colored noise satisfy

$$\dot{b}_{si} = 0 \tag{96}$$

$$\dot{n}_{si} = -n_{si}/\tau_{si} + v_{si} \tag{97}$$

where τ_{si} is the exponential correlation time, and the strength of v_{si} is determined by Equation (6).

To simplify the satellite-ranging model somewhat, the satellites are assumed to be in synchronous equatorial orbits. This requires, in Equation (89),

$$h_{si} = 19,323 \text{ nm} \tag{98}$$

$$L_{si} = 0 \tag{99}$$

For a two-satellite ranging system, the INS error state vector of Equation (29) must be augmented as before:

$$\underline{x} = \begin{bmatrix} \underline{x}_{INS} \\ b_{s1} \\ n_{s1} \\ b_{s2} \\ n_{s2} \end{bmatrix} \tag{100}$$

Then, using Equations (7), (94) and (100), the measurement vector for satellite ranging is

$$\underline{h}_s = \left[\begin{array}{c} 0 \\ 0 \\ 0 \\ r u_{Ni} \\ r \cos L_p \, u_{Ei} \\ 0 \\ 0 \\ (1-\gamma) u_{Di} \\ 0 \\ \vdots \\ \gamma h u_{Di} \\ 0 \\ \vdots \\ k \\ k \\ 0 \end{array}\right] \begin{array}{l} \\ \\ \\ \delta L \text{ term} \\ \delta \ell \text{ term} \\ \\ \\ \delta h_i \text{ term} \\ \\ \\ \tau_h \text{ term} \\ \\ \\ \text{two satellite timing} \\ \text{measurement errors} \\ \\ \end{array} \tag{101}$$

5.4.2 TYPICAL SATELLITE-RANGING ERROR MODEL PARAMETERS

It is difficult to specify typical numbers with any degree of accuracy since there are no satellite-ranging systems in operation. More detailed knowledge of an actual system will be needed to establish these errors accurately. Table 9 presents some estimated values which have been used in the simulation program. The oper-

Table 9. Typical Satellite-Ranging Model Inputs.

Satellite-Ranging Parameter	NATNAV Input	Value
Satellite Locations (Longitude)		
1st Satellite, ℓ_{s1}	SATLON(1)	10° W
2nd Satellite, ℓ_{s2}	SATLON(2)	70° W
Bias Errors (1σ)		
1st Satellite, b_{s1}	SBSAT1	0.1 μsec
2nd Satellite, b_{s2}	SBSAT2	0.1 μsec
Colored Measurement Noises (1σ)		
1st Satellite, n_{s1}	SNSAT1	0.1 μsec
2nd Satellite, n_{s2}	SNSAT2	0.1 μsec
Correlation Times		
1st Satellite, τ_{s1}	TSAT1	10 min
2nd Satellite, τ_{s2}	TSAT2	10 min
White Measurement Noises (1σ)		
1st Satellite, r_{s1}	SRSAT1	0.1 μsec
2nd Satellite, r_{s2}	SRSAT2	0.1 μsec
Update Interval	DTSAT	20 min

ational errors of a given system may be larger than the estimates presented below, but they will probably not be smaller.

The longitudes of the satellites will be selected from tradeoffs among coverage, geometry, reliability, etc. For consistency, the values shown are the same as those used in Reference 36. The satellite-ranging biases are due to satellite location uncertainties, clock errors and propagation velocity errors. The correlated noises in the measurements are due to equipment errors, and atmospheric effects on the propagation velocity. The random measurement errors are due to limits of the receiver clock. The update interval for satellite-ranging is also very difficult to estimate. It will depend upon the accuracy of an update, the rate of error growth between updates, computational limitations, etc. The value shown in Table 9 has provided reasonable results for the simulation cases examined.

5.5 AIR DATA SYSTEM

The aircraft air data system consists of aerodynamic and thermodynamic sensors, some form of computer and various displays. The outputs of the air data system are indicated values of various flight parameters such as altitude, airspeed or Mach number. Although it is not truly a part of the air data system, the heading indicator is often included in the air data system discussion for convenience. A general block diagram of the air data system is shown in Figure 16, where the inputs are actual values of altitude, altitude rate, airspeed and heading; and the outputs are indicated altitude, altitude rate, airspeed, Mach number and heading, plus calibrated airspeed. For the present simulation, the two models of interest are the altimeter (and vertical speed indicator) errors, and the airspeed errors which are dominated by wind uncertainties.

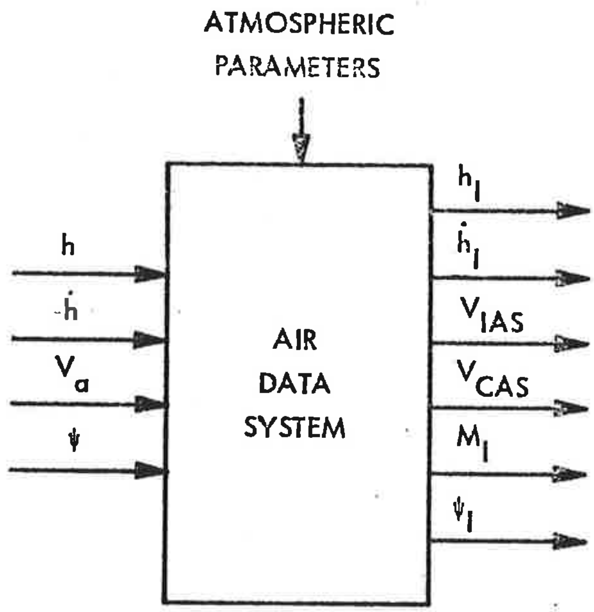

Figure 16. General Block Diagram of Air Data System Model.

5.5.1 ALTIMETRY ERRORS

The barometric altimeter indicates the pressure altitude of the aircraft based on the static pressure measurement and a standard temperature-altitude profile of the atmosphere. Local barometric fluctuations can be corrected for by adjusting the sea-level barometric pressure in flight. All aircraft operating above 18,000 ft MSL use the standard reference sea level pressure of 29.92 in. The principal altimeter errors are due to static defect, non-standard temperature-lapse rate and instrument errors.

The static defect is the difference between the free-stream static pressure and the measured value, and is usually not significant at speeds below about Mach 0.4. A static defect is usually calibrated as a function of Mach number, and automatically corrected for by the air data system. A typical maximum static defect is 350 ft, with a spread of 100 ft among aircraft of the same type (Ref 31). A non-standard temperature-lapse rate will result in an error between true altitude and pressure altitude, but all aircraft will be similarly affected. Therefore lapse-rate errors will not appreciably affect the relative vertical spacing of aircraft.

Altimeter instrument errors, including transducer, computer and indicator errors, have been widely discussed (cf. Ref. 12), especially for altitudes above 30,000 ft. Instrument error is the most significant altimeter uncertainty, and increases with aircraft altitude. The Society of Automotive Engineers (SAE) design objective is an accuracy of 0.2 percent or 25 ft, whichever is greater. The latest Aeronautical Radio Incorporated (ARINC) specifications call for a 3σ instrument error ranging from 15 ft at sea level to 80 ft at 50,000 ft.

The barometric altimeter error is modeled as a scale factor error with

$$\delta h_a = \tau_h h + r_h \tag{102}$$

The scale factor error has been discussed in Section 5.1.2.

The standard vertical speed indicator (VSI), or rate of climb indicator, senses differential changes in the static pressure by means of a calibrated leak. As static pressure changes during entry to a climb or descent, the VSI immediately shows a change of vertical direction. However, until the differential pressure stabilizes, reliable rate indications cannot be obtained. A six- to nine-second lag normally is required to equalize or stabilize the pressures. The instantaneous vertical speed indicator is a recent development which incorporates acceleration pumps to stabilize the pressure differential without the usual lag time. Some INS include a third, vertical accelerometer to provide a more accurate, instantaneous indication of altitude rate. Typical VSI errors are estimated to be about 5 percent to 10 percent of the altitude rate. ARINC specifications call for an accuracy of 30 ft/min or

5 percent, whichever is greater.

The uncertainty in a particular VSI is modeled as a fixed scale factor error with additive white noise:

$$\delta\dot{h}_a = \tau_{\dot{h}}\dot{h} + r_{\dot{h}} \tag{103}$$

The pressure stabilization lag time is not included in the model, since it is negligible in the time frame of interest for the navigation simulation.

5.5.2 AIRSPEED ERRORS

Normally, airspeed and heading information are used with the inertial navigation system only to estimate the local wind. Should the INS fail, then the airspeed and heading can be used for standard dead-reckoning navigation. The air data system errors in velocity measurements are caused by winds and by airspeed and heading instrument errors. In all practical cases the winds will dominate the airspeed and heading errors, so it is not worthwhile to pursue detailed models for the airspeed and heading instrument errors.

Neglecting the errors in the airspeed and heading indicators, the errors in the velocity information from the air data system become identical to the unknown wind. Only the slowly-varying, high-magnitude winds are of concern, since high-frequency gusts produce no net displacement of the aircraft. Experimental data regarding winds in the North Atlantic seem to verify the intuitive model of the wind components as exponentially-correlated processes at the velocity level (Ref. 37). It was observed, however, that there is significant cross-correlation between the north and east components. It is reasonable to expect that the components of the predicted wind would also be correlated with one another but that the components of the error in the predicted wind would not be. The error in the predicted wind is due to the inability of the meteorologist to accurately measure and model the atmosphere. There is no causal connection between the error he makes and the statistical variation of the wind from day to day. For this reason the initial components of the wind uncertainty will be assumed uncorrelated. Thus, the uncertainties in the north and east wind components are modeled as:

$$\delta\dot{V}_{wn} = -\left(\frac{V_g}{d_{wn}}\right)\delta V_{wn} + v_{wn} \tag{104}$$

$$\delta\dot{V}_{we} = -\left(\frac{V_g}{d_{we}}\right)\delta V_{we} + v_{we} \tag{105}$$

where d_{wn} and d_{we} are the correlation distances of the winds. The resulting uncertainties in latitude and longitude rates are

$$\delta\dot{L} = \delta V_{wn}/r \tag{106}$$

$$\delta\dot{\ell} = \delta V_{we}/(r \cos L) \tag{107}$$

Taking the derivatives of Equations (106) and (107), and using (104) and (105), we obtain

$$\delta\ddot{L} = -\left(\frac{V_g}{d_{wn}} + \frac{\dot{h}}{r}\right)\delta\dot{L} + \frac{v_{wn}}{r} \tag{108}$$

$$\delta\ddot{\ell} = -\left(\frac{V_g}{d_{we}} + \frac{\dot{h}}{r} - \dot{L}\tan L\right)\delta\dot{\ell} + \frac{v_{we}}{r\cos L} \tag{109}$$

To implement this dead-reckoning navigation mode in the simulation, in place of the INS, rows 6 and 7 of Equation (18) are modified to represent Equations (108) and (109):

$$F_\epsilon = \begin{bmatrix} 0 & f_{12} & f_{13} & f_{14} & 0 & 0 & f_{17} & 0 & 0 \\ f_{21} & 0 & f_{23} & 0 & 0 & -1 & 0 & 0 & 0 \\ f_{31} & f_{32} & 0 & f_{34} & 0 & 0 & f_{37} & 0 & 0 \\ 0 & 0 & 0 & 0 & 0 & 1 & 0 & 0 & 0 \\ 0 & 0 & 0 & 0 & 0 & 0 & 1 & 0 & 0 \\ 0 & 0 & 0 & 0 & 0 & f_{66} & 0 & 0 & 0 \\ 0 & 0 & 0 & 0 & 0 & 0 & f_{77} & 0 & 0 \\ 0 & 0 & 0 & 0 & 0 & 0 & 0 & 0 & 0 \\ f_{91} & f_{92} & 0 & f_{94} & 0 & f_{96} & f_{97} & f_{98} & 0 \end{bmatrix} \qquad (110)$$

where f_{66} and f_{77} are the coefficients, respectively, of $\delta\dot{L}$ and $\delta\dot{\ell}$ in Equations (108) and (109). Also, the random accelerometer noises w_{ax} and w_{ay} are replaced with v_{wn} and v_{we}. The strengths of these are calculated from the wind statistics with Equation (6). The error in the heading reference is represented by ϵ_D.

5.5.3 TYPICAL AIR DATA ERROR MODEL PARAMETERS

Table 10 presents typical values for the air data model error parameters. The errors in the altimeter and VSI are representative of airline quality equipment. The wind uncertainties are based on Reference 37.

5.6 COMPLETE ERROR MODEL SUMMARY

To simulate the situation of a three-dimensional INS with updates provided

Table 10. Typical Air Data Model Inputs.

Air Data Parameter	NATNAV Input	Value
Altimetry Uncertainties		
Altimeter (1σ)		
Scale Factor, τ_h	TAUH	0.3 %
White Noise, r_h	SALT	10.0 ft
Vertical Speed Indicator (1σ)		
Scale Factor, $\tau_{\dot{h}}$	TAUHD	5.0 %
White Noise, $r_{\dot{h}}$	SALTD	50.0 fpm
Wind Uncertainties (Dead-Reckoning)		
Correlated Wind Errors (1σ)		
North, δV_{wn}	SVWN	15 kt
East, δV_{we}	SVWE	15 kt
Correlation Distances		
North, d_{wn}	DVWN	800 nm
East, d_{we}	DVWE	800 nm

by Doppler, Omega and satellite-ranging measurements, the INS error state vector in Equation (29) must be augmented with 12 additional error state variables. Including the six biases or scale factor errors and the six correlated measurement noises, the complete error-state vector has 34 elements, as shown in Figure 17. The linear error state dynamics are described by Equation (1) in Section 4

$\underline{x} =$

State	Description	Subsystem	Error class
ϵ_N	platform tilt		INS system errors
ϵ_E			
ϵ_D			
δL	latitude		
$\delta \ell$	longitude		
$\delta \dot{L}$	latitude rate		
$\delta \dot{\ell}$	longitude rate		
δh	altitude		
$\delta \dot{h}$	altitude rate		
δ_x	gyro drifts		INS component errors
δ_y			
δ_z			
α_x	accelerometer uncertainties		
α_y			
α_z			
τ_x	gyro torquer scale factor		
τ_y			
τ_z			
ξ_g	geodetic uncertainties		
η_g			
Δg			
τ_h	altimeter scale factor		Independent Measurement Errors
b_{fwd}	fwd. scale factor	Doppler	
n_{fwd}	fwd. correlated noise		
b_{side}	side scale factor		
n_{side}	side correlated noise		
$b_{\Omega 1}$	LOP #1 bias	Omega	
$n_{\Omega 1}$	LOP #1 correlated noise		
$b_{\Omega 2}$	LOP #2 bias		
$n_{\Omega 2}$	LOP #2 correlated noise		
b_{s1}	timing bias #1	Satellite Ranging	
n_{s1}	correlated noise #1		
b_{s2}	timing bias #2		
n_{s2}	correlated noise #2		

Figure 17. Augmented Error State Vector.

$$\underline{\dot{x}} = F\underline{x} + G\underline{w} \tag{1}$$

where F is the 34×34 system matrix, $\underline{w}$ is a 21-element vector of driving white noises, and G is the 34×21 forcing matrix. The noise vector $\underline{w}$ is shown in Figure 18. The non-zero elements of the F and G matrices are shown in Figures 19 and 20. The nomenclature in these equations (Ref. 24) is defined at the beginning of this report. The north, east and down components of the specific force vector sensed by the INS are

$$f_N = r\ddot{L} + 2\dot{h}\dot{L} + \frac{1}{2} r\dot{\ell}(\dot{\lambda} + \omega_{ie}) \sin 2L \tag{111}$$

$$f_E = r\ddot{\ell} \cos L - 2r\dot{L}\dot{\lambda} \sin L + 2\dot{h}\dot{\lambda} \cos L \tag{112}$$

$$f_D = - \ddot{h} + r\dot{\ell}(\dot{\lambda} + \omega_{ie}) \cos^2 L + r\dot{L}^2 - g \tag{113}$$

where the celestial longitude rate is

$$\dot{\lambda} = \dot{\ell} + \omega_{ie} \tag{114}$$

In the simulation, the acceleration terms $(\ddot{L}, \ddot{\ell}, \ddot{h})$ are neglected since they occur so rapidly, relative to the time intervals of interest for navigation analyses.

$$\underline{w} = \begin{array}{ll} \begin{bmatrix} w_{g_x} \\ w_{g_y} \\ w_{g_z} \\ w_{a_x} \\ w_{a_y} \\ w_{a_z} \\ v_{g_x} \\ v_{g_y} \\ v_{g_z} \\ v_{a_x} \\ v_{a_y} \\ v_{a_z} \\ v_x \\ v_y \\ v_z \\ v_{df} \\ v_{ds} \\ v_{\Omega 1} \\ v_{\Omega 2} \\ v_{s1} \\ v_{s2} \end{bmatrix} & \begin{array}{l} \left.\begin{matrix} \vphantom{w_{g_x}} \\ \vphantom{w_{g_y}} \\ \vphantom{w_{g_z}} \end{matrix}\right\} \text{gyro random noise} \\ \left.\begin{matrix} \vphantom{w_{a_x}} \\ \vphantom{w_{a_y}} \\ \vphantom{w_{a_z}} \end{matrix}\right\} \text{accelerometer random noise} \\ \left.\begin{matrix} \vphantom{v_{g_x}} \\ \vphantom{v_{g_y}} \\ \vphantom{v_{g_z}} \end{matrix}\right\} \text{gyro correlated noise} \\ \left.\begin{matrix} \vphantom{v_{a_x}} \\ \vphantom{v_{a_y}} \\ \vphantom{v_{a_z}} \end{matrix}\right\} \text{accelerometer correlated noise} \\ \left.\begin{matrix} \vphantom{v_x} \\ \vphantom{v_y} \\ \vphantom{v_z} \end{matrix}\right\} \text{geodetic correlated error} \\ \left.\begin{matrix} \vphantom{v_{df}} \\ \vphantom{v_{ds}} \end{matrix}\right\} \text{Doppler correlated noise} \\ \left.\begin{matrix} \vphantom{v_{\Omega 1}} \\ \vphantom{v_{\Omega 2}} \end{matrix}\right\} \text{Omega correlated noise} \\ \left.\begin{matrix} \vphantom{v_{s1}} \\ \vphantom{v_{s2}} \end{matrix}\right\} \text{satellite correlated noise} \end{array} \end{array}$$

Figure 18. Driving Noise Vector.

$f_{1,2} = -\dot{\lambda} \sin L$

$f_{1,3} = \dot{L}$

$f_{1,4} = -\dot{\lambda} \sin L = f_{1,2}$

$f_{1,7} = \cos L$

$f_{1,10} = C_{11}$

$f_{1,11} = C_{12}$

$f_{1,12} = C_{13}$

$f_{1,16} = C_{11}\omega_x$

$f_{1,17} = C_{12}\omega_y$

$f_{1,18} = C_{13}\omega_z$

$f_{2,1} = \dot{\lambda} \sin L = -f_{1,2}$

$f_{2,3} = \dot{\lambda} \cos L$

$f_{2,6} = -1$

$f_{2,10} = C_{21}$

$f_{2,11} = C_{22}$

$f_{2,12} = C_{23}$

$f_{2,16} = C_{21}\omega_x$

$f_{2,17} = C_{22}\omega_y$

$f_{2,18} = C_{23}\omega_z$

$f_{3,1} = -\dot{L} = -f_{1,3}$

$f_{3,2} = -\dot{\lambda} \cos L = -f_{2,3}$

$f_{3,4} = -\dot{\lambda} \cos L = f_{3,2}$

$f_{3,7} = -\sin L$

$f_{3,10} = C_{31}$

$f_{3,11} = C_{32}$

$f_{3,12} = C_{33}$

$f_{3,16} = C_{31}\omega_x$

$f_{3,17} = C_{32}\omega_y$

$f_{3,18} = C_{33}\omega_z$

$f_{4,6} = 1$

$f_{5,7} = 1$

$f_{6,2} = -f_D/r$

$f_{6,3} = f_E/r$

$f_{6,4} = -\dot{\ell}(\dot{\ell} + 2\omega_{ie}) \cos 2L$

$f_{6,6} = -2\dot{h}/r$

$f_{6,7} = -\dot{\lambda} \sin 2L$

$f_{6,8} = -\frac{1}{r} [\ddot{L} + \frac{1}{2}\dot{\ell}(\dot{\ell} + 2\omega_{ie}) \sin 2L]$

$f_{6,9} = -2\dot{L}/r$

Figure 19. Non-Zero F-Matrix Elements.

$f_{6,13} = C_{11}/r$

$f_{6,14} = C_{12}/r$

$f_{6,15} = C_{13}/r$

$f_{6,19} = -1/r$

$f_{6,22} = f_{6,8}h + f_{6,9}\dot{h}$ *

$f_{7,1} = f_D/r \cos L$

$f_{7,3} = -f_N/r \cos L$

$f_{7,4} = (\ddot{\ell} + 2\dot{\lambda}\dot{h}/r + 2\dot{L}\dot{\lambda} \cot L) \tan L$

$f_{7,6} = 2\dot{\lambda} \tan L$

$f_{7,7} = -2(\dot{h}/r - \dot{L} \tan L)$

$f_{7,8} = -\frac{1}{r}(\ddot{\ell} - 2\dot{L}\dot{\lambda} \tan L)$

$f_{7,9} = -2\dot{\lambda}/r$

$f_{7,13} = C_{21}/r \cos L$

$f_{7,14} = C_{22}/r \cos L$

$f_{7,15} = C_{23}/r \cos L$

$f_{7,20} = 1/r \cos L$

$f_{7,22} = f_{7,8}h + f_{7,9}\dot{h}$ *

$f_{8,9} = 1$

$f_{9,1} = f_E$

$f_{9,2} = -f_N$

$f_{9,4} = -r\dot{\ell}(\dot{\ell} + 2\omega_{ie}) \sin 2L$

$f_{9,6} = 2r\dot{L}$

$f_{9,7} = 2r\dot{\lambda} \cos^2 L$

$f_{9,8} = \dot{L}^2 + \dot{\ell}(\dot{\ell} + 2\omega_{ie}) \cos^2 L - (\kappa - 2)\omega_s^2$

$f_{9,13} = -C_{31}$

$f_{9,14} = -C_{32}$

$f_{9,15} = -C_{33}$

$f_{9,21} = 1$

$f_{9,22} = \kappa\omega_s^2 h$

$f_{10,10} = -1/\tau_{gx}$

$f_{11,11} = -1/\tau_{gy}$

$f_{12,12} = -1/\tau_{gz}$

$f_{13,13} = -1/\tau_{ax}$

$f_{14,14} = -1/\tau_{ay}$

$f_{15,15} = -1/\tau_{az}$

$f_{19,19} = -1/\beta_x$

---

* two-accelerometer systems only

Figure 19. (Continued).

$$f_{20,20} = -1/\beta_y \qquad f_{28,28} = -1/\tau_{\Omega 1}$$

$$f_{21,21} = -1/\beta_z \qquad f_{30,30} = -1/\tau_{\Omega 2}$$

$$f_{24,24} = -1/\tau_{df} \qquad f_{32,32} = -1/\tau_{s1}$$

$$f_{26\ 26} = -1/\tau_{ds} \qquad f_{34,34} = -1/\tau_{s2}$$

Figure 19. (Continued).

$g_{1,1} = C_{11}$

$g_{1,2} = C_{12}$

$g_{1,3} = C_{13}$

$g_{2,1} = C_{21}$

$g_{2,2} = C_{22}$

$g_{2,3} = C_{23}$

$g_{3,1} = C_{31}$

$g_{3,2} = C_{32}$

$g_{3,3} = C_{33}$

$g_{6,3} = C_{11}/r$

$g_{6,4} = C_{12}/r$

$g_{6,5} = C_{13}/r$

$g_{7,3} = C_{21}/r \cos L$

$g_{7,4} = C_{22}/r \cos L$

$g_{7,5} = C_{23}/r \cos L$

$g_{9,3} = - C_{31}$

$g_{9,4} = - C_{32}$

$g_{9,5} = - C_{33}$

$g_{10,7} = 1$

$g_{11,8} = 1$

$g_{12,9} = 1$

$g_{13,10} = 1$

$g_{14,11} = 1$

$g_{15,12} = 1$

$g_{19,13} = 1$

$g_{20,14} = 1$

$g_{21,15} = 1$

$g_{24,16} = 1$

$g_{26,17} = 1$

$g_{28,18} = 1$

$g_{30,19} = 1$

$g_{32,20} = 1$

$g_{34,21} = 1$

Figure 20. Non-Zero G-Matrix Elements.

SECTION 6

THE SIMULATION PROGRAM

The error models and analysis techniques described in the previous sections have been implemented in a digital computer simulation program entitled NATNAV (North ATlantic NAVigation). This section presents a general description of the simulation program, and some additional analytical development which was not covered in the previous sections. The second volume of this report is a user's manual for NATNAV; it contains programming and operating details of the simulation.

6.1 GENERAL DESCRIPTION OF NATNAV

The digital computer simulation program NATNAV was developed to analyze various inertial aircraft navigation systems utilizing external measurements of position and/or velocity from the following sources:

- Doppler Radar
- Air Data
- OMEGA
- Satellite Surveillance (two-satellite ranging)

Since the mechanization details of the hybrid navigation systems to be analyzed cannot be specifically defined a priori, the simulation program had to be broad enough in scope to encompass all of the likely configurations, to allow for contingencies such as subsystem failures and blunders, and to enable evaluation of variable update rates, suboptimal filtering schemes, aircraft maneuvers, etc. The program was therefore developed with a highly modular structure for maximum flexibility.

The program provides for an optimum initial alignment of the INS prior to taxi. A dead-reckoning option; i.e., no INS is also available. Independent measurements using Doppler radar, Omega or satellite-ranging may be used to update the position and velocity estimates using the optimum recursive Kalman filter. As an alternative, suboptimum filter gains may be used. The operation of the simulation is controlled by the various program inputs. The user must specify the nominal flight plan, the INS configuration and error statistics, and the aiding systems and their characteristics. Figure 21 presents a very general summary of the simulation inputs and outputs; a complete description of all the input/output quantities is contained in Volume II.

The general organization and logical operation of NATNAV are illustrated by the overall flow diagram in Figure 22. The modular structure of the simulation is shown by the block diagram in Figure 23, which depicts the interrelationships of the main program and each of the subprograms. Brief abstracts of each of the programs are presented in Table 11.

Very simply, the simulation performs four principal operations:

- Calculating the time histories of the nominal aircraft position and velocity, upon which the error covariances are based.
- Integrating the differential equations which describe the propagation of the error covariance matrix; i.e., Equation (1).
- Updating the covariance matrix with the appropriate measurement information.
- Presenting the hybrid navigation system position and velocity errors suitably resolved into along-track, cross-track and vertical components.

Each of these basic operations is discussed further in subsequent sections.

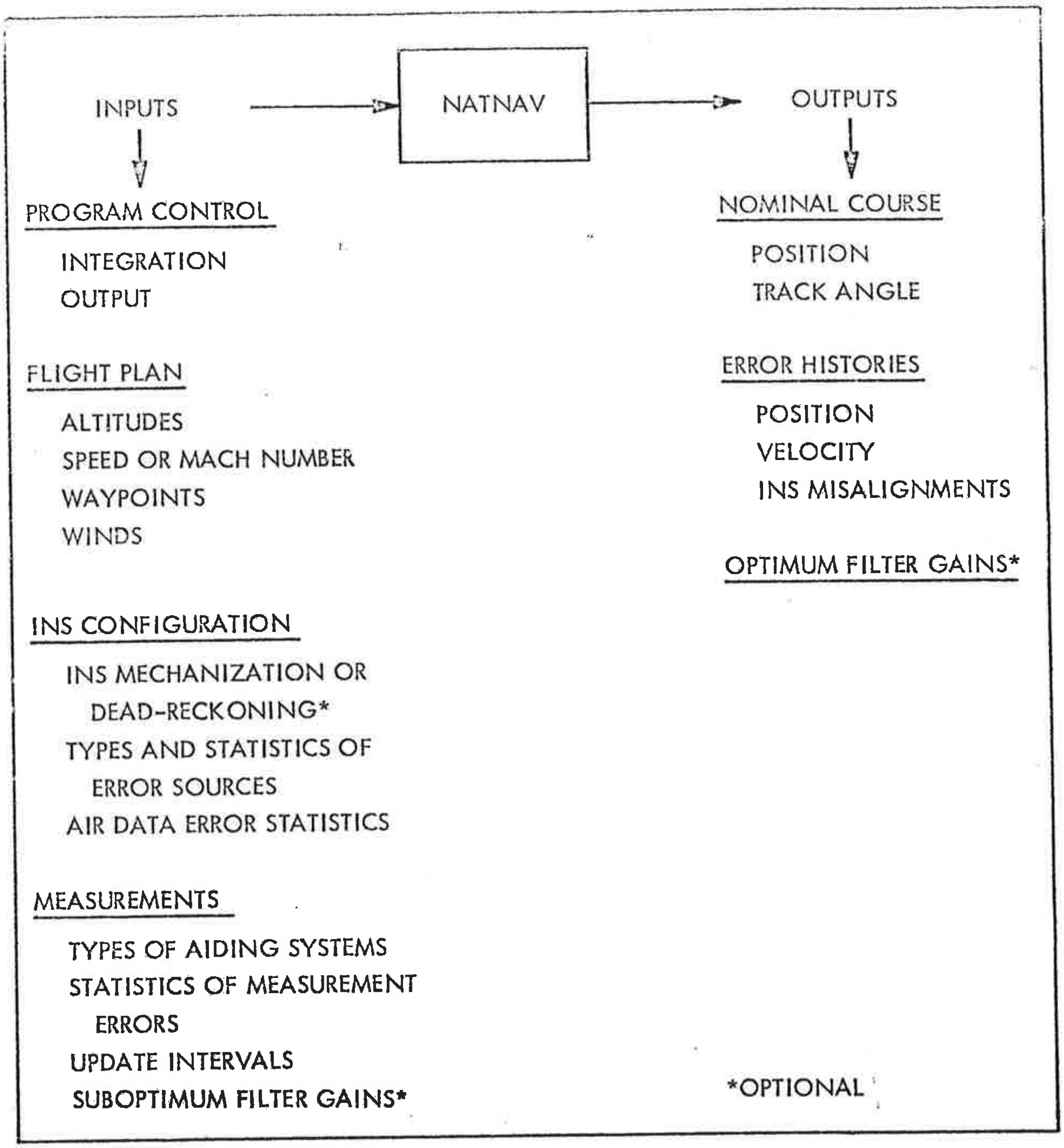

Figure 21. Summary of NATNAV Inputs and Outputs.

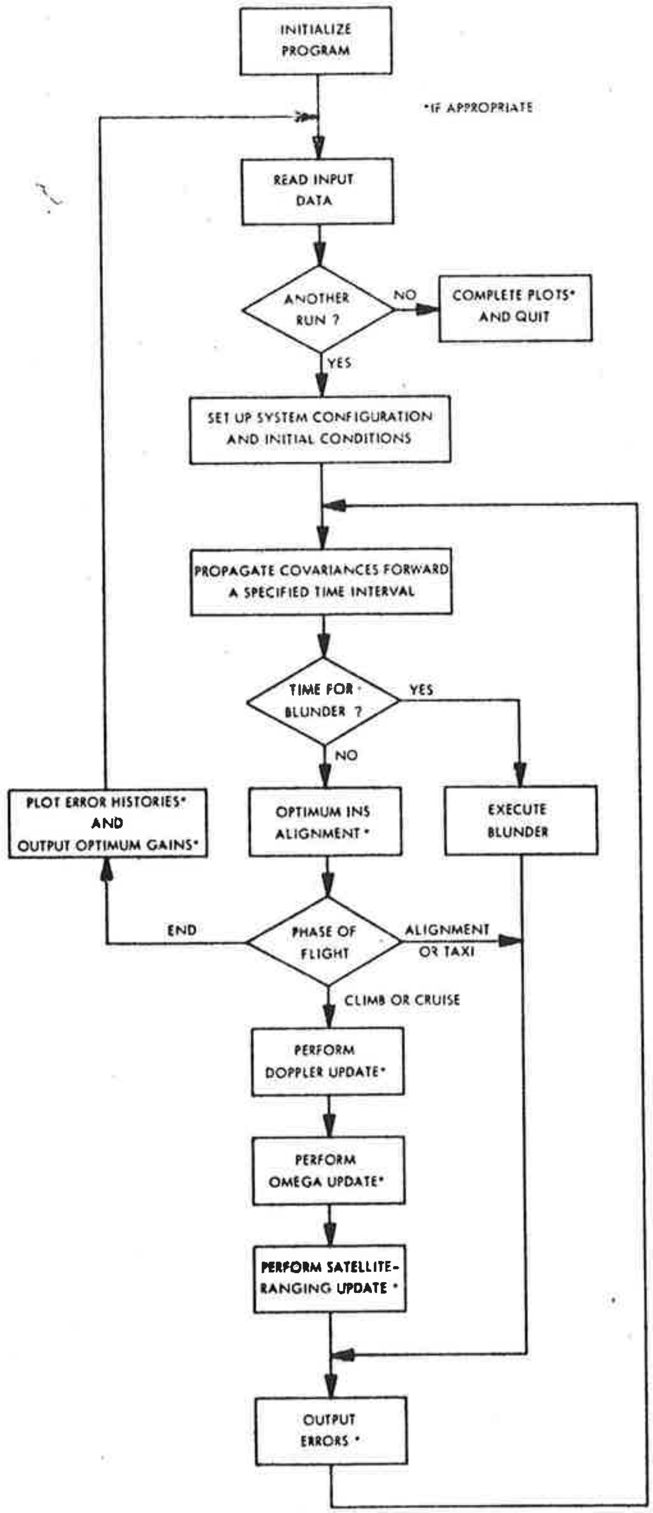

Figure 22. General Flow Diagram of Program NATNAV.

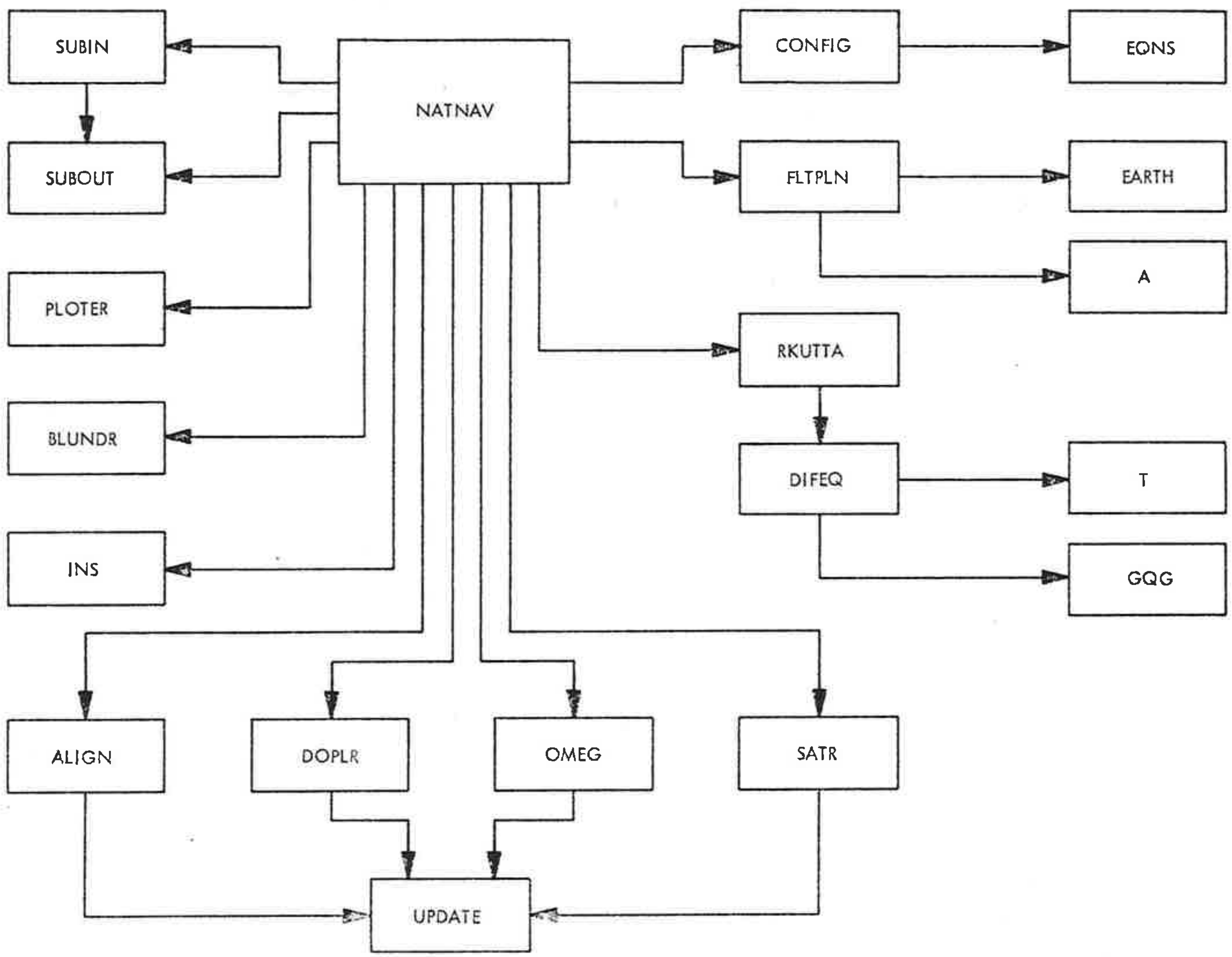

Figure 23. Modular Structure of Program NATNAV.

Table 11. NATNAV Program Abstracts.

NATNAV	Initializes the simulation, regulates the integration of the covariance terms, controls the measurement updates and governs the print and plot outputs. [Main Program]
SUBIN	Reads all input data and documents it on the printed output. [Called by NATNAV]
SUBOUT	Prints time histories of the position and velocity errors in track-referenced coordinates. Also saves data for plotting at completion of run. [Called by NATNAV and SUBIN]
EQNS	Initializes the array of covariance elements to be propagated, and sets the indices for integrating the appropriate differential equations. [Called by CONFIG]
CONFIG	Establishes the array of covariance elements to be integrated for the system configuration selected by the user. [Called by NATNAV]
FLTPLN	Calculates the nominal position, speed, track and heading of the aircraft as functions of time, assuming constant velocity between waypoints. [Called by NATNAV]
EARTH	Calculates the approximate geocentric distance and gravitational acceleration as functions of latitude and altitude. [Called by FLTPLN]
A	Calculates local speed of sound as function of altitude. [Called by FLTPLN]
INS	Initializes the INS covariances and driving noise strengths; calculates the system matrix elements, transformation matrix and torquing rates for the INS. [Called by NATNAV]
ALIGN	Calculates the measurement vectors and optimal filter gains for updating the covariance matrix during the alignment phase. [Called by NATNAV]
DOPLR	Calculates the measurement vectors and optimal filter gains for Doppler radar measurements. [Called by NATNAV]
OMEG	Calculates the measurement vectors and optimal filter gains for two Omega line-of-position measurements. [Called by NATNAV]
SATR	Calculates the measurement vectors and optimal filter gains for two satellite-ranging measurements. [Called by NATNAV]

Table 11. (Continued).

UPDATE	Updates the covariance matrix for optimum or suboptimum measurements. Stores optimum filter gains for printout if desired. [Called by ALIGN, DOPLR, OMEG, SATR]
RKUTTA	Integrates the covariance differential equations using a fourth-order Runge-Kutta procedure. [Called by NATNAV]
DIFEQ	Calculates the derivatives of the covariance elements. [Called by RKUTTA]
T	Calculates the elements of the matrix product $F \times P$. [Called by DIFEQ]
GQG	Calculates the elements of the noise matrix product $G \times Q \times G^T$. [Called by DIFEQ]
BLUNDR	Sets the new system error quantities after the occurrence of a specified blunder or malfunction. Supplied by user. [Called by NATNAV]
PLOTER	Plots the time histories of the position and velocity errors in track-referenced coordinates, if desired. [Called by NATNAV]

6.2 NOMINAL FLIGHT PLAN

The nominal time histories of the actual aircraft position and velocity, upon which the error covariances are based, are generated from an input flight plan. The content of this flight plan closely resembles the information normally provided by actual flight plans, with certain additional data being required. The flight plan inputs are summarized in Table 12.

Table 12. Flight Plan Input Data.

Inputs	Description
Δt_a	INS Alignment Time (min)
Δt_t	Taxi Time (min)
h_0	Airport Elevation, or Initial Altitude (ft)
$V_{c\ell}$	Climb Speed (kt)
$\dot{h}_{c\ell}$	Rate of Climb (ft/min)
M_{cr}	Cruise Mach Number
h_{cr}	Cruise Altitude (ft)
	<u>Route of Flight</u>
n	Number of Waypoints, Including Departure Point
L_i	Latitude of i-th Waypoint (deg)
ℓ_i	Longitude of i-th Waypoint (deg)
V_{w_i}	Windspeed at i-th Waypoint (kt)
θ_{w_i}	Wind Direction at i-th Waypoint (deg)
	$\}$ $i = 1, 2, \ldots n$

During the INS alignment time, nearly perfect position and velocity measurements are used to align the INS, and thus determine the initial covariance matrix, as discussed in Section 5.1.5. During this taxi period, the INS is operating, but no measurements are available for updating.

The aircraft's airspeed and rate of climb are assumed to be constant until the cruise altitude is reached. For the remainder of the flight, a constant cruise Mach number and cruise altitude are maintained. The route of flight is defined by a series of waypoints, each specified by latitude and longitude coordinates. The departure airport is assumed as the first waypoint. The predicted windspeed and direction are also input at each waypoint.

The data presented in Table 12 are used in Subroutine FLTPLN to calculate several quantities related to the nominal position and velocity of the aircraft. The time at the beginning of the cruise phase is:

$$t_{cr} = (h_{cr} - h_0)/\dot{h}_{c\ell} + t_1 \tag{115}$$

where the takeoff time t_1 is the sum or the alignment and taxi times:

$$t_1 = \Delta t_a + \Delta t_t \tag{116}$$

The airspeed during the cruise phase is calculated from

$$V_{cr} = M_{cr} a(h_{cr}) \tag{117}$$

where $a(h_{cr})$ is the local speed of sound at the cruise altitude.

The airspeed, altitude and altitude rate can then be calculated as functions of elapsed time:

$$V_a = \begin{cases} V_{c\ell} \quad , & t < t_{cr} \\ V_{cr} \quad , & t \geq t_{cr} \end{cases} \tag{118}$$

$$h = \begin{cases} h_0 + \dot{h}_{c\ell}(t - t_1) & , \quad t < t_{cr} \\ h_{cr} & , \quad t \geq t_{cr} \end{cases} \tag{119}$$

$$\dot{h} = \begin{cases} \dot{h}_{c\ell} & , \quad t - t_1 < t_{cr} \\ 0 & , \quad t - t_1 \geq t_{cr} \end{cases} \tag{120}$$

In the horizontal plane, the nominal flight path maintains a constant track angle across the earth's surface between waypoints. In Appendix A, this is shown to require the following ground track angle:

$$\chi = \tan^{-1}\left\{\Delta\ell/\ln\left[\frac{\cos L_i(1 + \sin L_{i+1})}{\cos L_{i+1}(1 + \sin L_i)}\right]\right\} \tag{121}$$

where $\Delta\ell = \ell_{i+1} - \ell_i$. A constant, average wind is also used between waypoints:

$$V_w = (V_{w_i} + V_{w_{i-1}})/2 \tag{122}$$

$$\theta_w = (\theta_{w_i} + \theta_{w_{i-1}})/2 \tag{123}$$

The aircraft heading required to maintain the track angle χ is

$$\psi = \chi - \delta \tag{124}$$

where the wind correction angle δ is

$$\delta = \sin^{-1}[(V_w/V_a) \sin (\theta_w - \chi)] \qquad (125$$

The groundspeed of the aircraft is then

$$V_g = V_a \cos \delta - V_w \cos (\theta_w - \chi) \tag{126}$$

and the northerly and easterly components are

$$V_N = V_g \cos \chi \tag{127}$$

$$V_E = V_g \sin \chi \tag{128}$$

The elapsed time to fly from waypoint i to waypoint i + 1 is

$$\Delta t_i = r(L_{i+1} - L_i)/V_N \tag{129}$$

or, for a constant latitude ($V_N = 0$, $L_{i+1} = L_i$),

$$\Delta t_i = r \cos L_i \, \Delta \ell / V_E \tag{130}$$

The nominal time-of-arrival at each waypoint is calculated using Equation (129) or (130) as:

$$t_{i+1} = t_i + \Delta t_i \quad , \qquad i = 1, \ldots n-i \tag{131}$$

The latitude and longitude (terrestrial) rates are given by

$$\dot{L} = V_N/r \tag{132}$$

$$\dot{\ell} = V_E/r \cos L \tag{133}$$

and the celestial longitude rate is

$$\dot{\lambda} = \dot{\ell} + \omega_{ie} \tag{134}$$

where ω_{ie} is the earth's rotation rate. Equations (132) to (134) are integrated analytically to obtain $L(t)$, $\ell(t)$ and $\lambda(t)$ (see Appendix A):

$$L(t) = \dot{L}_i + L(t - t_i) \tag{135}$$

$$\ell(t) = \ell_i + (V_E/V_N) \ln \left\{ \frac{\cos L_i \, [1 + \sin L(t)]}{\cos L(t) \, [1 + \sin L_i]} \right\} \tag{136}$$

$$\lambda(t) = \ell(t) + \omega_{ie} t \tag{137}$$

where j is determined such that $t_j \leq t < t_{j+1}$.

Finally, the nominal magnitudes of the geocentric radius vector and the gravitational acceleration are corrected for latitude and altitude (Ref. 31):

$$r = r_e(1 - f \sin^2 L) + h \tag{138}$$

$$g = g_e(1 + c \sin^2 L)(1 - 10^{-7} h) \tag{139}$$

where r_e and g_e are the sea level values at the equator.

6.3 ERROR PROPAGATION

A major element of the simulation program is the propagation of the error covariance matrix P, in accordance with Equation (3). The user-specified statistics of the system errors define the initial value of P, and numerical integration of Equation (3) produces the desired error time histories.

The covariance matrix for the maximum system (i.e., three-dimensional INS with Doppler, Omega and satellite measurements), contains $34 \times 34 = 1156$ elements. However, since P is symmetric ($P = P^T$), the total number of independent terms is $(34)(35)/2 = 595$. Thus the propagation of the covariance matrix requires the integration of 595 equations. Since 10 of the errors are biases or scale factors (whose variances are constant), the maximum total number of equations to be integrated is 585.

In general, the aided-INS configuration selected by the user will not require all 34 error states. For each state not used in the simulation, the appropriate row and column of the covariance matrix can be discarded, reducing the number of equations to be integrated. At the beginning of a simulation run, Subroutines CONFIG and EQNS select those elements of the covariance matrix which are required for the specified navigation system configuration. These active elements are used to define a separate array (S), which is then integrated. The 28 equations describing the 7-state INS errors (first 7 elements of $\underline{x}$) are the only ones out of the 585 total that are always retained in the S array. At the completion of an integration cycle, the new values of S are used to set the corresponding elements of P.

A fourth-order Runge-Kutta integration routine (e.g., Ref. 38) has been selected for the simulation. Comparisons were made between fourth- and third-order Runge-Kutta routines and a midpoint-trapezoidal technique, using various integration step sizes. The first method was found to provide a suitable compromise between accuracy and running time by allowing the use of a larger step size. Adjustable step-size techniques were discarded in favor of the simplicity of a constant step size method. The fourth-order Runge-Kutta algorithm is implemented in Subroutine RKUTTA.

The derivatives of the covariance elements; i.e., the right-hand side of Equation (3), are calculated by Subroutine DIFEQ. Since P is symmetric, Equation (3) may be rewritten as

$$\dot{P} = FP + (FP)^T + GQG^T \tag{140}$$

To have the program perform the matrix multiplication FP at each integration step would obviously be wasteful of computer time, since less than 1/3 of the elements of F are non-zero. Hence, following Reference 26, this multiplication was done beforehand and the resulting equations are written out in the function T(I,J). Similarly, function GQG(I,J) computes the driving noise term GQG^T in Equation (140).

6.4 COVARIANCE UPDATES

If any of the available aiding systems is being used, the simulation checks for the occurrence of an update at the completion of each integration cycle. If it is time for one or more measurements, the covariance matrix is updated as described in Section 4.2. Using the recursive formulation of the filter equations, each "measurement" (alignment, Doppler, Omega or satellite-ranging) actually provides two sequential updates. The result of these two scalar updates is identical to that of a single two-dimensional measurement, but the mathematical implementation of the recursive filter is much simpler.

The appropriate subroutine (ALIGN, DOPLR, OMEG or SATR) computes the measurement vector $\underline{h}$ for the first update using Equation (60), (78), (88) or (101), then determines the optimum filter gain for the update using Equation (10). Subroutine UPDATE performs the update itself via either Equation (13) or (14), depending upon whether optimum or suboptimum gains are being used. Next, the measurement vector for the second update is determined from Equation (61), (79), (88) or (101), and the remainder of the process is repeated.

To illustrate the effect of the measurement, the system position and velocity errors are output before and after the update process. The updated covariance matrix becomes in effect a new initial condition for Equation (3), and the propagation process is resumed until another measurement is taken.

6.5 SIMULATION OUTPUTS

The principal outputs of the program are the time histories of the standard deviations of the position and velocity errors, resolved into along-track, cross-track and vertical components. However, the covariance matrix provides the error statistics in terms of the navigation coordinate frame (latitude, longitude, vertical). The vertical errors are the same in both frames and do not require any transformation. The resolution of the horizontal errors from the navigation frame into the desired track referenced frame is accomplished as follows. From Figure 24, the position

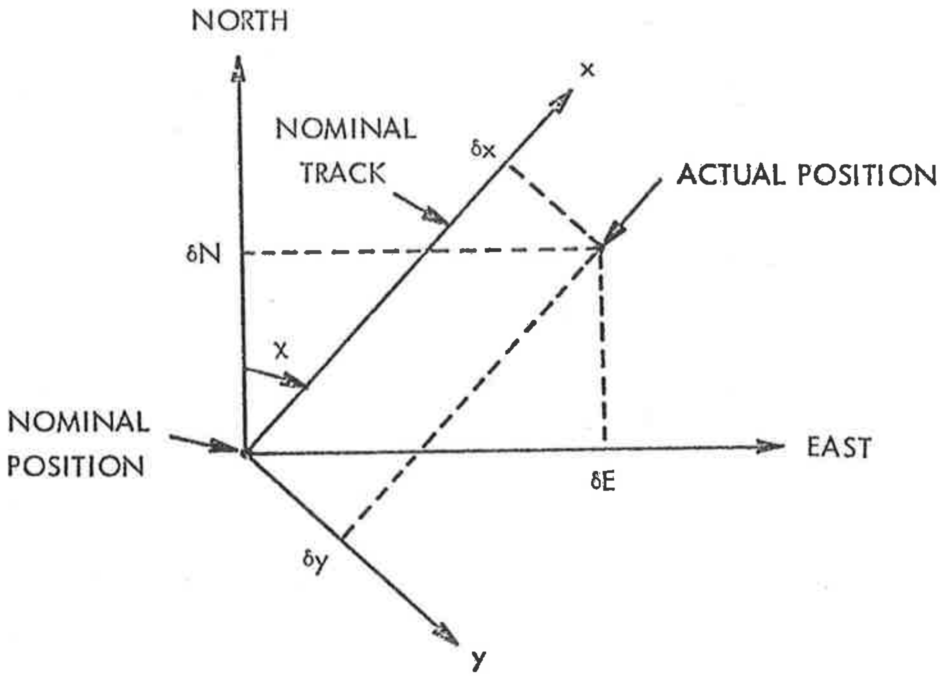

Figure 24. Navigation and Track-Referenced Coordinates.

errors in the north-east navigation frame are

$$\delta N = r\ \delta L \tag{141}$$

$$\delta E = r \cos L\ \delta \ell \tag{142}$$

In the track-referenced frame the errors are

$$\delta x = r(\delta L \cos \chi + \delta \ell \cos L \sin \chi) \tag{143}$$

$$\delta y = r(-\ \delta L \sin \chi + \delta \ell \cos L \cos \chi) \tag{144}$$

The standard deviations of these errors are then

$$\sigma_{\delta x} = \sqrt{\langle \delta x^2 \rangle}$$

$$= r\sqrt{\sigma^2_{\delta L} \cos^2 \chi + \sigma^2_{\delta \ell} \cos^2 L \sin^2 \chi + 2\langle \delta L\ \delta \ell \rangle \cos L \sin \chi \cos \chi} \tag{145}$$

$$\sigma_{\delta y} = \sqrt{\langle \delta y^2 \rangle}$$

$$= r\sqrt{\sigma^2_{\delta L} \sin^2 \chi + \sigma^2_{\delta \ell} \cos^2 L \cos^2 \chi - 2\langle \delta L\ \delta \ell \rangle \cos L \sin \chi \cos \chi} \tag{146}$$

Note that the cross-correlation between the latitude and longitude errors $\langle \delta L\ \delta \ell \rangle$ are needed for these outputs. Similarly, the velocity error σ's in the track-referenced frame are:

$$\sigma_{\delta \dot{x}} = r\sqrt{\sigma^2_{\delta \dot{L}} \cos^2 \chi + \sigma^2_{\delta \dot{\ell}} \cos^2 L \sin^2 \chi + 2\langle \delta \dot{L}\ \delta \dot{\ell} \rangle \cos L \sin \chi \cos \chi} \tag{147}$$

$$\sigma_{\delta \dot{y}} = r\sqrt{\sigma^2_{\delta \dot{L}} \sin^2 \chi + \sigma^2_{\delta \dot{\ell}} \cos^2 L \cos^2 \chi - 2\langle \delta \dot{L}\ \delta \dot{\ell} \rangle \cos L \sin \chi \cos \chi} \tag{148}$$

Again, the cross-correlation term $\langle \delta \dot{L}\ \delta \dot{\ell} \rangle$ is required.

The transformations expressed by Equations (145) to (148) merely indicate a rotation of the coordinate system in which the position and velocity error ellipses are being observed. Because the track angle X changes during the flight, the error reference is not invariant. Consequently, when a change in course occurs at a waypoint, the output errors will show discontinuities as the reference suddenly rotates. The results presented in the following section will illustrate this effect.

SECTION 7

SIMULATION RESULTS

This section presents a number of simulation results which have been obtained using Program NATNAV. The typical error model input parameters presented in Section 5 were used unless otherwise specified. The same nominal flight plan described below was utilized for all the examples.

7.1 NOMINAL FLIGHT PLAN

The nominal flight plan was developed for a typical west-to-east North Atlantic flight. This flight was rather arbitrarily defined as originating from Boston's Logan International Airport and terminating at the Shannon, Ireland VOR, which is a convenient coast-in point for London's Heathrow Airport. As shown in Figure 25, the route of flight was selected to approximate the great-circle path from Boston to London. The departure route follows the high-level airway HL 575 to Yarmouth, Nova Scotia, thence HL 579 to the Stephenville, Newfoundland, coast-out point. Beyond Stephenville, the over-water waypoints are selected at integer latitudes each 10° of longitude, which is the normal operational procedure.

Table 13 summarizes the nominal flight plan data. The aircraft parameters are representative of 707 or DC-8 commercial aircraft. The wind data was arbitrarily selected to represent the westerly characteristics of NAT winds aloft.

7.2 INS WITH NO UPDATES

Figures 26 and 27 present the position and velocity error histories for the unipolar INS with no updates after alignment. For the typical error statistics pre-

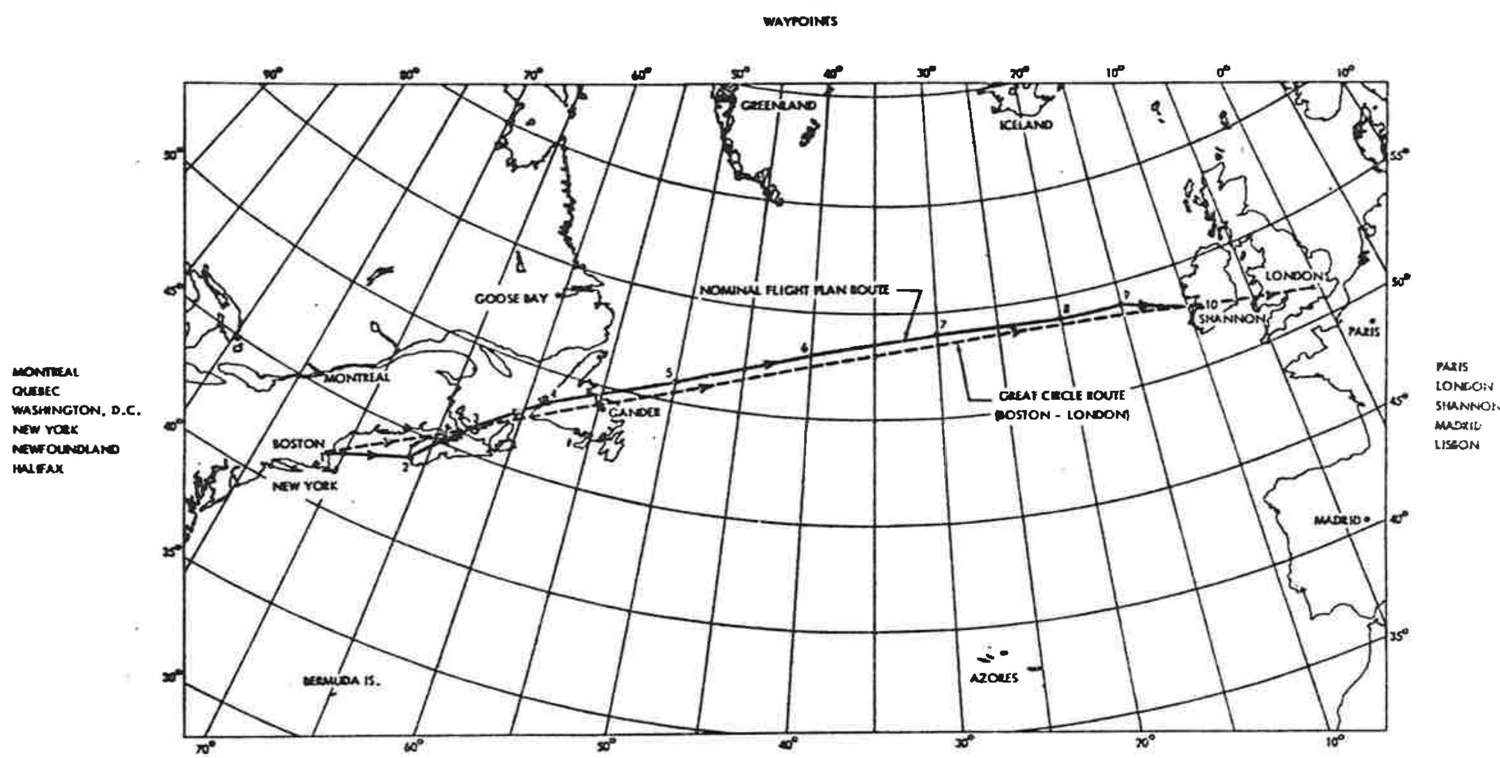

Figure 25. Nominal Boston-to-Shannon Route.

Table 13. Nominal Flight Plan Data (Boston to Shannon).

Route of Flight (NWPTS = 10)				
I = Waypoint	LAT(I) = Latitude (Deg)	LON(I) = Longitude (Deg)	THETAW(I) = Wind Direction (Deg)	VW(I) = Wind Speed (Knots)
1 (Boston, Mass.)	42.36 N	71.01 W	320.0	10.0
2 (Yarmouth, N. S.)	42.83 N	66.08 W	300.0	30.0
3 (Charlottetown, P.E.I.)	46.21 N	62.98 W	270.0	40.0
4 (Stephanville, Newf.)	48.54 N	58.56 W	270.0	40.0
5	51.00 N	50.00 W	270.0	40.0
6	53.00 N	40.00 W	270.0	40.0
7	54.00 N	30.00 W	270.0	40.0
8	54.00 N	20.00 W	270.0	40.0
9	54.00 N	15.00 W	270.0	40.0
10 (Shannon, Ire.)	52.70 N	8.92 W	270.0	40.0

DTA	= INS Alignment Time	=	15.00 minutes
DTT	= Taxi Time	=	5.00 minutes
HØ	= Airport Elevation	=	19.00 feet
VCL	= A/C Climb Speed	=	280.0 knots
RC	= A/C Rate of Climb	=	1,500. feet per minute
MCR	= Cruise Mach Number	=	.82
HCR	= Cruise Altitude	=	35,000. feet

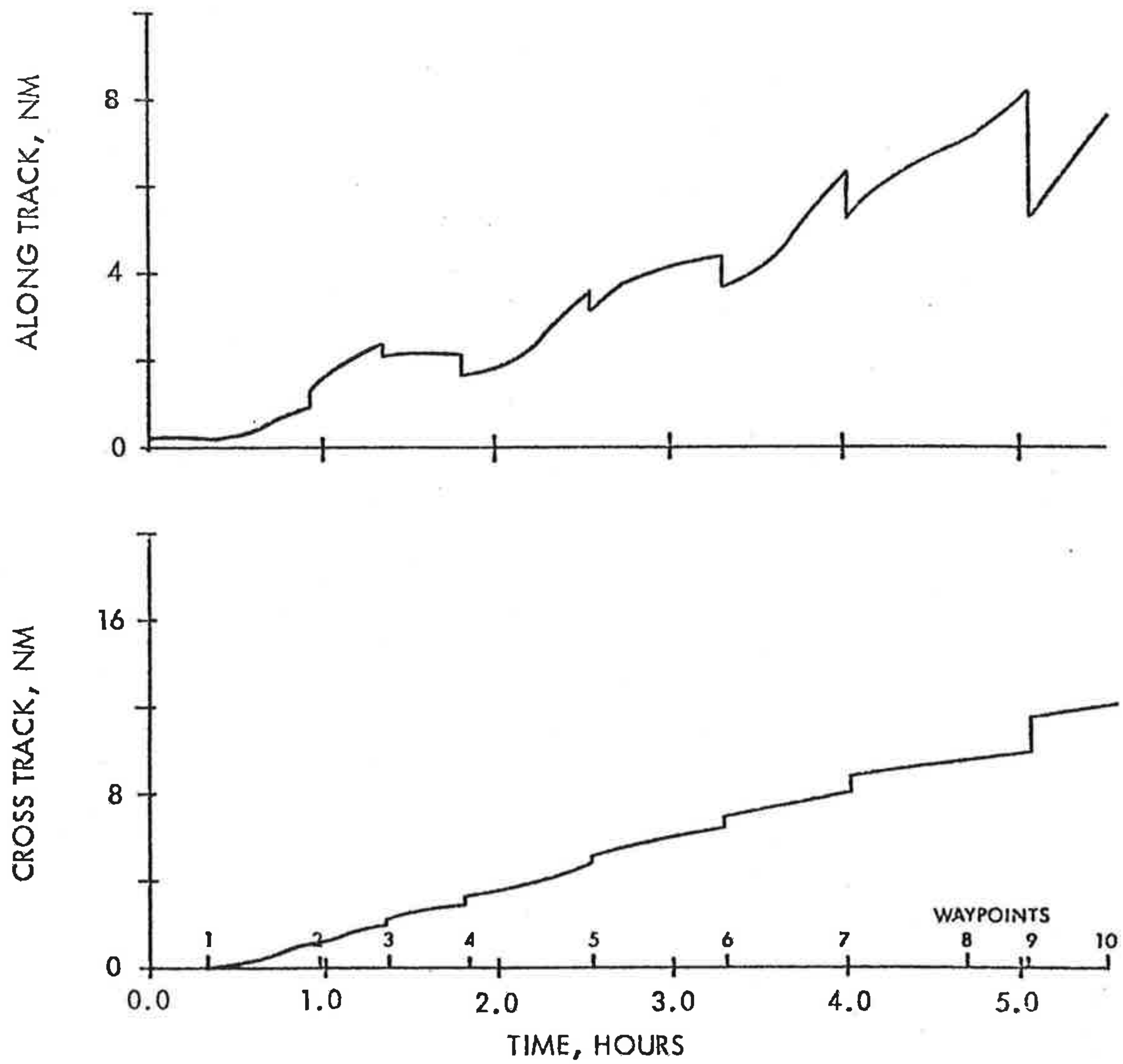

Figure 26. Position Errors for Unipolar INS with no Updates.

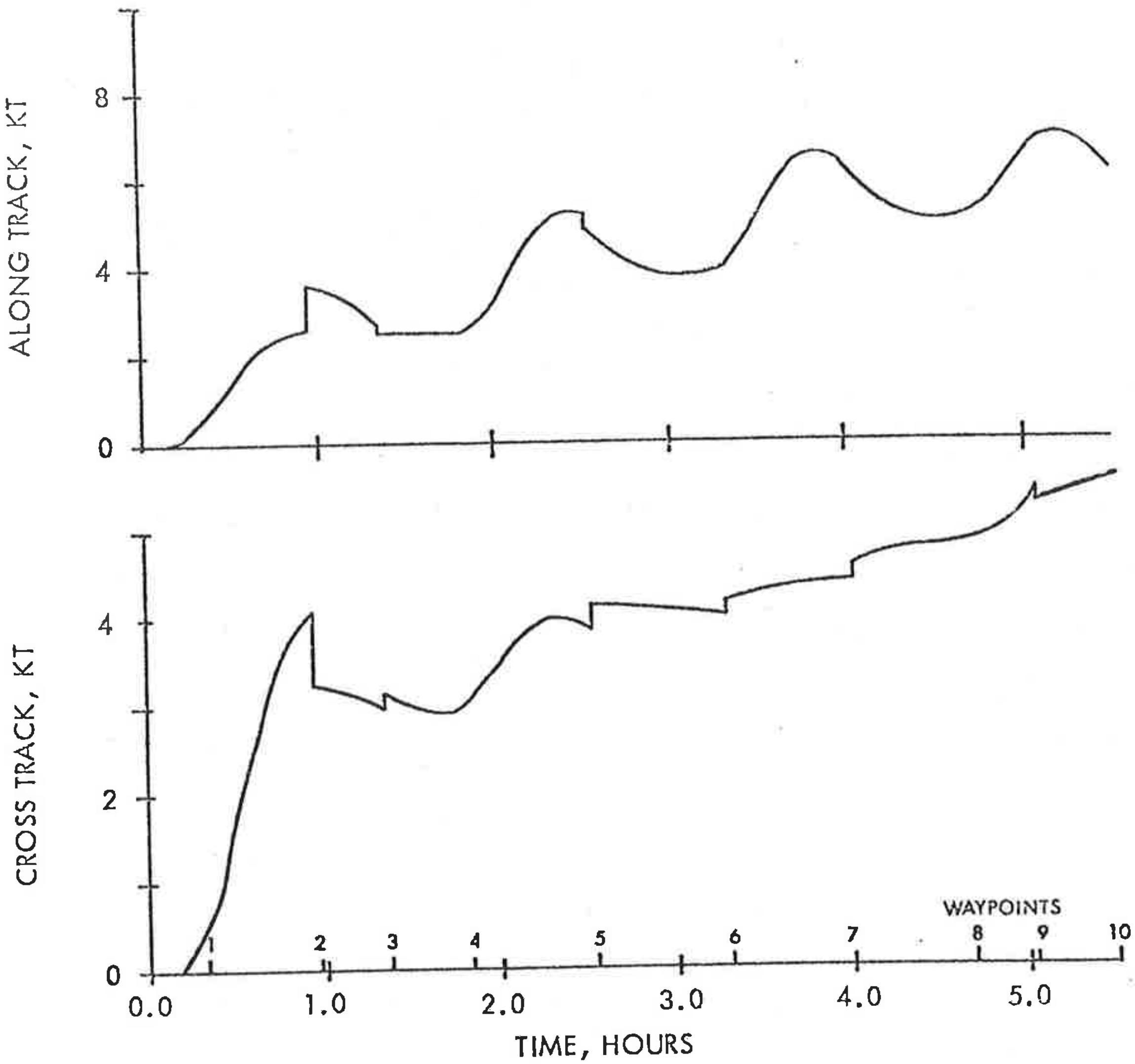

Figure 27. Velocity Errors for Unipolar INS with no Updates.

sented in Section 5, the position errors increase with time to an RMS value of approximately 15 nm at Shannon. As mentioned in Section 6.5, the discontinuities in these errors are the result of the heading changes, and attendant coordinate frame rotations, at the waypoints indicated at the bottom of the figure. The velocity uncertainties in Figure 27 display the typical Schuler 84-minute (1.4 hr) oscillation. The RMS error at Shannon is about 8 knots.

The altitude and vertical speed errors are shown in Figure 28. The dominant altimeter error is the scale factor, which produces a 105 ft uncertainty during cruise. The scale factor error dominates the vertical speed uncertainty during climb, while the random noise prevails in cruise.

To show the effects of the two most significant INS component errors, Figures 29 and 30 present, respectively, the error histories for the same INS, neglecting all but the gyro drift errors and the accelerometer uncertainties. Comparison of Figures 26 and 29 shows that the gyro drift uncertainties are responsible for most of the total position errors. However, from Figure 30, the two component errors have comparable effects on the overall velocity uncertainty, with the accelerometer errors being slightly more important.

7.3 DEAD-RECKONING

Figure 31 depicts the position errors with dead-reckoning for 15 knot uncertainties in both the north and the east winds. The RMS error at Shannon is almost 71 nm.

7.4 INS WITH OMEGA UPDATES

The improvement in the navigational accuracy provided by updating the INS with periodic Omega position fixes is shown in Figures 32 and 33. Three update

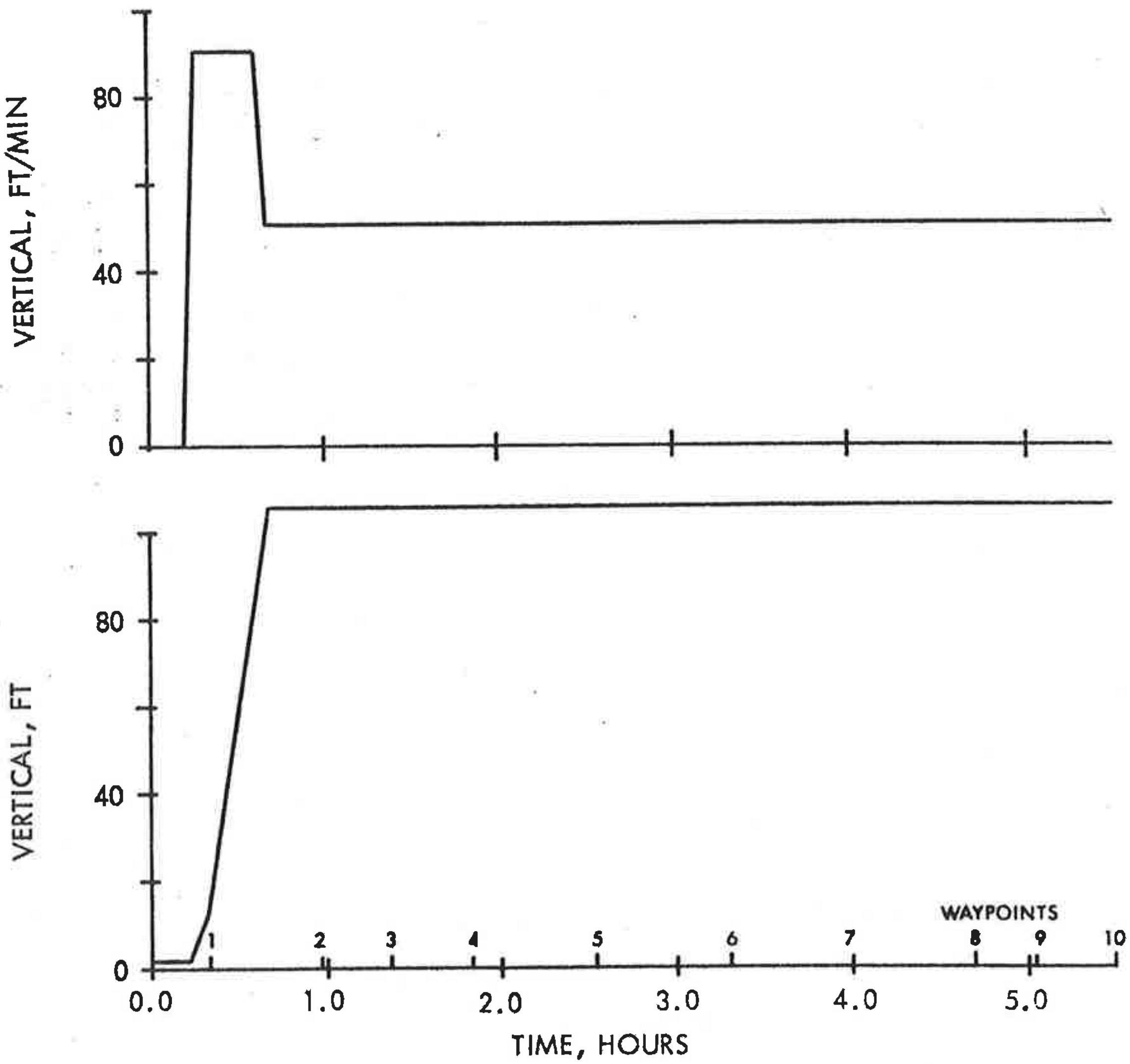

Figure 28. Altitude and Vertical Speed Errors.

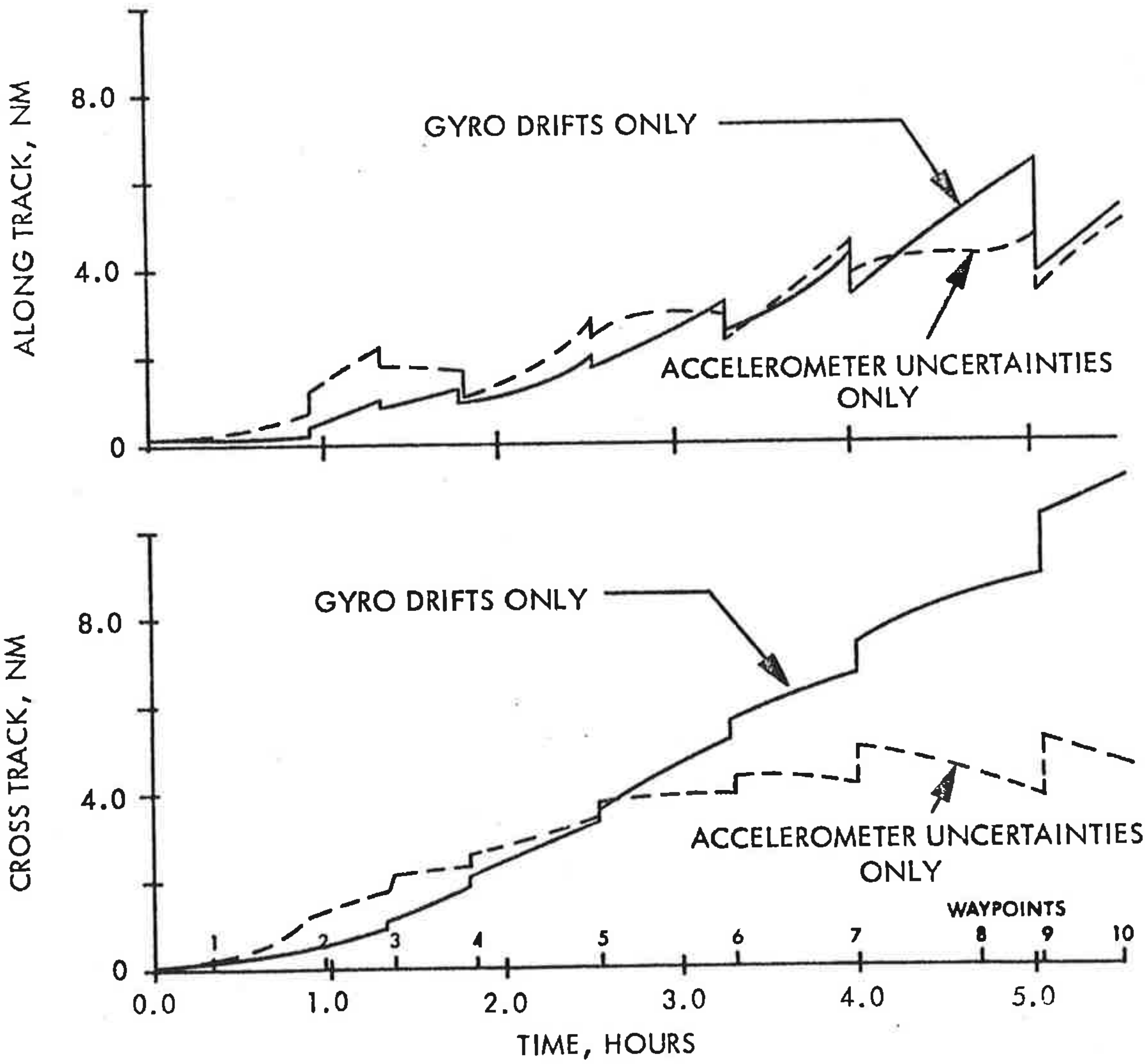

Figure 29. Effects of Gyro Drifts and Accelerometer Uncertainties on INS Position Errors.

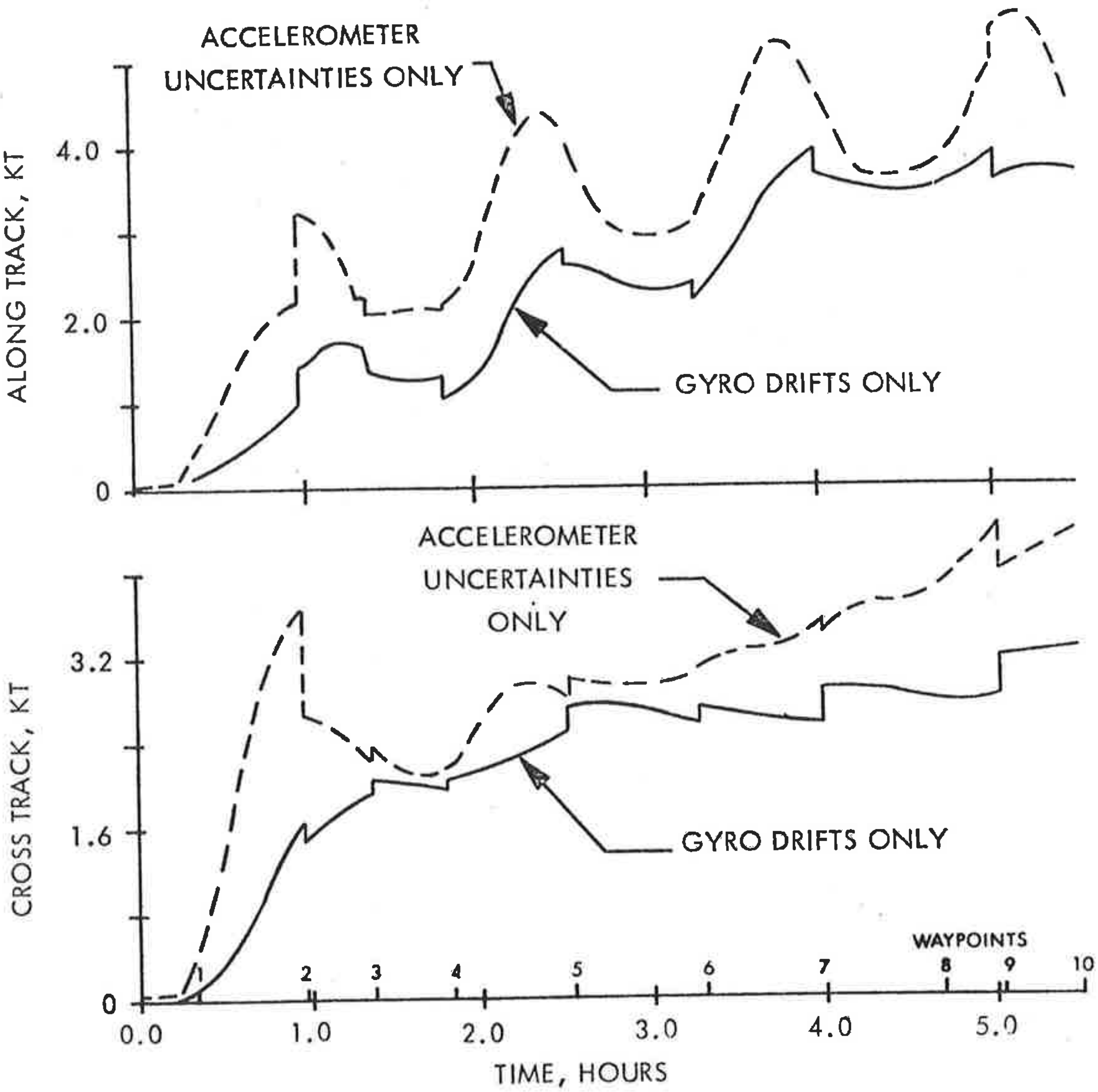

Figure 30. Effects of Gyro Drifts and Accelerometer Uncertainties on INS Velocity Errors.

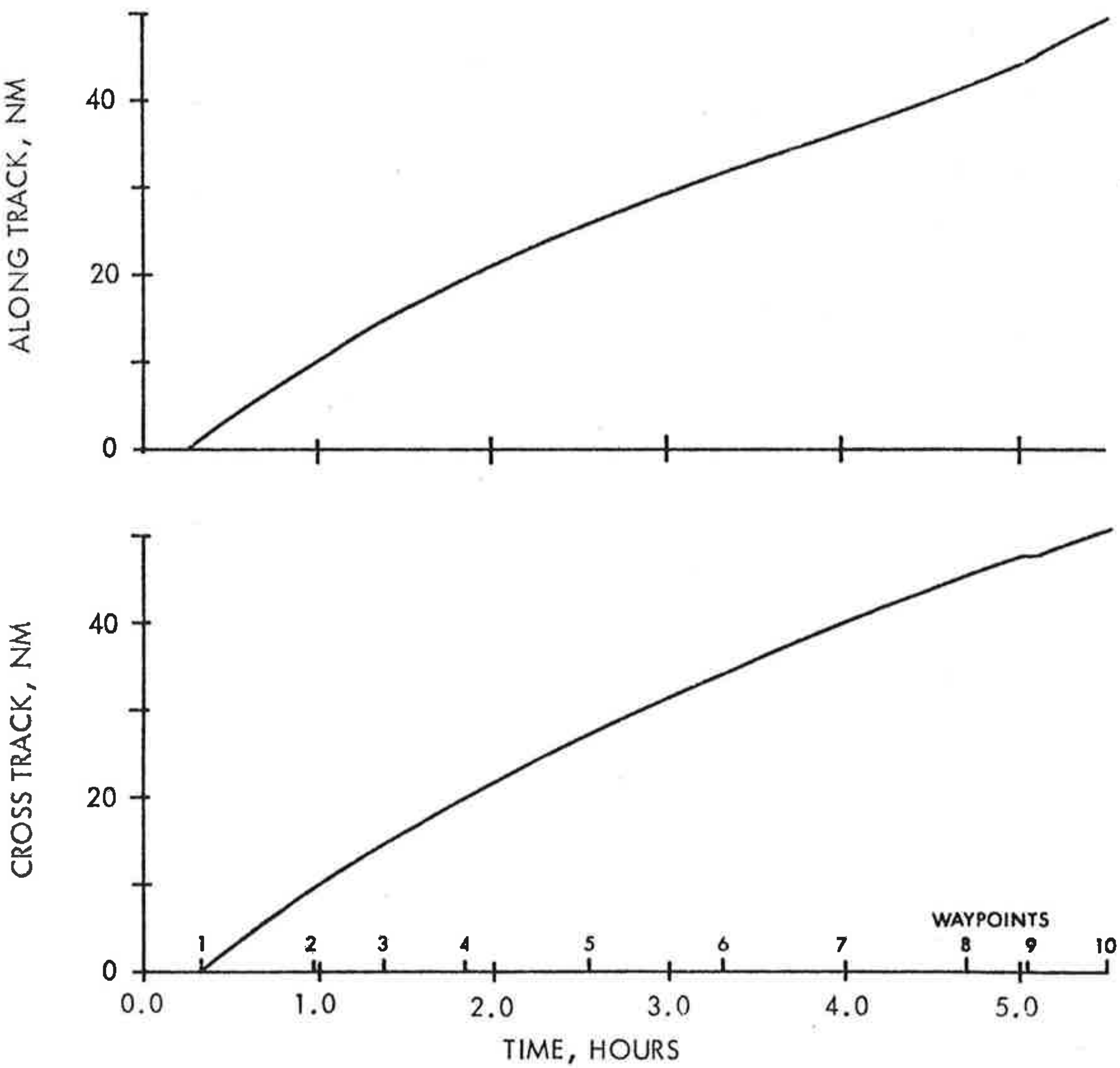

Figure 31. Position Errors with Dead-Reckoning.

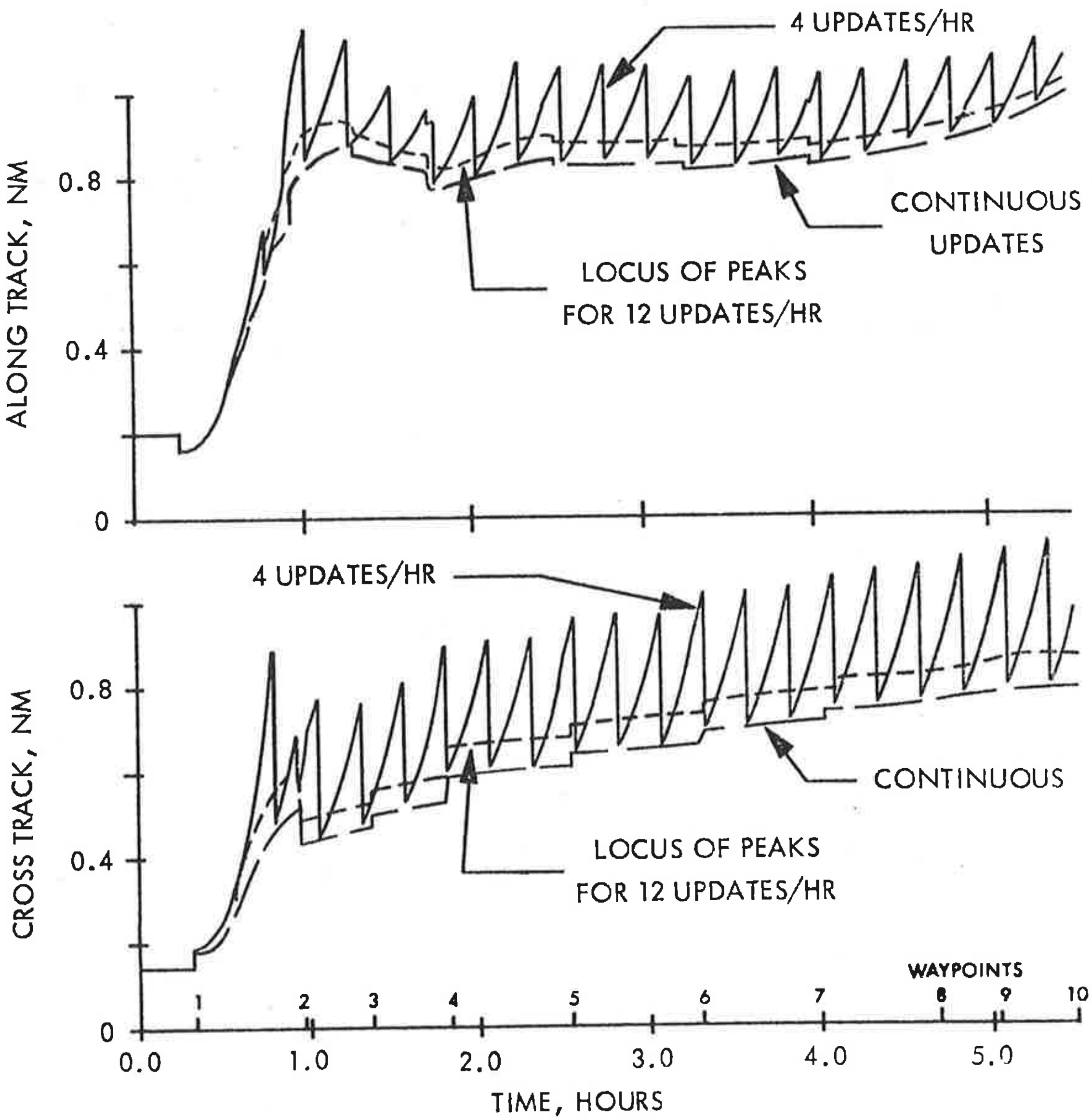

Figure 32. INS Position Errors with Omega Updates at Various Rates.

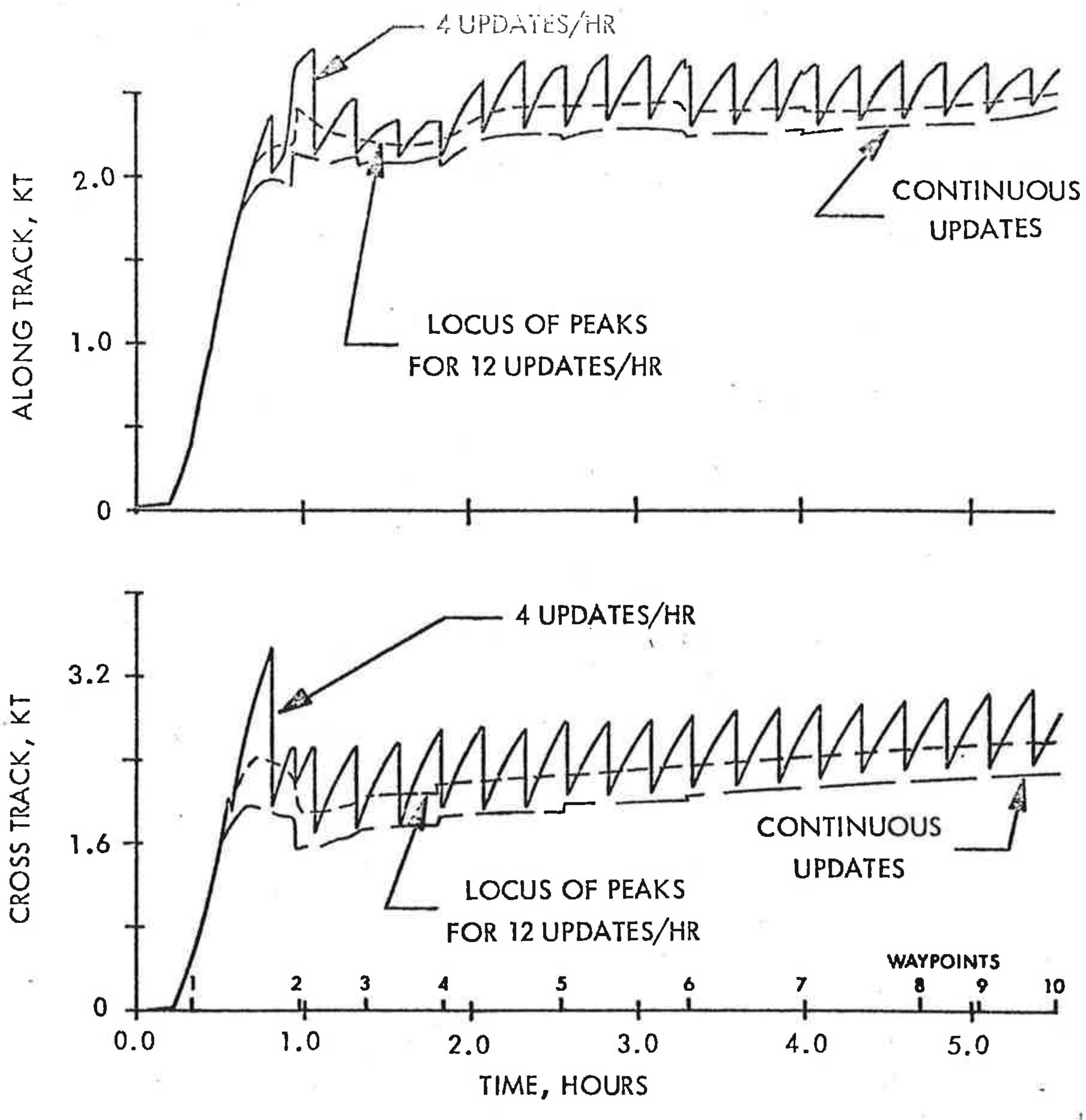

Figure 33. INS Velocity Errors with Omega Updates at Various Rates.

rates are compared: continuous, 12 fixes/hr and four fixes/hr. In each case, the errors immediately after incorporating a measurement are essentially the same as the continuous measurements. The only significant difference between these update rates is the length of time during which the INS is allowed to drift freely. With continuous updates, the RMS position error at Shannon is 1.25 nm. When Omega fixes are taken every 15 minutes, the average reduction in the RMS position error is nearly 0.4 nm; reducing the measurement interval to five minutes provides a five-fold improvement in the average position uncertainty. The velocity uncertainties in Figure 33 display the same behavior.

To illustrate another INS mechanization, a strapdown system was simulated with Omega measurements every 15 minutes. The position uncertainties were almost identical to those shown in Figure 32 for the local-level, unipolar system. The three components of velocity uncertainties are presented in Figure 34. The cross- and along-track errors are very similar to those in Figure 33, but show a slightly larger drift rate, particularly during the first couple of hours of the flight. The major difference is the vertical speed errors in the three-dimensional strapdown system (cf. Figure 28), which settles down to about 16 fpm after the initial climbout transients. Notice that the Omega measurements also reduce the vertical speed error, primarily as a result of improved estimates for the INS reference frame misalignments.

7.5 INS WITH DOPPLER UPDATES

Figures 35 and 36 show the position and velocity errors for the INS with Doppler updates every 10 minutes. As expected, the Doppler measurements have very little direct effect on the position uncertainties. The RMS position error increases essentially linearly, to about 4.5 nm at Shannon. The principal effects of the Doppler measurements are to bound the velocity uncertainty to an average

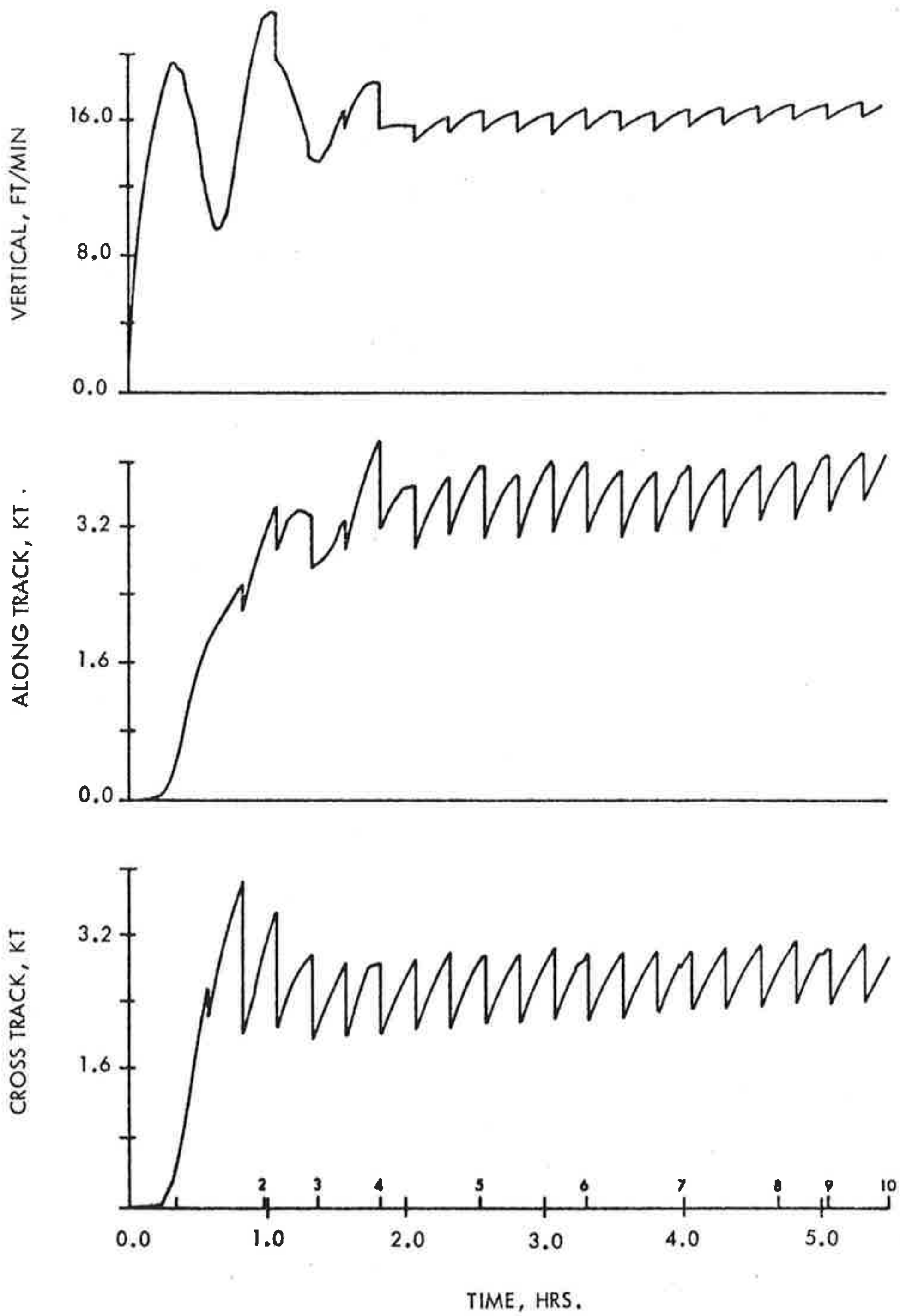

Figure 34. Strapdown INS Velocity Errors with Omega Updates.

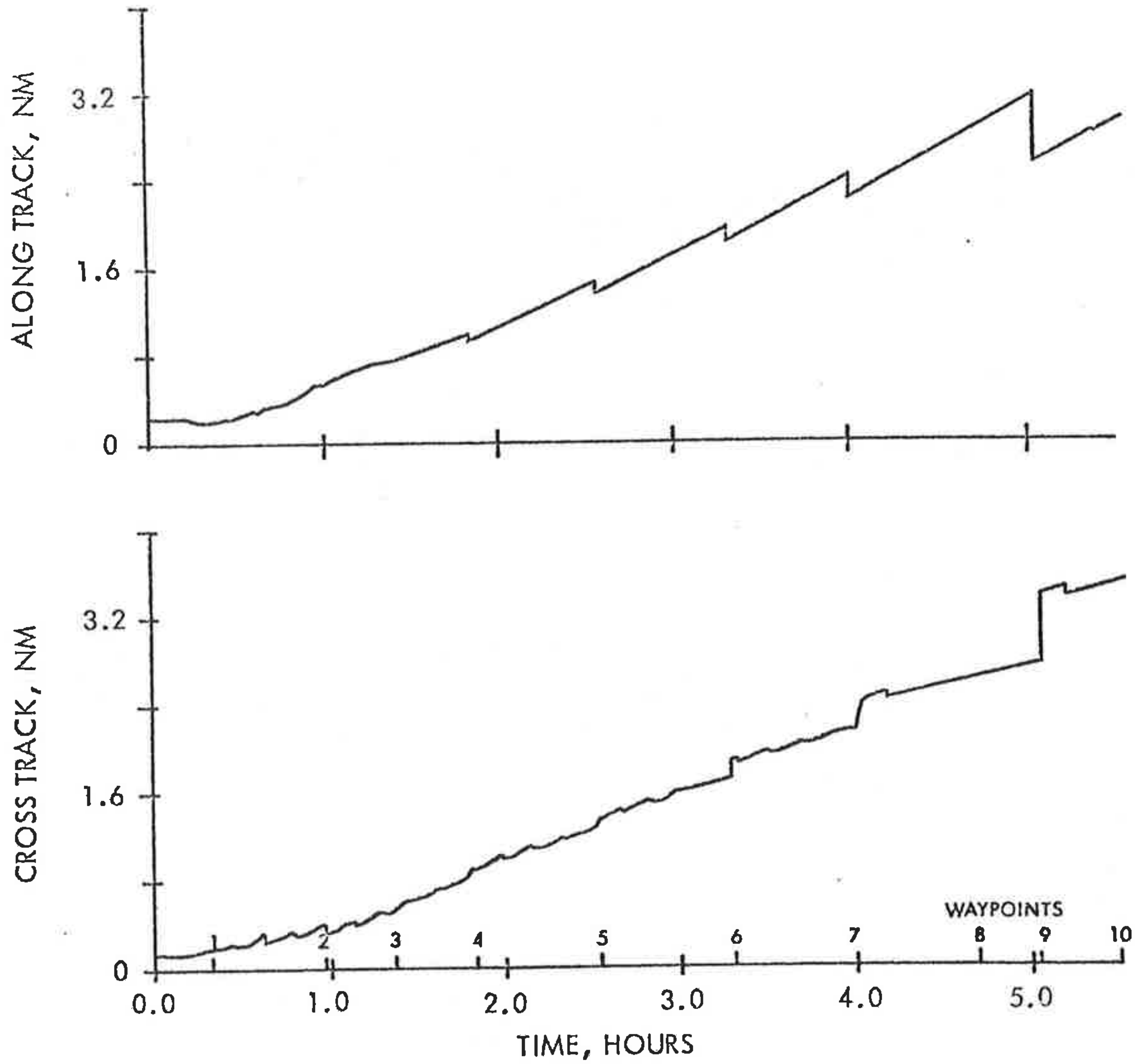

Figure 35. INS Position Errors with Doppler Updates Every 10 Minutes.

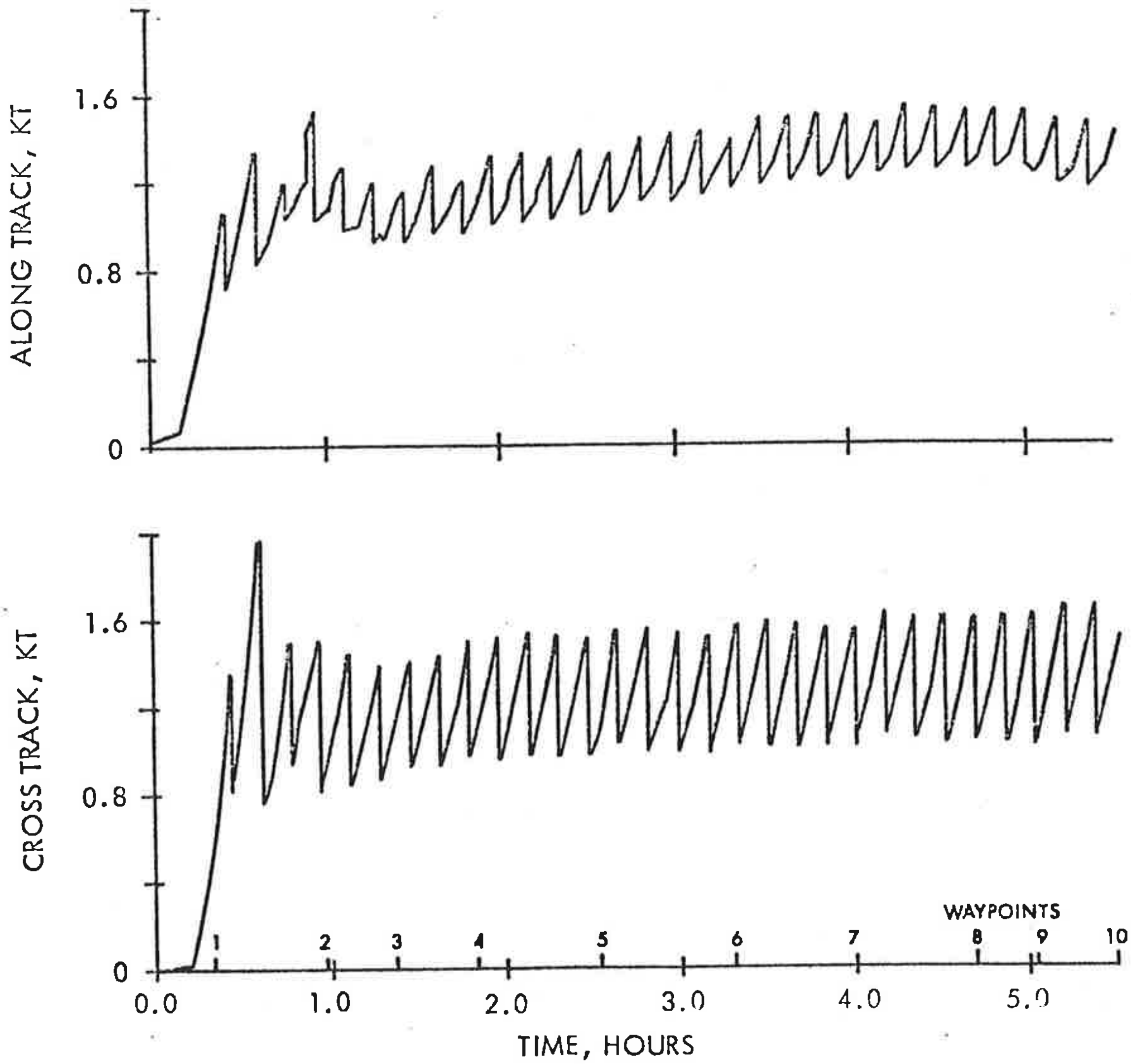

Figure 36. INS Velocity Errors with Doppler Updates Every 10 Minutes.

RMS value of about 1.5 knots, and to reduce the average platform misalignment angles by more than 50% compared to the unaided INS. The result is a better than three-fold improvement in position accuracy.

The effects of using both Doppler and Omega measurements are depicted in Figures 37 and 38. Notice (cf. Figure 32) that the position errors are significantly smaller than those for Omega updates alone, even continuous ones, due to the improved velocity error estimates with the Doppler radar. The RMS position uncertainty at Shannon is 1.06 nm, compared with 4.52 nm with Doppler alone, and 1.44 nm with Omega alone. For the first hour the velocity errors in Figure 38 are nearly identical to those in Figure 36 (Doppler updates only), but they become progressively better as a result of the improved INS misalignment estimates from the Omega updates.

7.6 INS WITH SATELLITE-RANGING UPDATES

Figures 39 and 40 illustrate the position and velocity errors for the INS with satellite-ranging updates at 20-minute intervals. Even with this update interval, the average RMS position uncertainty during the flight is only about 0.4 nm. At Shannon, the RMS position error is less than 0.3 nm. It is obvious that both the position and velocity errors in Figures 39 and 40 could be substantially reduced by more frequent updates, if necessary.

7.7 INS WITH SUBOPTIMUM OMEGA GAINS

Figure 41 presents the optimum filter gains for Omega measurements at 15-minute intervals. For each line of position there are 22 non-zero elements in the filter gain vector $\underline{K}$. After initial transients of a couple of hours' duration, most of these gains stabilize at fairly constant values or slopes.

To examine a much simpler mechanization of the hybrid navigator, a set

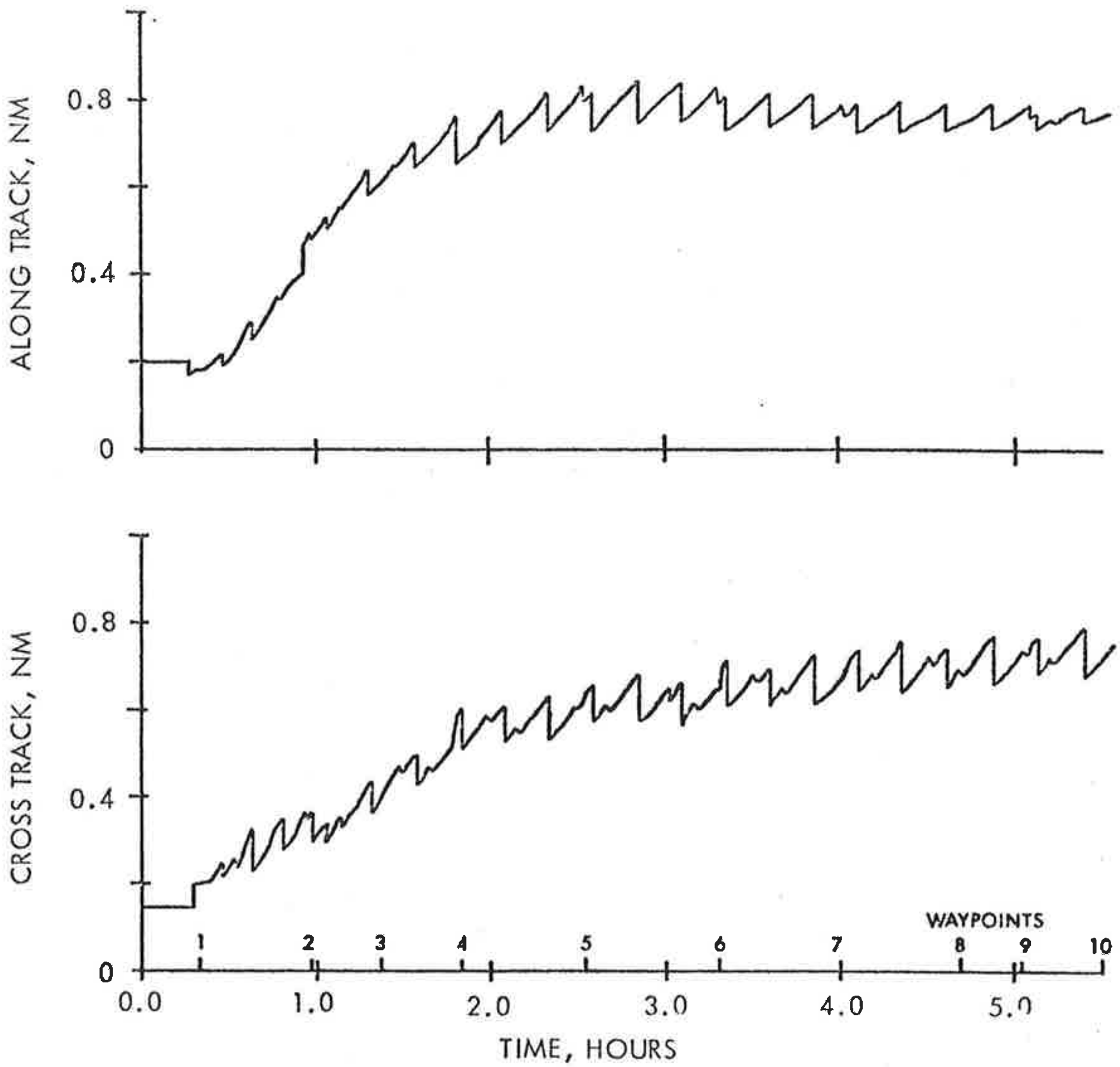

Figure 37. INS Position Errors with both Omega and Doppler Updates.

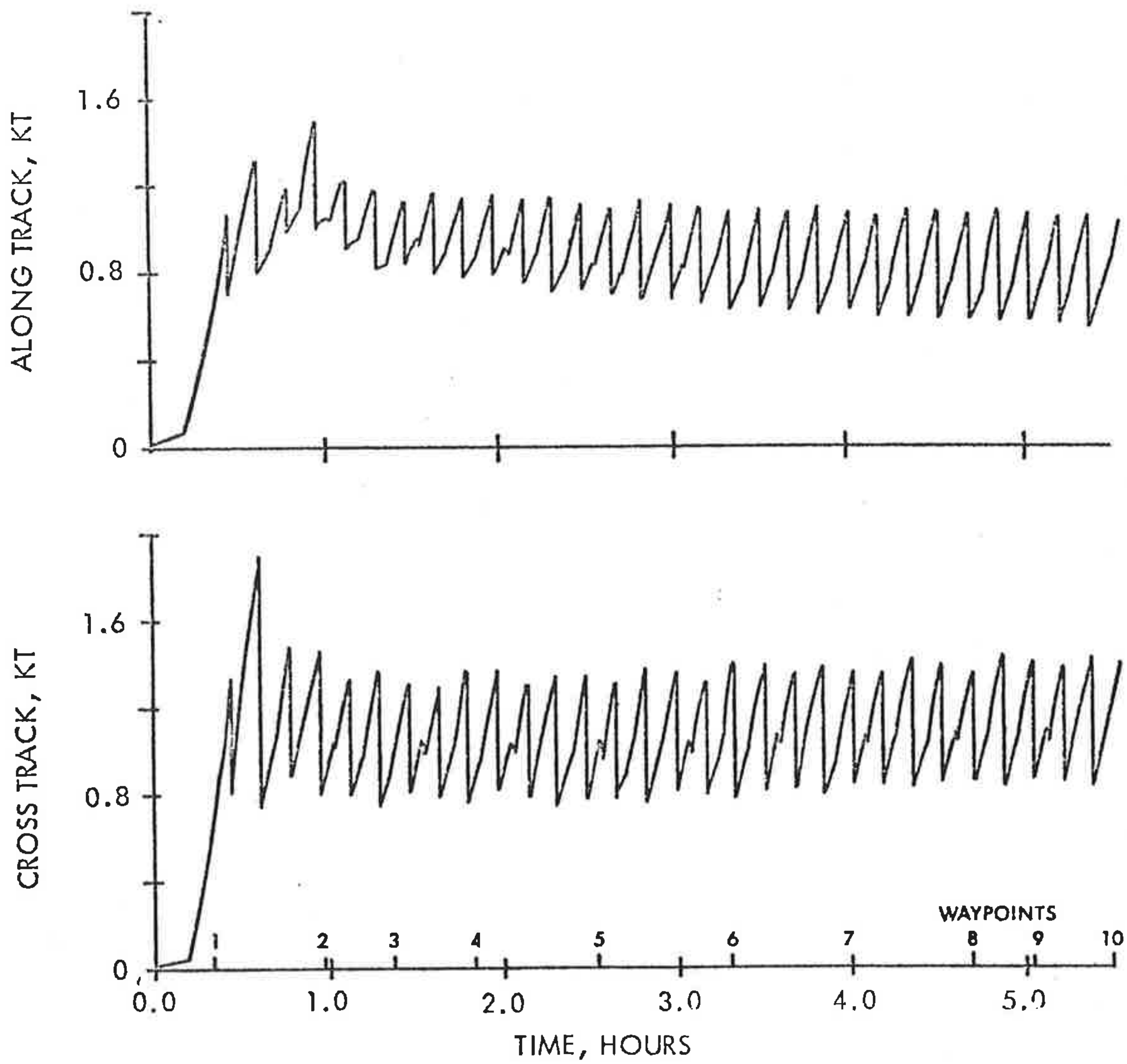

Figure 38. INS Velocity Errors with both Omega and Doppler Updates.

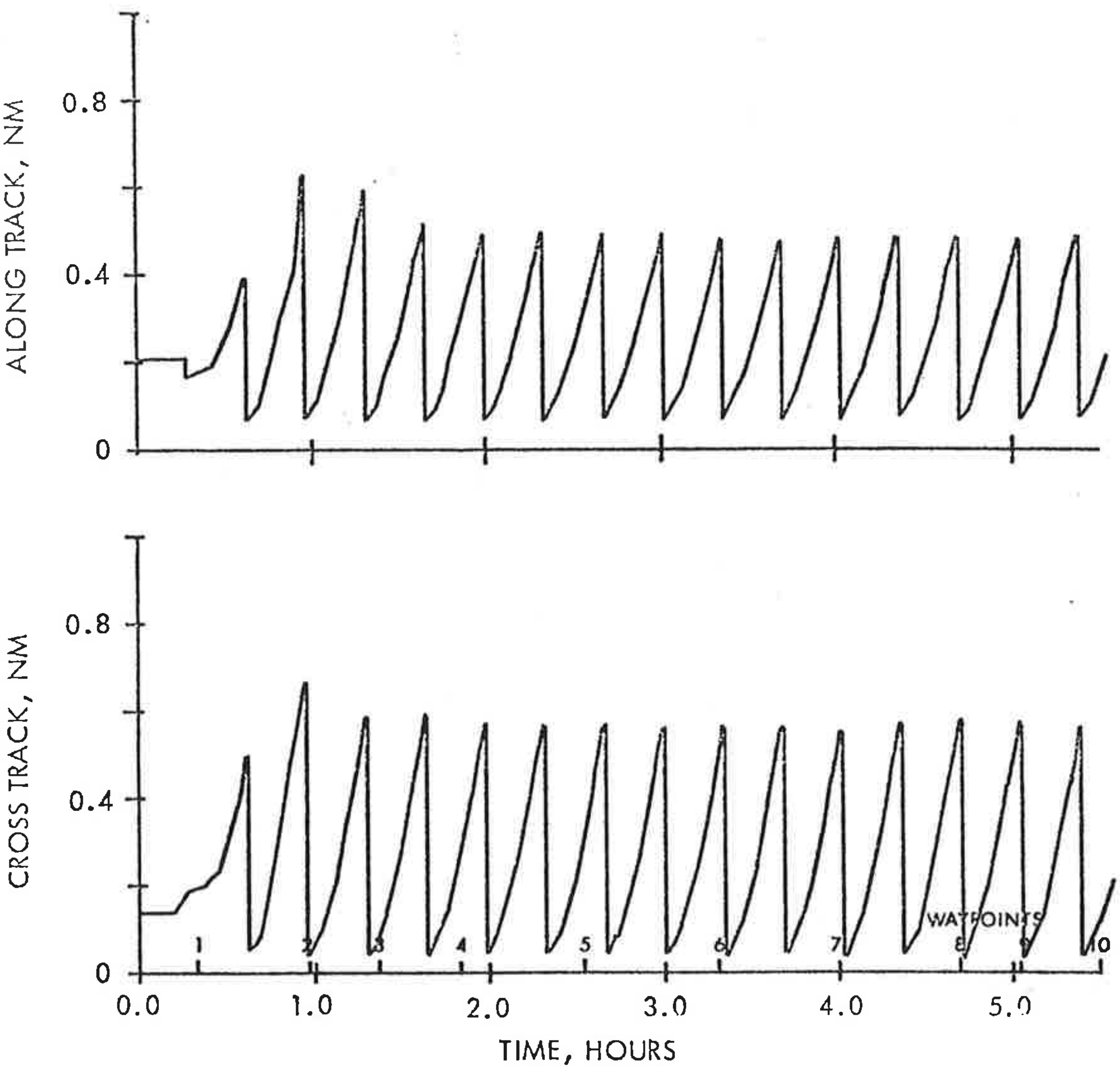

Figure 39. INS Position Errors with Satellite-Ranging Updates Every 20 Minutes.

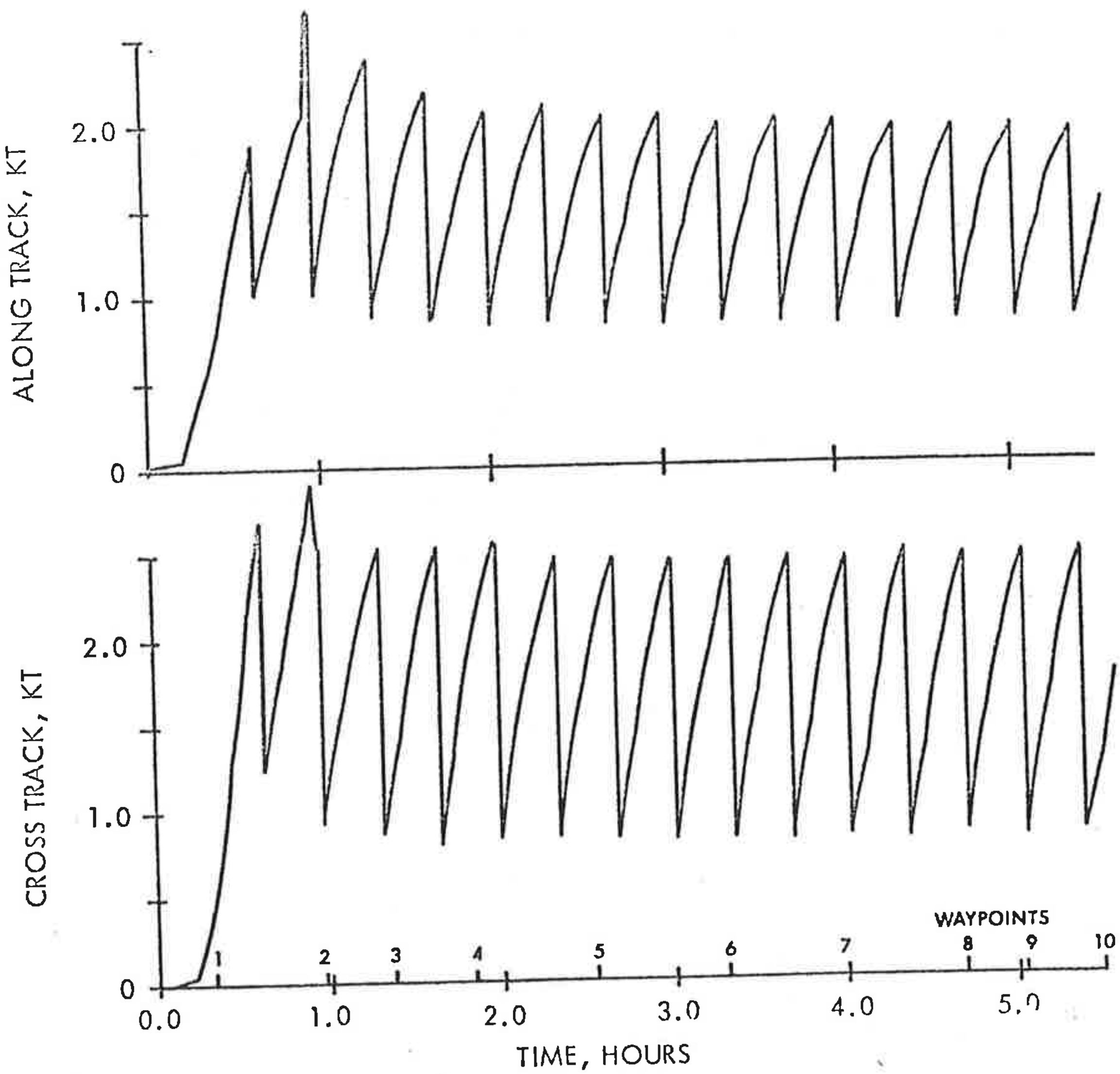

Figure 40. INS Velocity Errors with Satellite-Ranging Updates Every 20 Minutes.

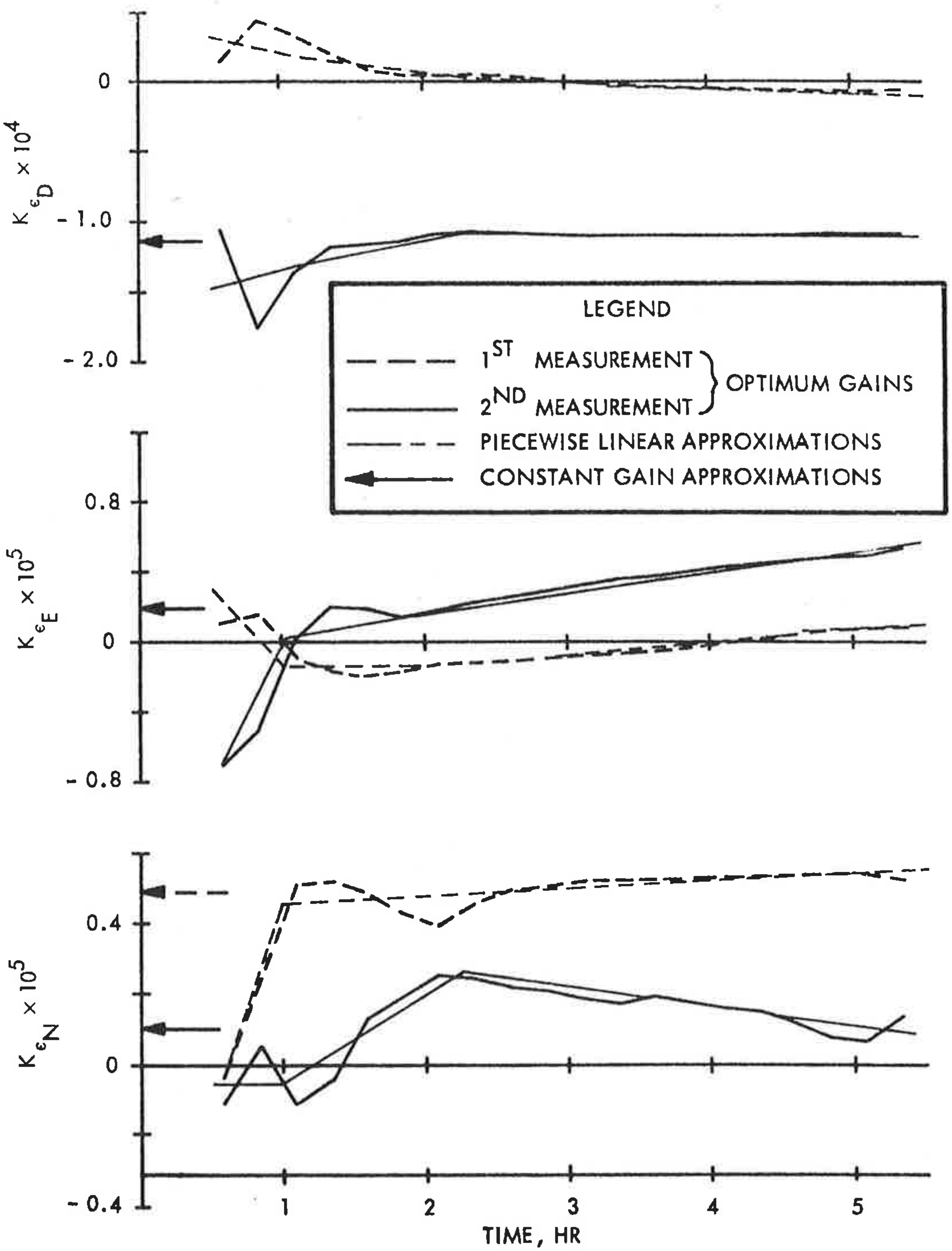

Figure 41. Optimum Filter Gains for INS with Omega Updates Every 15 Minutes.

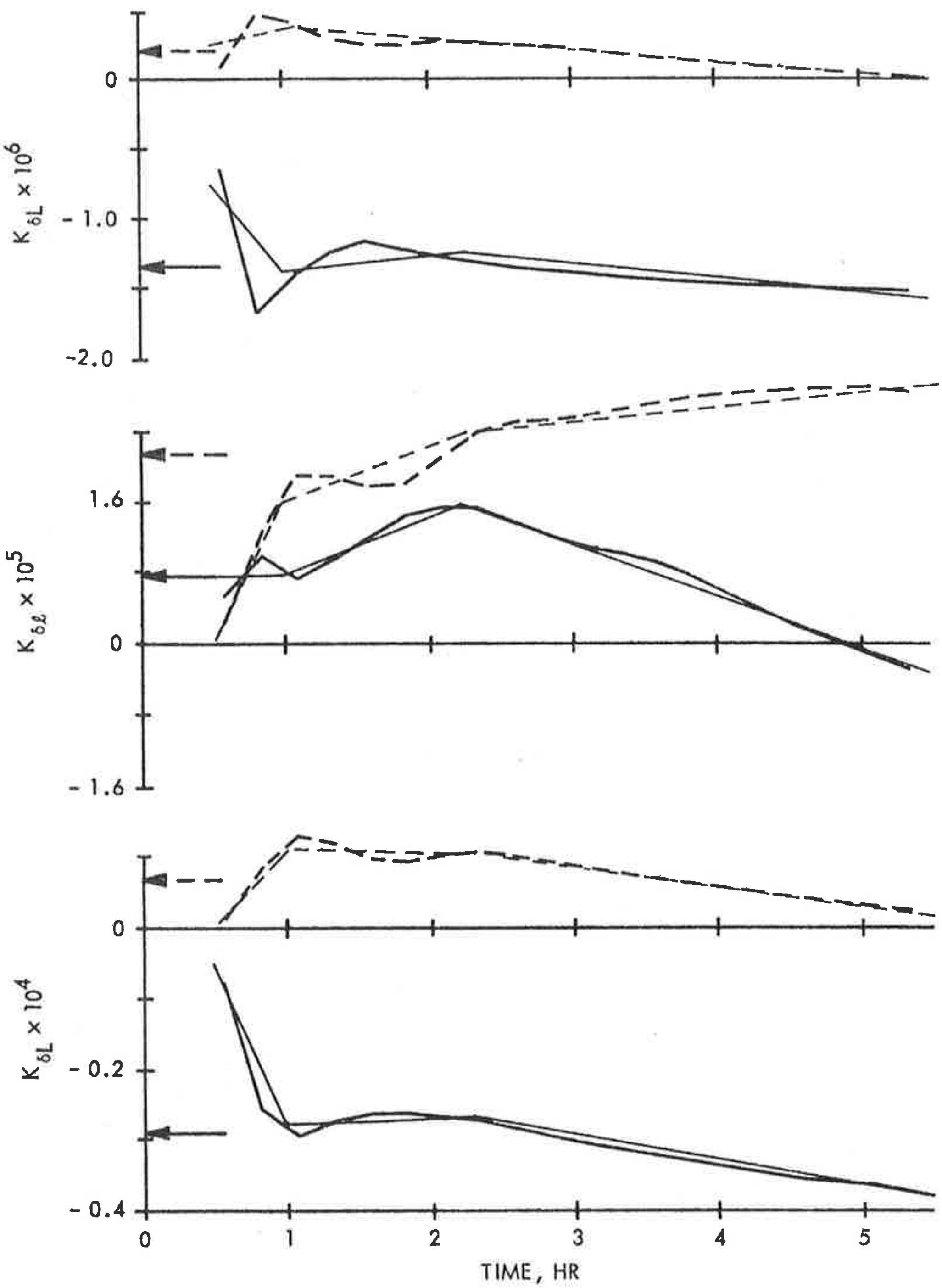

Figure 41. (Continued).

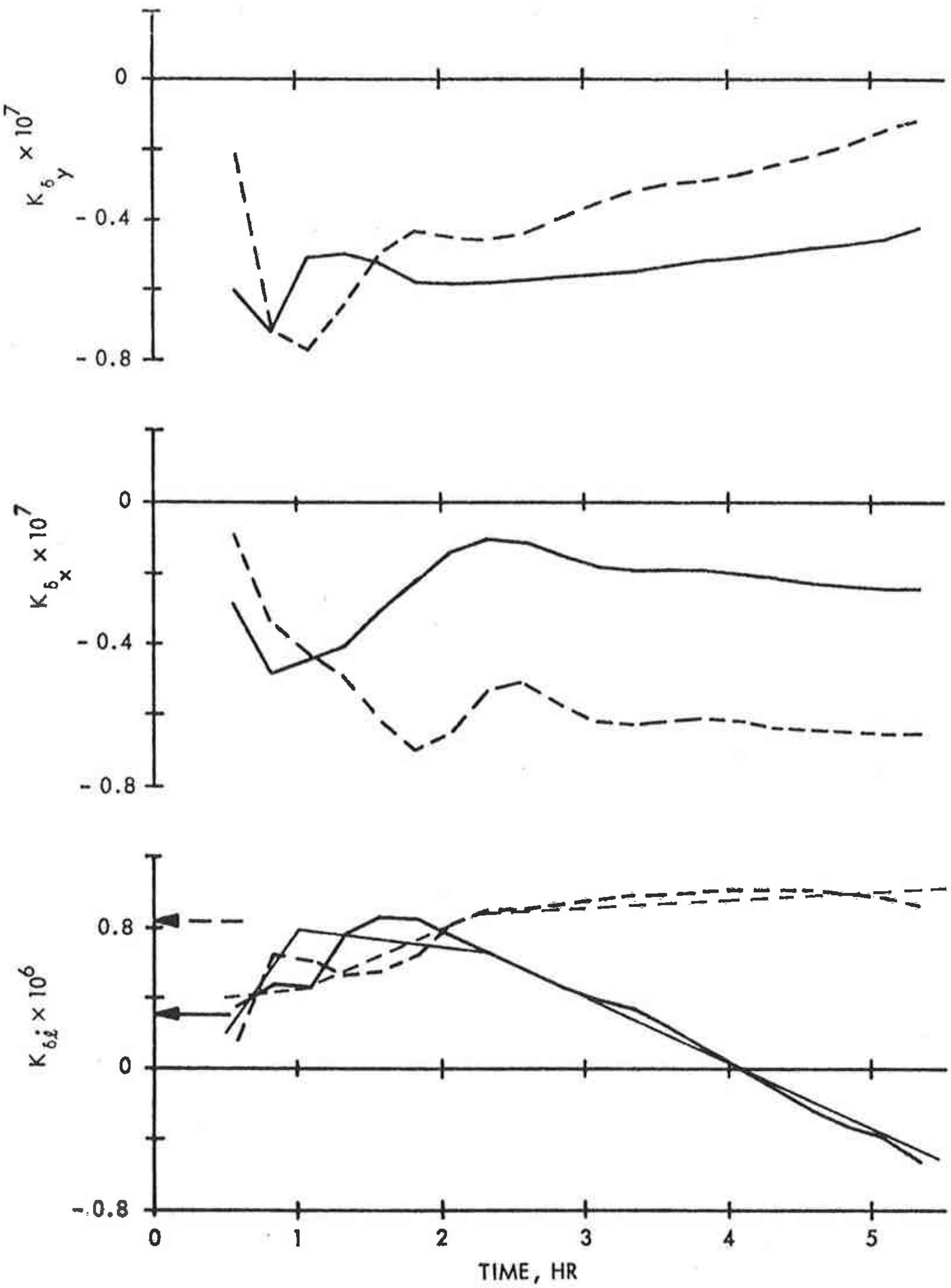

Figure 41. (Continued).

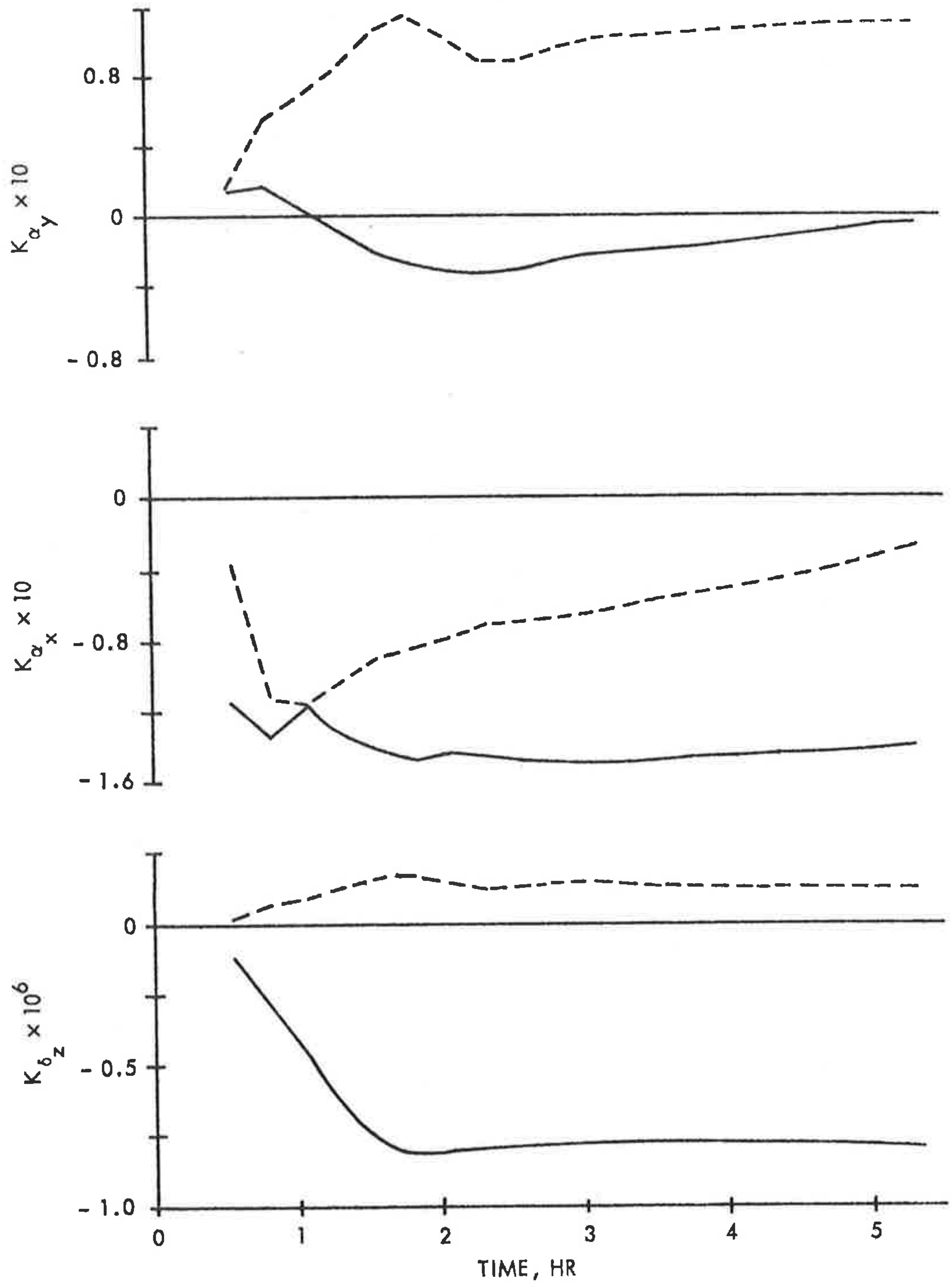

Figure 41. (Continued).

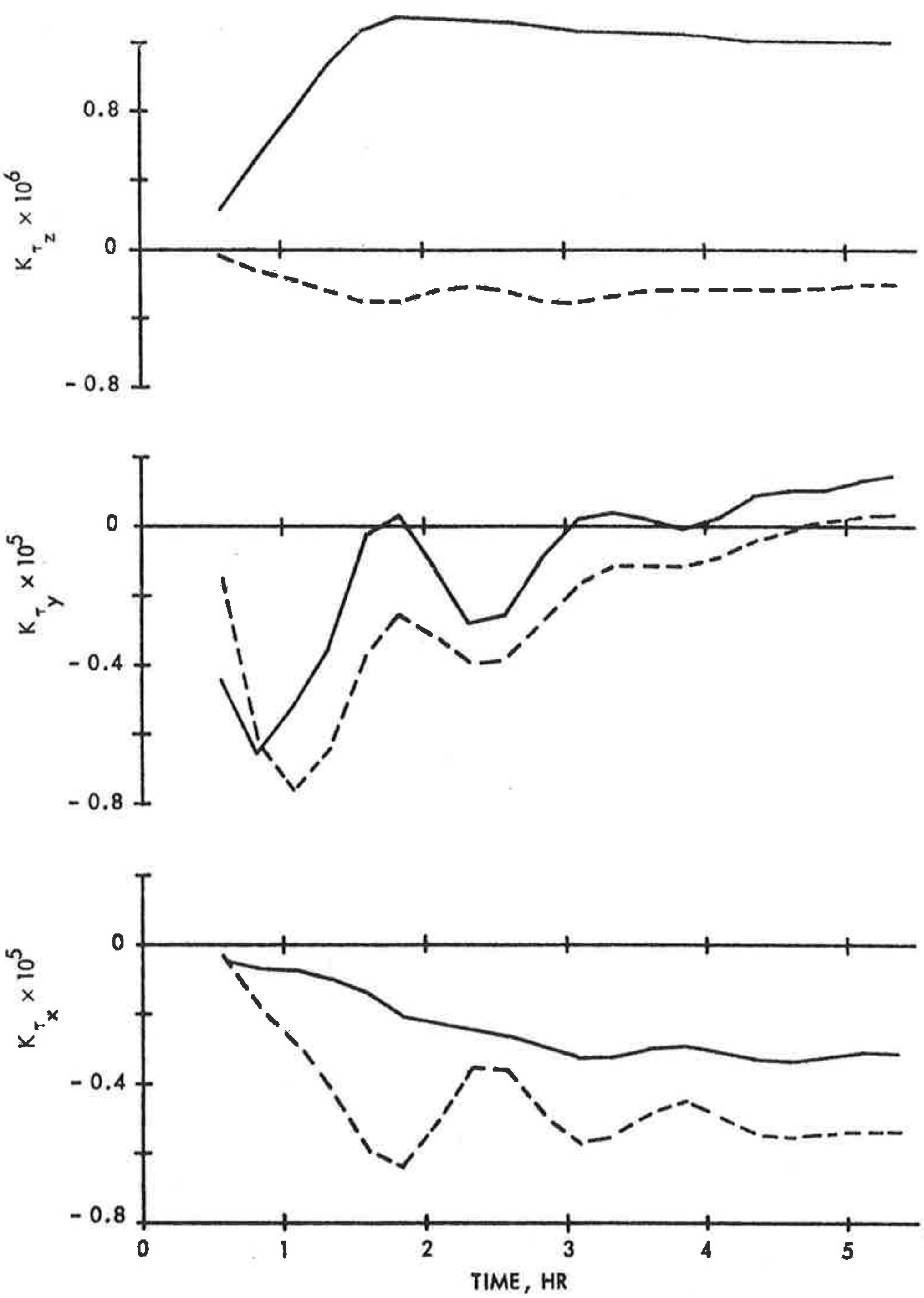

Figure 41. (Continued).

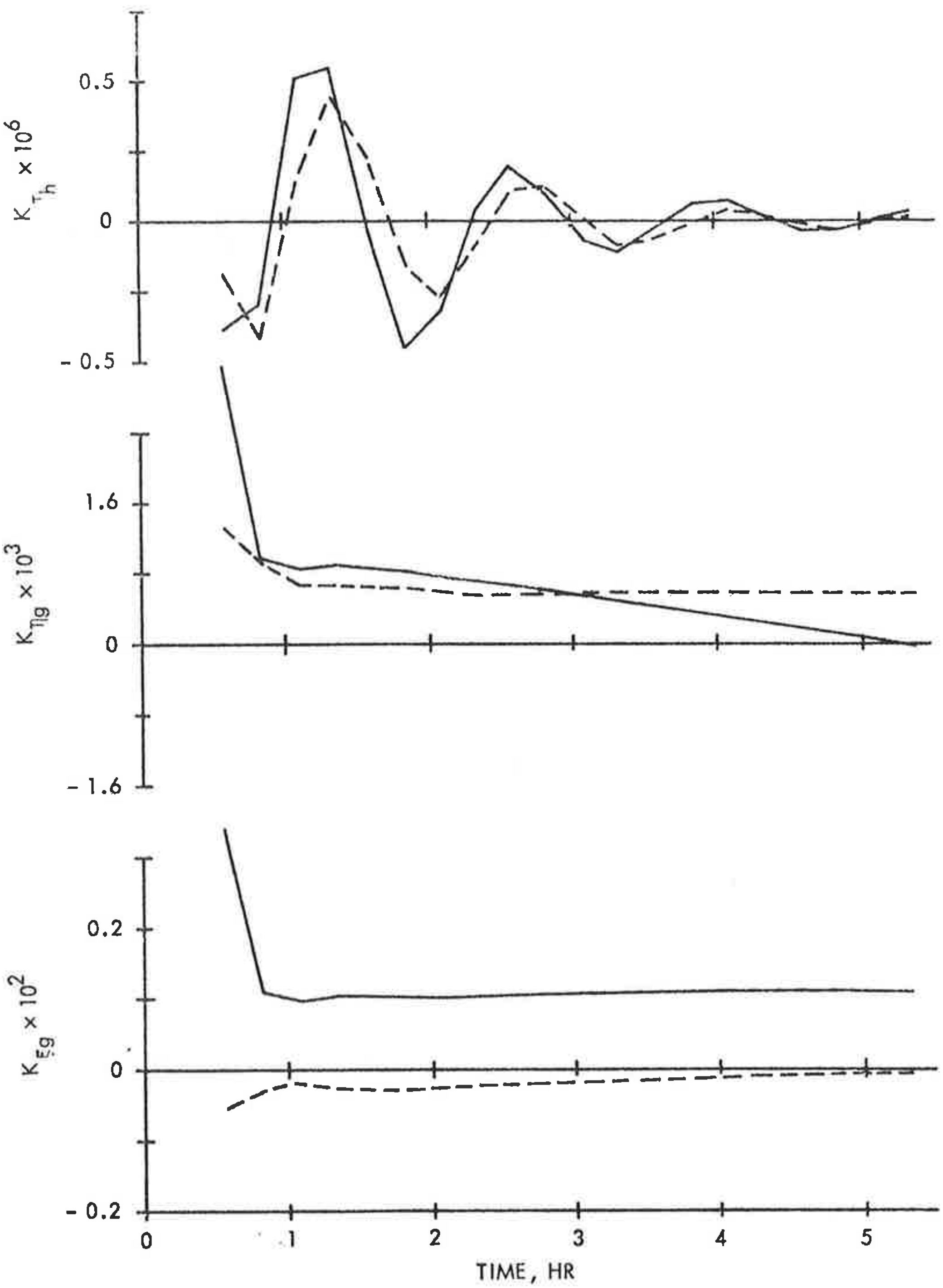

Figure 41. (Continued).

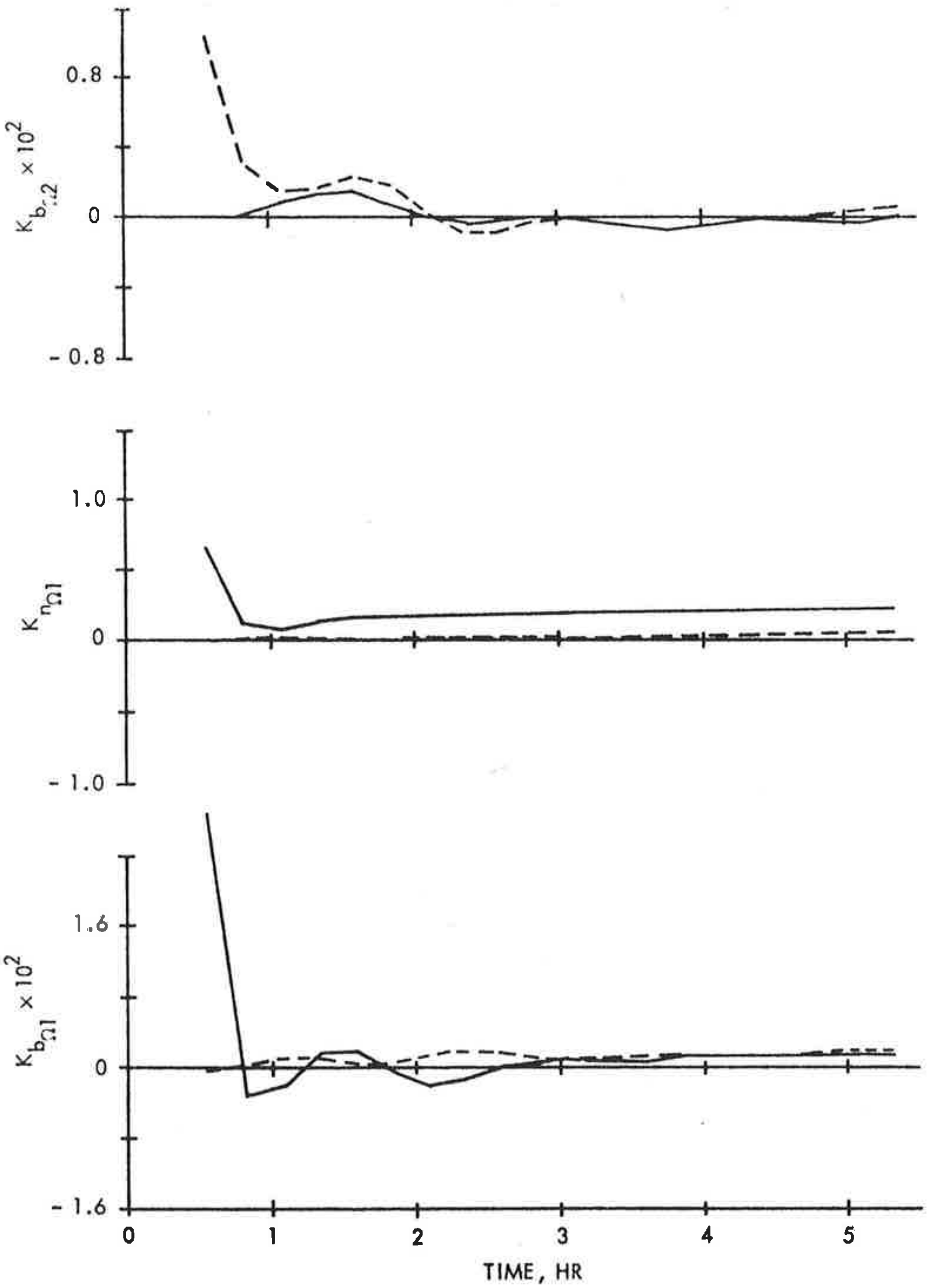

Figure 41. (Continued).

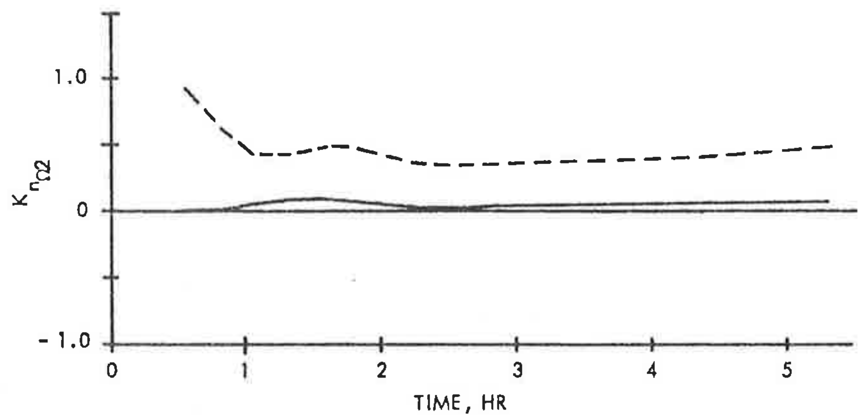

Figure 41. (Continued).

of piecewise-linear gains was chosen to approximate the first seven elements of $\underline{K}$ for each LOP. These are shown as dashed lines in Figure 41. The remaining suboptimum filter gains were zero. The resulting position and velocity errors are presented in Figures 42 and 43. The position uncertainties are very slightly larger than those obtained with the optimum gains (cf. Figure 32) during the first 90 min, and essentially the same thereafter. The velocity uncertainties remain a little larger than their optimum counterparts (Figure 33) throughout the flight.

Due to the very minor loss in accuracy suffered by the 14 piecewise-linear suboptimum gains discussed previously, a set of twelve constant gains was examined. These constant gains are also indicated in Figure 41 and their errors are compared with the previous results in Figures 44 and 45. The navigational accuracy is substantially poorer with the constant gains chosen; the RMS position uncertainty is nearly an order of magnitude greater than the optimum gains provided. Although the along-track errors are not too unreasonable, both the position and velocity cross-track uncertainties show a constant growth. In fact, the constant gains used actually produce occasional increases in the position and velocity uncertainties. Due to

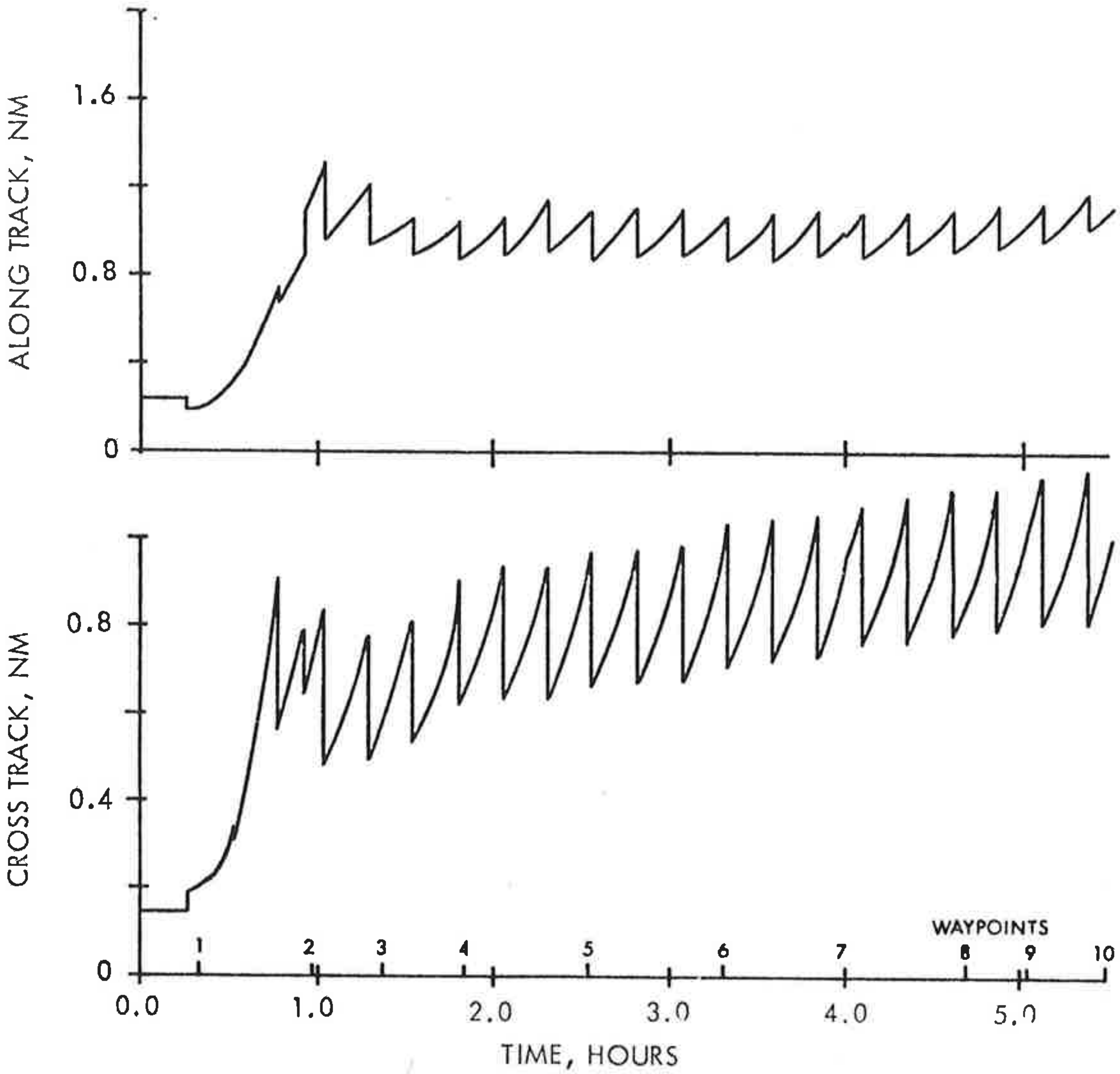

Figure 42. INS Position Errors with Piecewise-Linear Suboptimum Omega Gains.

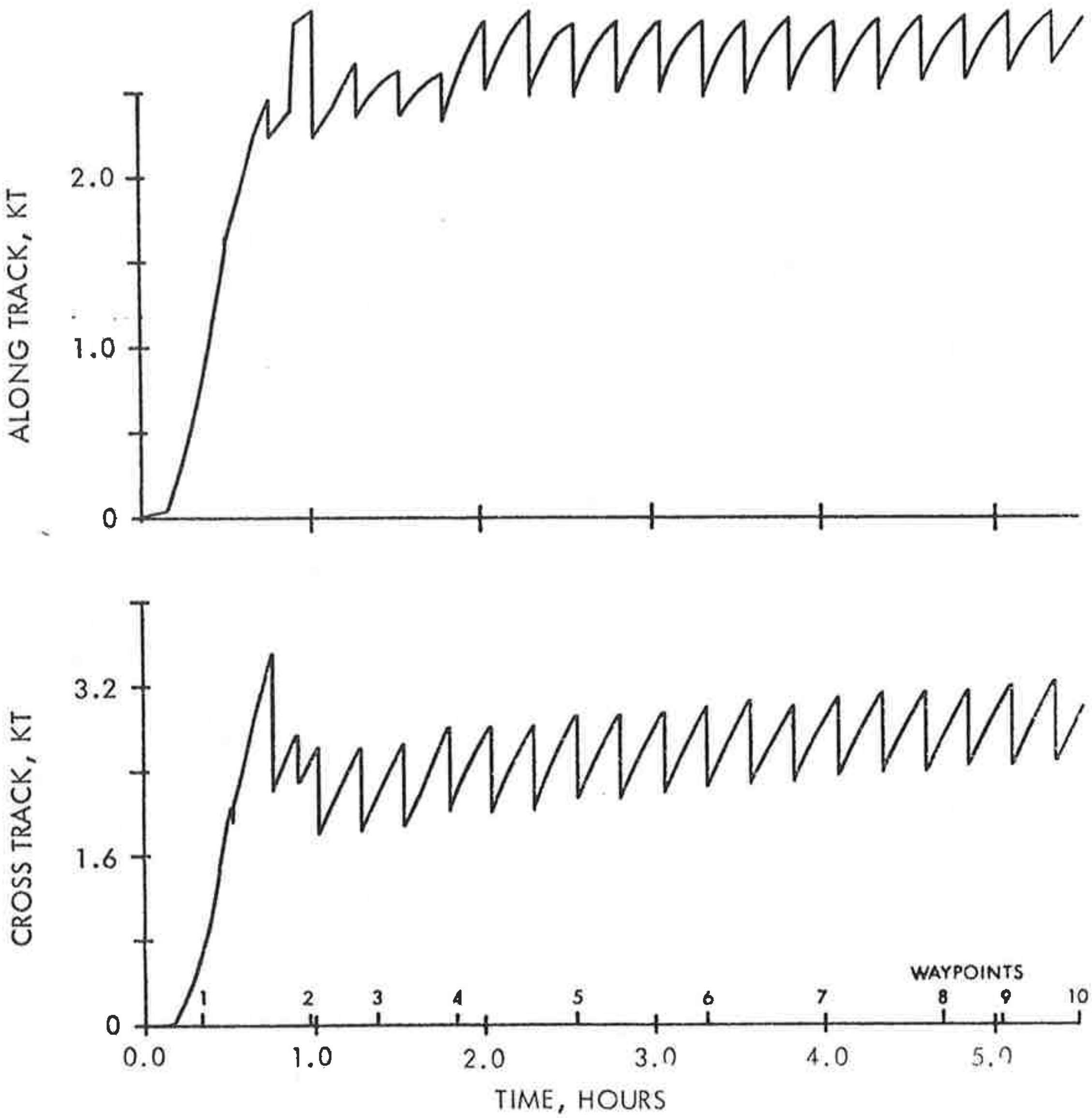

Figure 43. INS Velocity Errors with Piecewise-Linear Suboptimum Omega Gains.

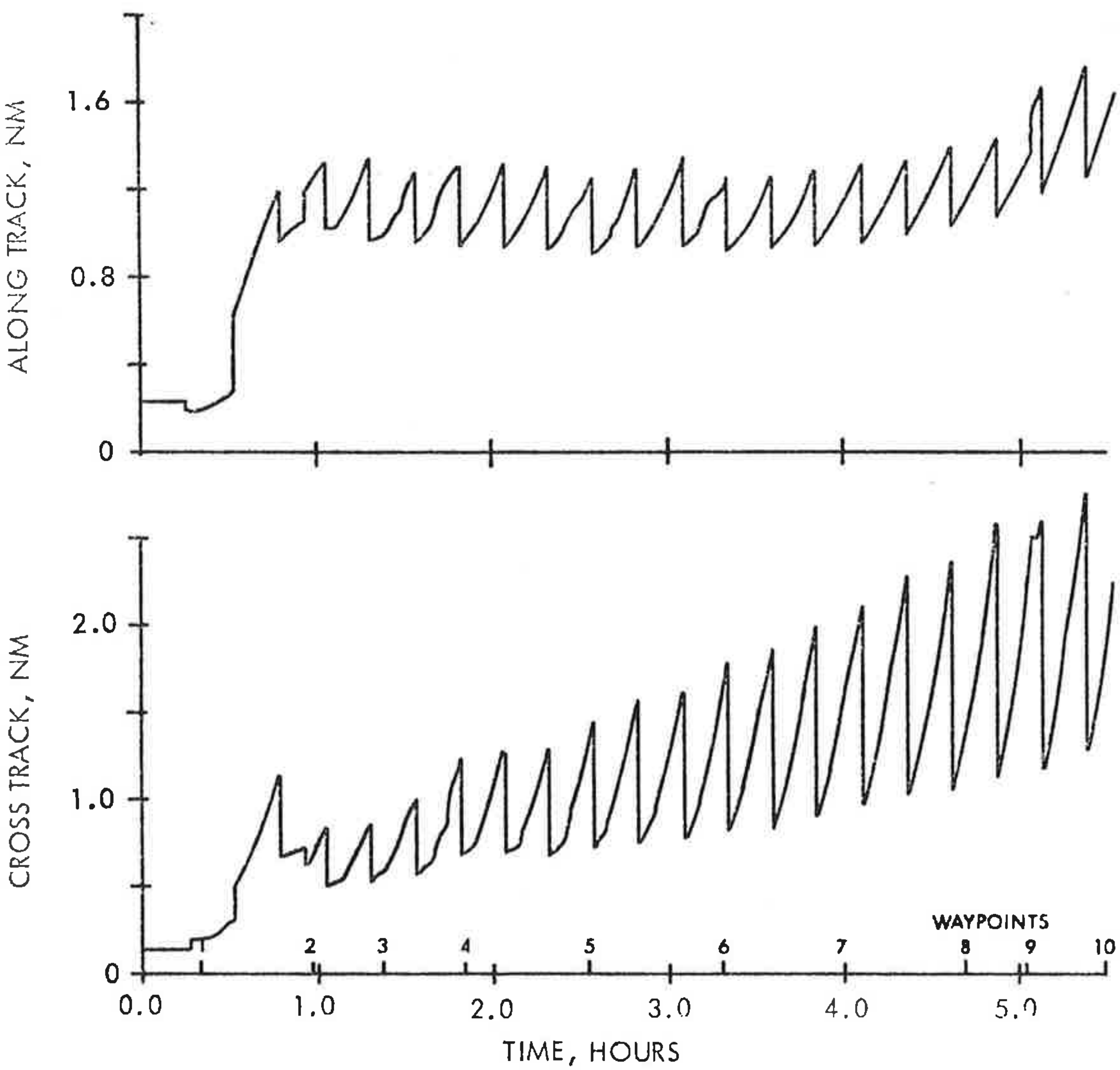

Figure 44. INS Position Errors with Constant Suboptimum Omega Gains.

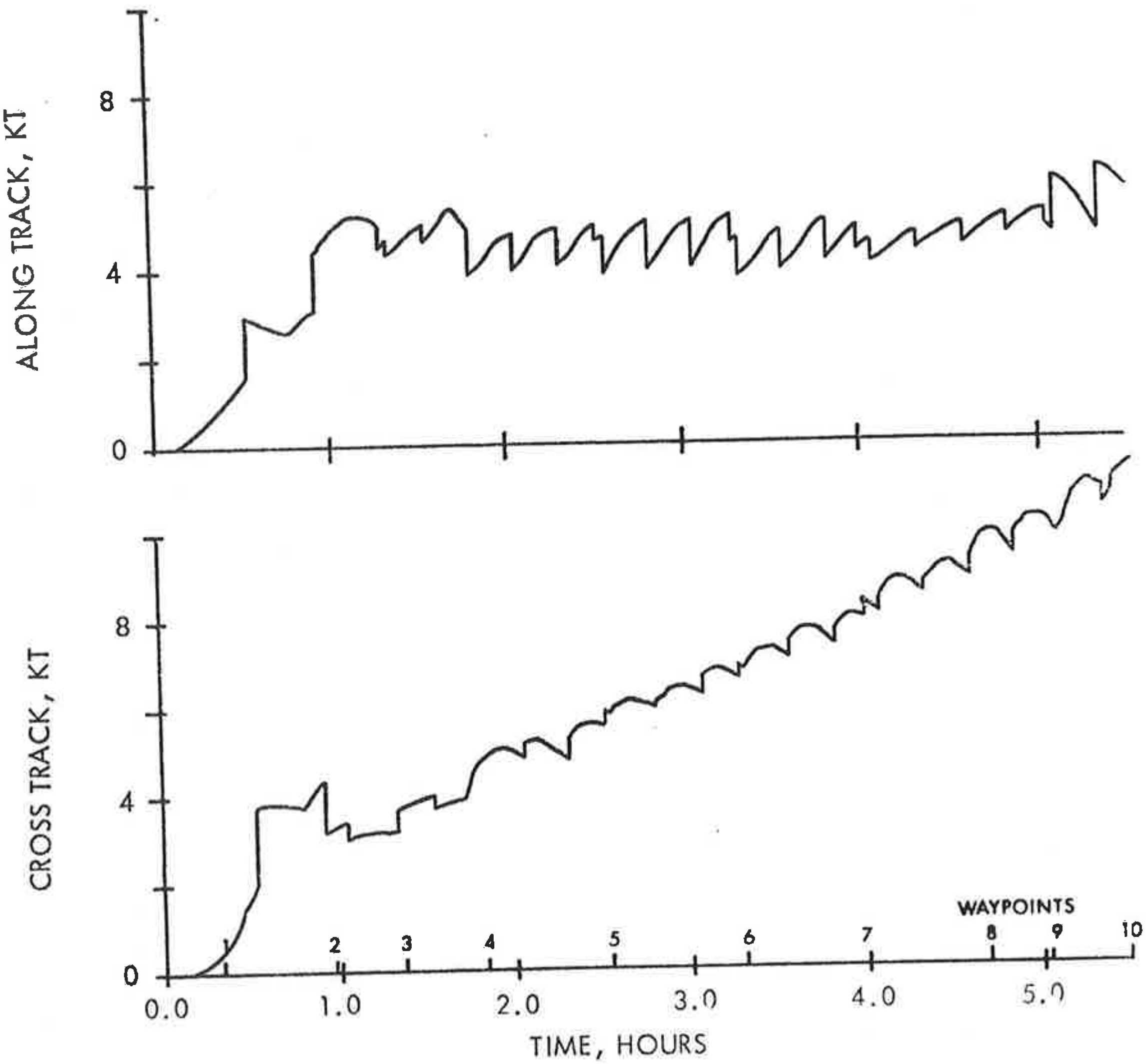

Figure 45. INS Velocity Errors with Constant Suboptimum Omega Gains.

the character of the gain histories in Figure 41, the selection of satisfactory constant gain schedules is not a straightforward process. However, it is possible that there exists another set of 12 or more constant gains which will provide reasonable performance.

7.8 EXAMPLE MALFUNCTIONS/BLUNDERS

To illustrate how the effects of various blunders or equipment malfunctions can be simulated with NATNAV, two hypothetical situations are presented. Both of these involve a discrete event at three hours' time on the nominal Boston-Shannon flight with Omega updates every 15 minutes.

The first situation involves a malfunction or blunder in the Omega navigator of a three-lane (10.2 kHz) shift in the first line-of-position measurement. This is represented by a 24 nm increase in the 1st LOP bias error, $b_{\Omega 1}$. Figures 46 and 47 show the resulting position and velocity errors. Although the error actually occurs at $t = 3$ hr, the effect does not appear until the next Omega update five minutes later. Due to the geometry of the 1st LOP (Trinidad - No. Dakota), the dominant effect of the lane shift is on the cross-track position error. In addition to the sudden increases in the position and velocity uncertainties, the lane shift also introduces large errors in the other estimates, including the platform misalignment angles. Subsequent updates eventually reduce these estimates again, but for the remainder of the flight, the INS alone is considerably less accurate than it was prior to the incorporation of the erroneous measurement information.

The second example of a malfunction is a sudden twofold increase in the drift rates of the INS gyros. This creates gradual increases in the INS misalignment angles, and consequently in the position and velocity uncertainties as shown in Figures 48 and 49. The end result is an increase in the RMS position uncertainty of about 1/4 nm at Shannon.

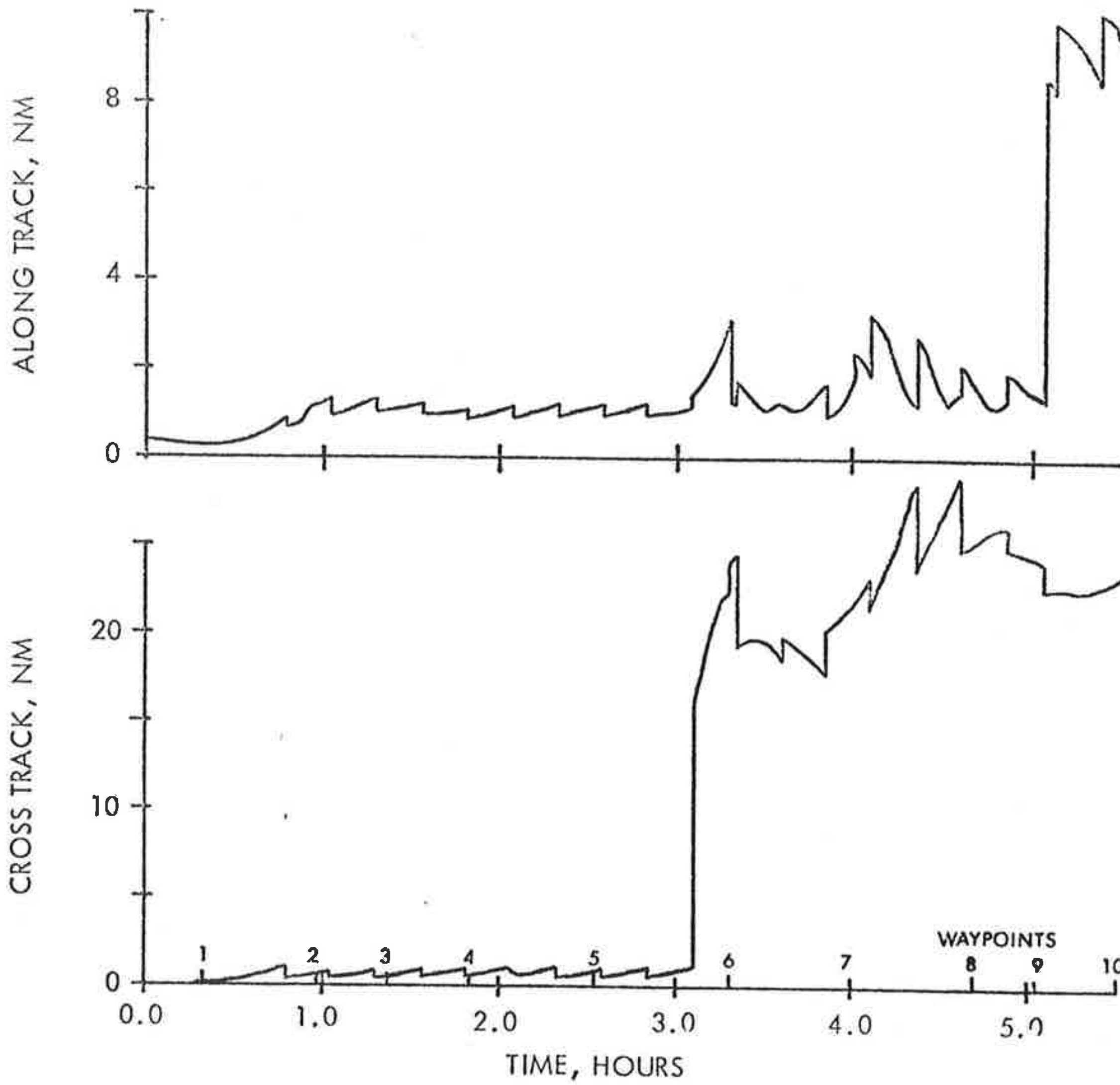

Figure 46. INS Position Errors with Omega Lane Shift.

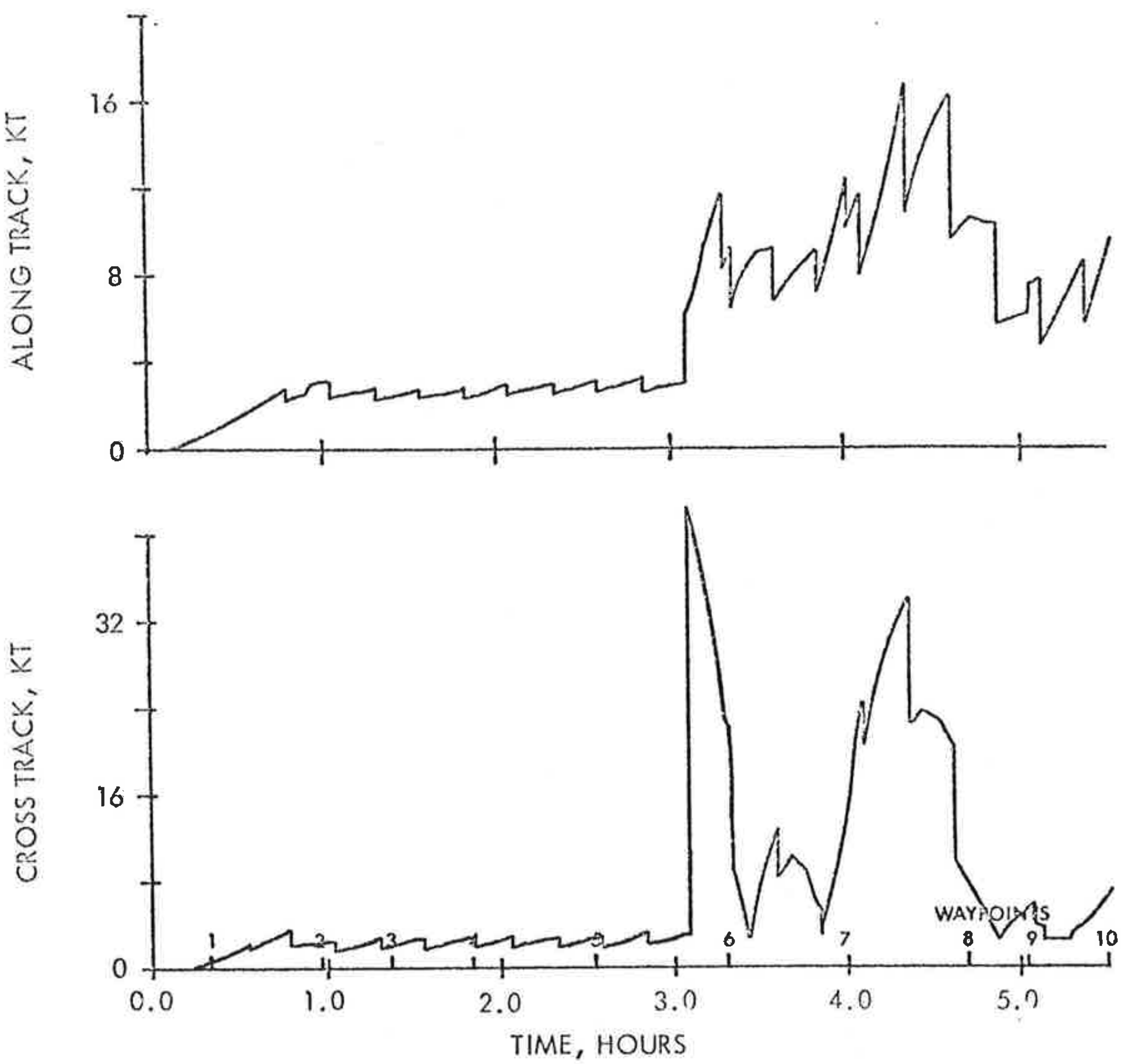

Figure 47. INS Velocity Errors with Omega Lane Shift.

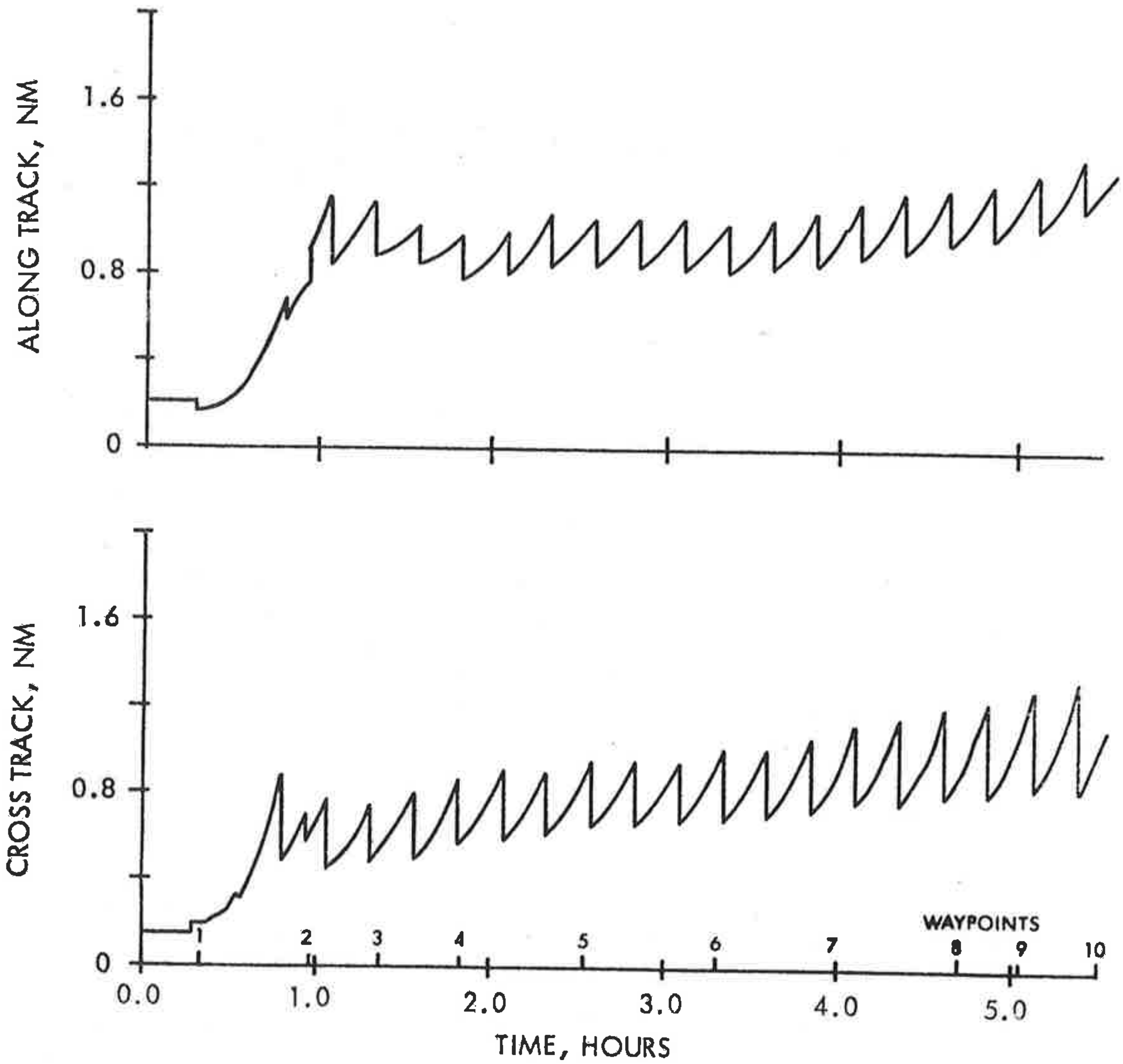

Figure 48. INS Position Errors with Increased Gyro Drifts.

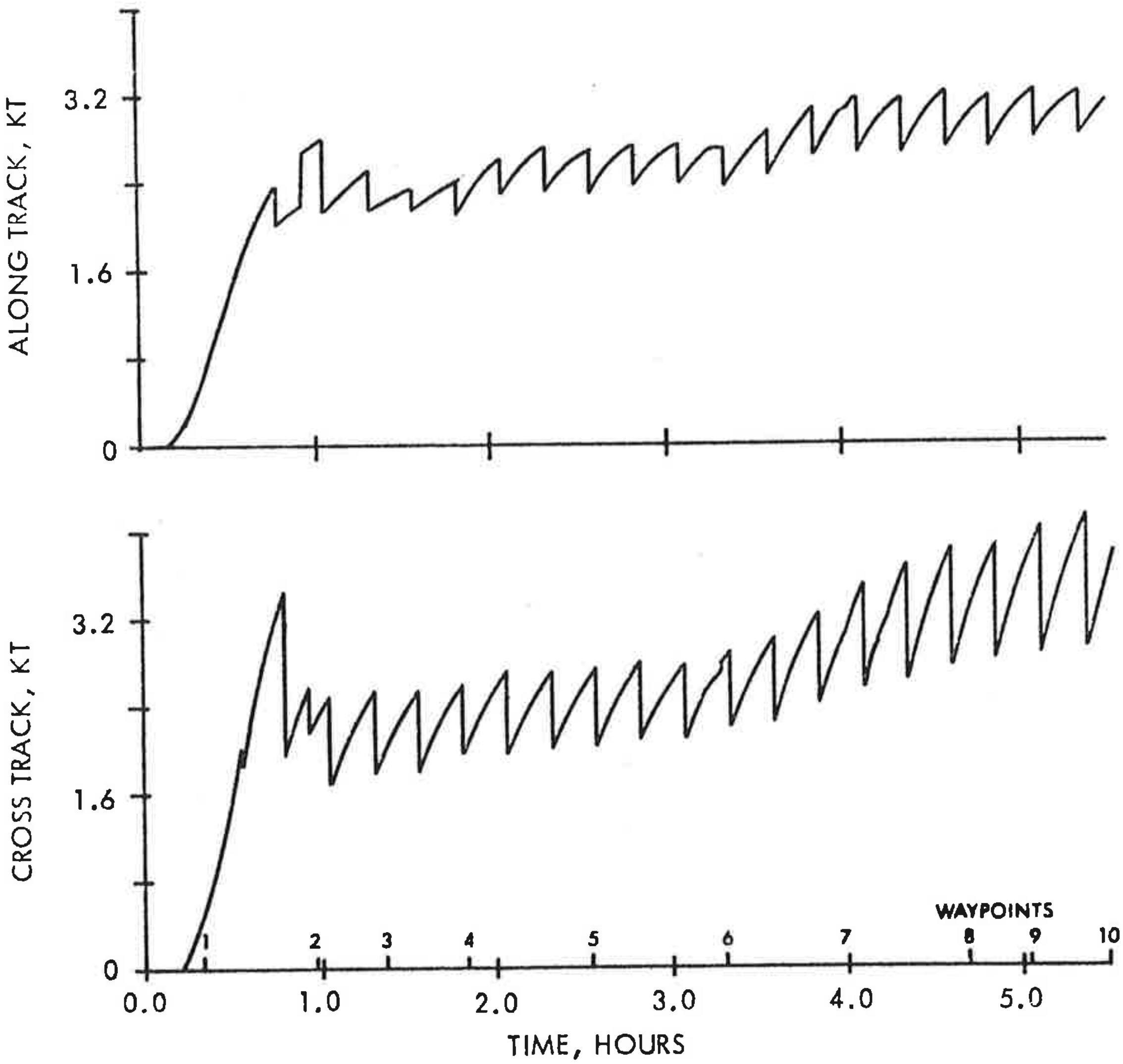

Figure 49. INS Velocity Errors with Increased Gyro Drifts.

SECTION 8

CONCLUSIONS AND RECOMMENDATIONS

This section presents a summary of the important conclusions of the NAT error analysis and modeling study, along with some suggested applications for the revised error models and possible additional improvements for the simulation.

8.1 SUMMARY OF CONCLUSIONS

The anticipated increase in traffic density across the North Atlantic will require increased capacity of the existing track routing structure. At the present time, the basic lane separation standards for the NAT region are

- Lateral — 120 nautical miles
- Longitudinal — 15 minutes
- Vertical — 2,000 feet

The principal means of increasing capacity is to reduce one or more of these separation standards. However, this must be achieved without adversely affecting the accepted collision risk standard, which has been established at 0.1 to 0.4 fatal accidents per 10 million flying hours. This can be accomplished by use of higher accuracy guidance and navigation aids such as augmented inertial navigation systems. For example, if separation standards could be safely reduced to 30 miles laterally and 8 minutes in trail with aided-inertial systems, the projected traffic increases could be handled with a much lower ATC-imposed penalty than today's traffic.

The objective of this study has been the development of a digital computer simulation program NATNAV (NAT NAVigation), for evaluating the performance of various aided-inertial navigation system configurations which might be used by commercial NAT aircraft. By simulating the errors of these hybrid navigation systems, Program NATNAV provides the information needed for subsequent analyses relating achievable performance of various configurations to separation standards and collision risk.

A hybrid navigator combines navigation information from two or more sources to provide estimates of position and velocity which are more accurate than those available from either source alone. A hybrid navigation system is also more reliable because the loss of either source of information still permits navigation with the remaining source(s). The present study was concerned with hybrid navigators which combine information from the following navigational aids:

- Inertial Navigation System
- Doppler Radar
- Air Data
- Omega
- Satellite Ranging

An ensemble error analysis approach was selected for the NATNAV simulation program over a Monte Carlo simulation for economy of computer time. The error equations are linearized about an assumed flight path, and the system errors are then mathematically described by a covariance matrix. The purpose of the simulation is to determine how the covariance matrix propagates with time while the aircraft takes fixes with its several sensors. The method requires that all the navigation system errors be described by a set of linear differential equations, driven by white (uncorrelated) noise. For system errors which are not modeled as white noise, "shaping filters" are introduced to convert white noise into appropriate "colored" noise which describes the correlated statistical behavior of the error sources. Thus the error state vector represents the hybrid navigator state augmented by the shaping filter states.

The error analysis is based on the minimum variance estimator derived by Kalman for the discrete measurement case. The discrete filter is chosen for this application to deal with the questions raised by non-periodic and incomplete measurements. The continuous filter can be simulated in the limit as the sampling time becomes very small. To incorporate measurements, the recursive navigation technique (Ref. 20) is used to avoid matrix inversion and to eliminate unnecessary computation on missing measurements. With this approach, each update of the covariance matrix involves one or more sequential scalar measurements.

The error state vector contains the basic INS errors, plus additional elements for each contributing error source in the complete system. A maximum dimension of 34 was selected to accommodate the situation of a three-dimensional INS augmented by Doppler, Satellite and Omega measurements. The possible elements of the state vector are as follows:

9 INS errors	3 platform misalignment angle errors 3 inertial position errors 3 inertial velocity errors
13 INS component error sources	3 gyro drifts - scale factor 3 gyro drifts - colored noise 3 accelerometer errors - colored noise 3 geodetic uncertainties - colored noise 1 altimeter error - scale factor
12 independent measurement errors	2 Doppler velocity errors - scale factor 2 Doppler velocity errors - colored noise 2 hyperbolic position fix errors - bias 2 hyperbolic position fix errors - colored noise 2 range measurement errors - bias 2 range measurement errors - colored noise

The INS error model was developed from a unified error analysis for terrestrial inertial navigation (Refs. 24 and 25). Self-alignment of the INS is provided with the Kalman filter by taking measurements of velocity prior to taxiing. The Doppler radar measurement errors are modeled as a scale factor error, a colored noise and white noise in both the forward and the lateral axes. Each of the Omega line-of-position measurements is assumed to be corrupted by a bias, a colored noise and white noise. Similarly, the error in each satellite-ranging measurement contains a bias, a colored noise and white noise. Both the altimeter and rate-of-climb indicator errors are represented by scale factor, colored noise and white noise; wind uncertainties are modeled as exponentially-correlated. Typical numerical values were selected for all the error model parameters.

The digital computer simulation program NATNAV was developed with a highly modular structure for greatest flexibility to analyze a variety of likely hybrid navigation system configurations, to allow for contingencies such as sub-system failures and blunders, and to enable evaluation of variable update rates, suboptimal filter schemes, aircraft maneuvers, etc. The program provides for an optimum initial alignment of the INS prior to taxi. A dead-reckoning option; i.e., no INS, is also available. Independent measurements using Doppler radar, Omega or satellite-ranging may be used to update the position and velocity estimates using the optimum recursive Kalman filter. As an alternative, suboptimum filter gains may be used. The operation of the simulation is controlled by the various program inputs, which include the nominal flight plan, the INS configuration and error statistics, and the aiding systems and their characteristics. The principal outputs of the program are the time histories of the standard deviations of the position and velocity errors, resolved into along-track, cross-track and vertical components.

NATNAV calculates the nominal time histories of the actual aircraft position and velocity, upon which the error covariances are based, from an input flight plan which closely resembles the information normally provided by actual flight plans. The error covariance matrix is propagated by numerical integration of up to 585 linear, first-order differential equations, using a fourth-order Runge-Kutta integration routine. In general, the hybrid navigator being analyzed will not require all 34 error states; for each state not used in the simulation, the appropriate row and column of the covariance matrix is discarded, reducing the number of equations to be integrated and hence computer time. The output of the program is a printout of the time histories of the nominal aircraft flight path and the standard deviations of the position and velocity errors and INS misalignment angles. Options are available for automatic plotting of the position and velocity errors, and for printout of the optimum filter gains.

A number of computer results were obtained for a typical North Atlantic flight from Boston, Massachusetts, to the Shannon, Ireland, coast-in point. The performance of the unaided INS was illustrated as a basis of comparison. The INS errors are due primarily to gyro drifts and accelerometer uncertainties. The accuracy of dead-reckoning without an INS depends almost entirely on the wind uncertainty. Omega and satellite-ranging updates bound the INS position error; the sample time determines the maximum values of the errors. Doppler measurements limit the velocity uncertainties, and a combined Doppler-Omega system provides very good estimates of both position and velocity. For the Omega-INS, many of the optimum filter gains can be neglected, and a simple approximation of the remaining gains provides nearly-optimum performance. Finally, two examples show how the suboptimum gain option of NATNAV can be used to simulate discrete malfunctions or blunders.

8.2 RECOMMENDATIONS FOR ADDITIONAL STUDY

Following are some potential applications for the NATNAV simulation, and some suggestions for possible extensions of the present program.

A principal motivation for developing the simulation was to provide information for subsequent collision risk analyses. Error histories would be computed for selected navigation system configurations. As described in the user's manual, these error histories can be saved on magnetic tape for later analysis if desired. Depending on the collision risk model, these NATNAV outputs can be used to specify the appropriate input parameters, or as direct inputs. The collision risk analysis can then be exercised to determine the allowable separation standards as functions of the navigation system configurations.

A related application would be a sensitivity study to investigate the effects of various parameters of the navigation system accuracy. The results of such a study would provide valuable information for selecting/specifying the features of future navigation systems for NAT operations. A wide variety of effects could be investigated, such as: INS accuracies; Omega, Doppler and satellite measurement error statistics; selection of Omega stations; positions of navigation satellites; measurement update rates; alternate flight routes; etc. Such studies would not necessarily be restricted to North Atlantic flights, but could also be useful for North and South Pacific operations, polar flights or even domestic routes.

One area which is very closely related to collision risk analyses is the effects of human blunders or equipment malfunctions. By their very nature, such errors are unpredictable, and, hence, indescribable by normal statistical terms. However, they have a substantial impact on the "tails" of the error distributions, which are the principal determinants in a collision risk analysis. A study of malfunctions/blunders which have been experienced in the past and others which might be hypothesized could provide valuable inputs to a risk analysis. The effects of specific blunders could be evaluated with NATNAV. Empirical observations might be used to assign some estimated probabilities to the occurrence of such events. The result would be an evaluation of blunder/malfunction statistics for subsequent collision risk analyses.

Although all commercial INS's are presently local-level mechanizations or variations thereof, strapdown systems are being considered for the future. NATNAV does contain an approximate strapdown model which could be used for preliminary error analyses, but some program modifications would be necessary to accurately simulate the performance of a particular strapdown system. The existing model ignores the effects of accelerations during maneuvers, and neglects all attitude dynamics of the aircraft. These factors should be added to an improved model. Other important effects which should be included are the representation of the strapdown system's computational algorithms, and the airborne computer characteristics (e.g. speed, word length, etc.).

Because of its modular construction, NATNAV could be readily adapted to evaluate the effects of alternate or additional aiding navigation systems, such as VORTAC, LORAN, DECCA, etc. For example, a hyperbolic system such as LORAN could be easily implemented by replacing the existing Omega model. Similarly, a range-range or range-azimuth system, such as DME/DME or VOR/DME, could be readily incorporated as a replacement for the satellite-ranging system. Additional models could be added to those now contained in NATNAV, but this would require augmenting the error-state vector (already 34th order) and result in increased storage requirements for the program.

Another useful modification to the program would be the development of a time-sharing version, which would enable the user to quickly evaluate the

15. Kalman, R. E. and Bucy, R. S., "New Results in Linear Filtering and Prediction Theory", Transactions of the ASME, Series D., Journal of Basic Engineering, Vol. 83, March 1961, pp. 95-108.

16. Brock, L. D. and Schmidt, G. T., "Statistical Estimation in Inertial Navigation Systems", Journal of Spacecraft and Rockets, Vol. 5, No. 2, February 1968, pp. 146-153.

17. Zimmerman, W., "Optimum Integration of Aircraft Navigation Systems", IEEE Transactions on Aerospace and Electronic Systems, Vol. AES-5, No. 5, September 1969, pp. 737-747.

18. Gelb, A. and Sutherland, A. A., "Software Advances in Aided Inertial Navigation Systems", Navigation: Journal of the Institute of Navigation, Vol. 17, No. 4, Winter 1970-1971, pp. 358-369.

19. Bryson, A. E. and Ho, Y. C., "Applied Optimal Control", Blaisdell, 1969.

20. Battin, R. H., "Astronautical Guidance", McGraw-Hill, 1964.

21. Anon., "Technical Description - Litton LTN-51 INS System for Commercial Aviation," Publication No. 6363, Litton Systems, Woodland Hills, California, October 1970.

22. Anon., "Carousel IV Inertial Navigation System - System Technical Description", AC Electronics, 1969.

23. Anon., "INS-61B Inertial Navigation System", 523-0746229-00111P, Collins Radio Company, Cedar Rapids, Iowa, December 7, 1971.

24. Britting, K. R., "Inertial Navigation Systems Analysis", Wiley Interscience, 1971.

25. Britting, K. R., "Unified Error Analysis of Terrestrial Inertial Navigation Systems", AIAA Paper No. 71-901, AIAA Guidance, Control and Flight Mechanics Conference, Hofstra University, August 16-18, 1971.

26. Bergli, O. D., "A Computer Program for Evaluation of Error Covariances in Terrestrial Navigation Systems", RN-70, MIT Measurement Systems Laboratory, August 1971.

27. Britting, K. R., et al., "Assessment of the Impact of Gradiometer Techniques on the Performance of I.N.S.", RE-78, MIT Measurement Systems Laboratory, 1971.

28. Ryan, T. J., "Alignment and Calibration of a Strapdown Inertial Measuring Unit", MIT Measurement Systems Laboratory, RE-67, December 1970.

29. Ruetenik, J. R., Thompson, J. H. and Britting, K. R., "Study of the Concept of Inertially-Aided Barometric Altimetry System for Supersonic Aircraft", NASA CR-1770, June 1971.

30. Fried, W. R., "Modern Aircraft Navigation Sensors for Hybrid Systems", AGARD Conference Proceedings No. 54, Guidance and Control Panel 9th Meeting, Delft, Netherlands, September 22-26, 1969.

31. Kayton, M. and Fried, W. R. (eds.), "Avionics Navigation Systems", John Wiley and Sons, 1969.

32. Scott, R. E., "Study and Evaluation of Omega Navigation System for Transoceanic Navigation in Civil Aviation", Final Report RD-69-39, Radio Science Laboratory, University of Michigan, August 1969.

33. Pierce, J. A. "Omega", IEEE Transactions on Aerospace and Electronic Systems, Vol. AES-1, No. 3, December 1965, pp. 206-215.

34. Hollister, W. M. and Bansal, D. D., "Guidance and Control for V/STOL Aircraft: Final Report", RE-77, MIT Measurement Systems Laboratory, November 1970.

35. Anderson, R. E., "A Concept for Navigation and Communication Using Satellites", Journal of the Institute of Navigation, Vol. 19, No. 1, January 1966, pp. 2-22.

36. Anon., "Oceanic ATC Surveillance Systems Study", DOT-TSC-260-1, Systems Control, Inc., February 1972.

37. Anon., "System Analysis of the North Atlantic Air Traffic Complex", Final Report on FAA Contract FAA/BRD-334, ARCON Corporation, December 1962.

38. Hildebrand, F. B., "Advanced Calculus for Applications", Prentice-Hall, 1962.

BIBLIOGRAPHY

Abbott, M. D., "Some Remarks in the Distribution of Aircraft Track Keeping Errors", Journal of the Institute of Navigation, Vol. 18, No. 3, July 1965.

Abbott, M. R., "Digital Simulation Study of an Idealized Model of a Computer-Controlled Procedural Free-Route System for North Atlantic Air Traffic", TR 66147, Royal Aircraft Establishment, May 1966.

Anderson, E. W. and Ellis, D. M., "Error Distributions in Navigation", Journal of the Institute of Navigation, Vol. 24, No. 4, October 1971, pp. 429-442.

Asche, G. P., "Implementation Status of the Omega Navigation System", The Institute of Navigation, Proceedings of the First Omega Symposium, Washington, D. C., November 9-11, 1971, pp. 35-39.

Attwooll, V. W., "The Parallel-route System for North Atlantic Subsonic Jet Traffic", Journal of the Institute of Navigation, Vol. 19, No. 2, April 1966, pp. 187-197.

Attwooll, V. W., "Parallel-route Systems for Supersonic Traffic", Journal of the Institute of Navigation, Vol. 19, No. 3, July 1966, pp. 348-360.

Bansal, D. D., "Better Accuracy by Optimum Mixing of Data from Inertial and Some Radio Navigation Systems", TE-38, MIT Measurement Systems Laboratory, June 1970.

Barham, P. M. and Manville, P., "Application of Kalman Filtering to Baro/Inertial Height Systems", AGARDograph 139, Theory and Applications of Kalman Filtering, April 1970, pp. 269-281.

Baziw, J. and Leondes, C. T., "In-Flight Alignment and Calibration of Inertial Measurement Units", IEEE Transactions on Aerospace and Electronic Systems, Vol. AES-8, No. 4, July 1972, pp. 439-466.

Bona, B. E. and Hutchinson, C. E., "Optimum Reset of an Inertial Navigation From Satellite Observations", National Electronics Conference Proceedings 21, 1965, pp. 569-574.

Brandel, P. L., et al., "Communications, Navigation and Surveillance for Aircraft and Marine Vessels Operating in the North Atlantic Region", DOT TSC Report, 1970.

Brayard, M. C., "Optimum Mixing of Inertial Navigator Data and Radar Data", TE-29, MIT Experimental Astronomy Laboratory, June 1969.

Brink, D., "Oceanic ATC Automation at Oakland", Journal of ATC, January-February 1973, pp. 14-15.

Britting, K. R.,"Final Report: Analysis of Oceanic Air Traffic Control Navigation Systems", RN-67, MIT Measurement Systems Laboratory, July 1971.

Brock, L. D. and Schmidt, G. T., "General Questions on Kalman Filtering in Navigation Systems", AGARDograph 139, Theory and Applications of Kalman Filtering, April 1970, pp. 203-230.

Brown, R. G. and Hagerman, L. L., "An Optimum Inertial/Doppler-Satellite Navigation System", Navigation: Journal of the Institute of Navigation, Vol. 16, No. 3, Fall 1969, pp. 260-270.

Bryant, W. B., Simpson, R. W. and Trueblood, R. B., "Inertial Navigation and Guidance for Civil Air Transport", Journal of the Institute of Navigation, Vol. 18, No. 4, October 1965, pp. 457-474.

Bryson, A. E., Jr. and Bobick, J. C.,"Updating Inertial Navigation Systems with VOR/DME Information", AIAA Paper No. 72-846, AIAA Guidance and Control Conference, Stanford, California, August 14-16, 1972.

Burrows, J. W., "Combined Inertial - ILS Aircraft Navigation Systems", Journal of Aircraft, Vol. 8, No. 6, June 1971, pp. 439-443.

Calvert, B. J., "Carousel IV in the 747", Flight International, July 1, 1971, pp. 16-17.

Clark, J. M., "Aircraft Navigation Using Omega", IEEE Transactions on Aerospace and Electronic Systems, Vol. AES-5, September, 1969, pp. 756-761.

Couzens, R., "The Accuracy of Corrected Omega Close to a Transmitter", The Institute of Navigation, Proceedings of the First Omega Symposium, Washington, D.C., November 9-11, 1971, pp. 54-55.

Craigie, J. H., et al., "Navigation/Traffic Control Satellite Mission Study", Volumes I, II, III, TRW Systems Corp., Contract No. NAS-12-595, June, 1969.

Crocker, E. B. and Rabins, L., "Application of Kalman Filtering Techniques to Strapdown System Initial Alignment", AGARDograph 139, Theory and Applications of Kalman Filtering, April, 1970, pp. 491-512.

Crook, W. G. and Sulzer, R. L., "Simulation and Analysis of Over-Ocean Separation Assurance Procedures and Displays", NA-68-14 (RD-67-43), FAA NAFEC, February 1968.

Diamond, P. M., "The Potential of a System of Satellites as a Part of an Air Traffic Control System", AGARD-CPP-105, June 1972, pp. 20-1-20-17.

Dworkin, B., "Standardization of Aeronautical Navigation/Guidance Enabled by Omega", The Institute of Navigation, Proceedings of the First Symposium, Washington, D. C. , November 9-11, pp. 155-164.

Dunmire, C. E., "Estimated Instantaneous Airborne Traffic in the North Atlantic", (N72-12585), Federal Aviation Administration, May 1970.

Eisenberg, R. L., Thornhill, A. F. and Williams, M. F., "Development and Flight Testing of Pre-Production Omega Aircraft Receivers and Antennas", The Institute of Navigation, Proceedings of the First Omega Symposium, Washington, D. C., November 9-11, 1971, pp. 144-154.

Euler, E. A. and Adams, G. L., "Generalized Covariance Analysis for Navigation Filter Design and Performance Evaluation", AIAA Paper No. 72-14, AIAA 10th Aerospace Sciences Meeting, San Diego, California, January 17-19, 1972.

Findley, D. E., "Satellite Considerations in Future Air Traffic Control Systems", AGARD-CPP-105, June 1972, pp. 30-1 - 30-9.

Fried, W. R., "Performance Analysis and Future Outlook of Doppler Navigation Systems", Navigation, Vol. 6, No. 5, Spring 1959, pp. 284-292.

Halamandaris, H. and Ozdes, D., "A Kalman Filter Augmented Marine Navigation System", AGARDograph 139, Theory and Applications of Kalman Filtering, April 1970, pp. 513-537.

Hawkes, K. H., Jr. and Birnbaum, D., "Integration and Flight Test of an Omega Receiver with the P-3C Aircraft Navigation System", The Institute of Navigation, Proceedings of the First Omega Symposium, Washington, D. C., November 9-11, 1971, pp. 190-201.

Heffes, H., "The Effect of Erroneous Models on the Kalman Filter Response", IEEE Transactions on Automatic Control, Vol. AC-11, No. 3, July 1966, pp. 541-542.

Hershkowitz, R. M., "Collision Risk Model for NAT Region", DOT-TSC-FAA-71-6, DOT Transportation Systems Center, May 1971.

Hershkowitz, R. M., O'Mathuna, D. and Britting, K. R., "The Impact of Inertial Navigation on Air Safety", Navigation, Vol. 18, No. 3, Fall 1971, pp. 298-307.

Hollister, W. M., and Brayard, M. C., "Optimum Mixing of Inertial Navigator and Position Fix Data", Journal of Aircraft, Vol. 8, No. 9, September 1971, pp. 698-703.

Huddle, J. R., "Application of Kalman Filtering Theory to Augmented Inertial Navigation Systems", AGARDograph 139, Theory and Applications of Kalman Filtering, April 1970, pp. 231-268.

Hutchinson, C. E., "Design of Low Sensitivity Kalman Filters for Hybrid Navigation Systems", AGARD Conference Proceedings No. 54, Guidance and Control Panel 9th Meeting, Delft, Netherlands, September 22-26, 1969.

Kaminski, P. G., Bryson, A. E. and Schmidt, S. F., "Discrete Square Root Filtering: A Survey of Current Techniques", IEEE Transactions on Automatic Control, Vol. AC-16, No. 6, December 1971, pp. 727-736.

Kasper, J. F., Jr., "Evaluation of Omega Configurations for Airways Systems Operations", Proceedings of the ION National Air Meeting, Saddle Brook, New York, April 14-16, 1971.

Kasper, J. F., Jr. and Creekmore, E. E., "Omega Utilization by Non-Military Subscribers", The Institute of Navigation, Proceedings of the First Omega Symposium, Washington, D. C., November 9-11, 1971, pp. 106-112.

Keane, L. M., "Multibeam Aeronautical Satellite System Design", DOT-TSC-FAA-71-30, DOT Transportation Systems Center, December 1971.

Klass, P. J., "Omega Navaid Aviation Use Studied", Aviation Week and Space Technology, Vol. 97, No. 22, November 29, 1971, pp. 38-42.

Klass, P. J., "Promise Seen for Hybrid ATC", Aviation Week and Space Technology, Vol. 97, No. 12, September 18, 1972, pp. 52ff.

LaFond, C. D., "Airline Interest in Omega as Long-Range Navaid is on the Climb", Air Transport World, Vol. 9, No. 9, September 1972, pp. 83ff.

Leaver, C. A., "Omega Polar Navigation Performance", The Institute of Navigation, Proceedings of the First Omega Symposium, Washington, D.C. November 9-11, 1971, pp. 165-172.

Leonard, B. P., "Characteristics of a Satellite Navigation System Operating In Conjunction with a User Inertial System", AGARD Conference Proceedings No. 54, Guidance and Control Panel 9th Meeting, Delft, Netherlands, September 22-26, 1969.

Leondes, C. T. (ed.), "Hybrid Navigation Systems", AGARD Conference Proceedings No. 54, Guidance and Control Panel 9th. Meeting, Delft, Netherlands, September 22-26, 1969.

Leondes, C. T., (ed.), "Theory and Applications of Kalman Filtering", AGARDograph 139, University of California, Los Angeles, 1970.

Levine, S. A. and Gelb, A., "Effect of Deflections of the Vertical on the Performance of a Terrestrial Inertial Navigation System", Journal of Spacecraft and Rockets, Vol. 6, No. 9, pp. 978-984.

Lord, R. N., "Separation Standards and Aircraft Wander", Journal of the Institute of Navigation, Vol. 19, No. 2, April 1966, pp. 198-208.

Lord, R. N., and Overton, D. A., "Synthesis of the Aircraft Navigational Across-Track Error", Report E & C No. 2, Cranfield Institute of Technology, March 1971.

MacKinnon, D. and Madden, P., "Performance Limits on an Aircraft Inertial-Based Stochastic Lateral Guidance System," Journal of Aircraft, Vol. 9, No. 3, March 1972, pp. 217-222.

MacKinnon, D. and Hursh, J. W., "The Role of Inertial Navigation in Future Air Traffic Control Systems", Navigation, Vol. 18, No. 3, Fall 1971, pp. 320-330.

Mactaggart, D., "Design and Performance of CMA-719 Computerized Airborne Omega Receiver", The Institute of Navigation, Proceedings of the First Omega Symposium, Washington, D.C., November 9-11, 1971, pp. 63-74.

Madigan, R. J. and Canniff, J., "Flight Test Report of Experiments in Inertial Navigation System Updating", AIAA Paper No. 69-842, AIAA Guidance, Control and Flight Mechanics Conference, Princeton, New Jersey, August 18-20, 1969.

Martin, S. C. and Davies, W. D. T., "A Simplified Correlation Technique for Position Location Using Earth Satellites", AIAA Paper No. 72-564, 4th. Communications Satellite Systems Conference, Washington, D.C., April 24-26, 1972.

Matthews, A., "A Special Omega Navigation Configuration Can Meet Airline Needs", ICAO Bulletin, Vol. 28, No. 3, March 1973, pp. 19-22.

Meier, R. W., "NAT Aeronautical Satellite System Development", Proceedings of the IEEE, Vol. 58, No. 3, March 1970, pp. 448-455.

Miller, B., "Omega Improves Multisensor Accuracy", Aviation Week and Space Technology, Vol. 97, No. 18, October 30, 1972, pp. 48-49.

Miller, B. J., "The C-5 Navigation System - An Application of Digital Synergistic Stochastic Hybrid Navigation Technology", AGARD Conference Proceedings No. 54, Guidance and Control Panel 9th Meeting, Delft, Netherlands, September 22-26, 1969.

Mitchell, M. W., "Global Navigation/Traffic Surveillance/Communication Satellite System for Military and Civil Vehicles", AGARD Conference Proceedings No. 54, Guidance and Control Panel 9th Meeting, Delft, Netherlands, September 22-26, 1969.

Nash, R. A., D'Appolito, J. A. and Roy, K. J., "Error Analysis of Hybrid Aircraft Inertial Navigation Systems", AIAA Paper No. 72-848, AIAA Guidance and Control Conference, Stanford, California, August 14-16, 1972.

Nishimura, T., "Modeling Errors in Kalman Filters", AGARDograph 139, Theory and Applications of Kalman Filtering, April 1970, pp. 87-103.

North, R. N., "Separation Standards and Aircraft Wander", Journal of the Institute of Navigation, Vol. 19, No. 2, April 1966.

O'Halloran, W. F. and Warren, R. S., "Design of a Reduced-State Sub-optimum Filter for Self-Calibration of a Terrestrial Inertial Navigation System", AIAA Paper No. 72-849, AIAA Guidance and Control Conference, Stanford, California, August 14-16, 1972.

Palmer, W., "Omega-Inertial Hybrid Receiver", Journal of Institute of Navigation, Vol. 15, No. 4, Winter 1968-1969, pp. 376-390.

Pierce, J. A., et al., "Omega -- A World-Wide Navigational System. System Specification and Implementation", P & B Pub. No. 886B, published by Pickard and Burns, Waltham, Mass., May 1, 1966.

Poritzky, S. B., "The Use of Hybrid Techniques in Commercial Transport Aircraft", AGARD Conference Proceedings No. 54, Guidance and Control Panel 9th Meeting, Delft, Netherlands, September 22-26, 1969.

Quinn, G. H., "FAA Airborne Omega Development Program", The Institute of Navigation, Proceedings of the First Omega Symposium, Washington, D.C., November 9-11, pp. 130-131.

Rey, J. A. and Sakran, F. C., Jr., "The AN/ARN-99 (V) Airborne Omega Navigation Set: Capabilities and Status", The Institute of Navigation, Proceedings of the First Omega Symposium, Washington, D.C., November 9-11, 1971, pp. 89-98.

Savage, P. G. and Hartmann, G. L., "Optimum Aiding of Inertial Navigation Systems Using Air Data", AIAA Paper No. 72-847, AIAA Guidance and Control Conference, Stanford, California, August 14-16, 1972

Schmidt, S. F., "Computational Techniques in Kalman Filtering", AGARD-ograph 139, Theory and Applications of Kalman Filtering, April 1970, pp. 65-86.

Schmidt, S. F., Weinberg, J. D. and Lukesh, J. S., "Application of Kalman Filtering to the C-5 Guidance and Control System", AGARDograph 139, Theory and Applications of Kalman Filtering, April 1970, pp. 283-334.

Smith, E. J., "AN/ARN 99 Method of Removing Omega Lane Ambiguity", The Institute of Navigation, Proceedings of the First Omega Symposium, Washington, D. C., November 9-11, 1971, pp. 75-82.

Sorensen, J. A., Stepner, D. E. and Tyler, J. S., "The Effect of Omega on Oceanic Airway Safety", Proceedings of the First Omega Symposium, Washington, D.C., November 9-11, 1971.

Starr, S. H. and Horowitz, B. M., "Application of Optimal Control Theory to Satellite-Based Air Traffic Control", Navigation: Journal of the Institute of Navigation, Vol. 17, No. 4, Winter 1970-1971, pp. 336-348.

Stepner, D. E., "Modeling of Position Errors with Independent Surveillance", AIAA Paper No. 73-162, AIAA 11th Aerospace Sciences Meeting, Washington, D.C., January 10-12, 1973.

Stepner, D. E. and Tyler, J. S., "The Computation of Position Errors for Air Traffic Control Surveillance Models", AIAA Paper No. 71-927, AIAA Guidance, Control and Flight Mechanics Conference, Hofstra University, August 16-18, 1971.

Stow, R. C. and Danik, B., "Integrated Hybrid-Inertial Aircraft Navigation Systems", AGARD Conference Proceedings No. 54, Guidance and Control Panel 9th Meeting, Delft, Netherlands, September 22-26, 1969.

Stringer, F. S., "The TMA Role of Hybrid System Radio Sensors", AGARD Conference Proceedings No. 54, Guidance and Control Panel 9th Meeting, Delft, Netherlands, September 22-26, 1969.

Stubberud, A. R. and Wismer, D. A., "Suboptimal Kalman Filter Techniques", AGARDograph 139, Theory and Applications of Kalman Filtering, April 1970, pp. 105-117.

Swanson, E. R., "Omega", Navigation: Journal of the Institute of Navigation, Vol. 18, No. 2, Summer 1971, pp. 168-175.

Swanson, E. R. and Tibbals, M. L., "The Omega Navigation System", Navigation, Vol. 12, No. 1, Spring 1965, pp. 24-35.

Swick, R. "Optimal Correction of Stochastic Errors of Inertial Systems", AGARD Conference Proceedings No. 54, Guidance and Control Panel 9th Meeting, Delft, Netherlands, September 22-26, 1969.

Tyler, J. S. and Brown, J. V., "The Estimation of Inertial Guidance Errors", AIAA Paper No. 68-885, AIAA Guidance, Control and Flight Dynamics Conference, Pasadena, California, August 12-14, 1968.

Tymczyszyn, J. J., "Potential Operational Advantages of Low Cost VLF/Omega Navigation Equipment", The Institute of Navigation, Proceedings of the First Omega Symposium, Washington, D. C., November 9-11, 1971, pp. 132-137.

Unger, F. G. and Ott, N., "Optimal Use of Redundant Information in an Inertial Navigation System", AGARDograph 139, Theory and Applications of Kalman Filtering, April 1970, pp. 467-490.

Van Allen, R. L., and Brown, R. G., "An Incremental Velocity Measurement Algorithm for Use in Inertial Navigation Alignment", Technical Report ERI-72-23, Iowa State University, Engineering Research Institute, February 1972.

Waldman, R. H., "Commercial Navigation Systems for Long Range Subsonic Transports in the 1970's", Journal of the Institute of Navigation, Vol. 22, No. 4, October 1969.

Wiggins, D., "An All-Omega System Can Provide Enroute Navigation Today", ICAO Bulletin, March 1973, Vol. 28, No. 3, pp. 14-18.

Weinman, R. W., "Real Time Propagation Prediction for an Airborne Omega System", The Institute of Navigation, Proceedings of the First Omega Symposium, Washington, D. C., November 9-11, 1971, pp. 83-88.

White, A., "Air Traffic Control Separation Minima and Navigational Capability", Journal of the Institute of Navigation, Vol. 24, No. 4, October 1971, pp. 443-456.

Woodford, J. B. and Dutcher, R. L., "A Satellite System to Support an Advanced Air Traffic Control Concept", Proceedings of the IEEE, Vol. 58, No. 3, March 1970, pp. 438-447.

Anon., "Analysis of Organized Route Systems in the North Atlantic", ARCON Corporation Final Report, FAA Contract No. FA-WA-4620, Sept. 1964.

Anon., "An ATC Survey of North Atlantic Navigation Problems", Journal of the Institute of Navigation, Vol. 10, No. 4, August 1965.

Anon., "Phase Difference Navigation Satellite Study", Final Report -- Contract NAS-12-509, Radio Corporation of America, Moorestown, New Jersey, December 1967.

Anon., "Study of a Navigation and Traffic Control Technique Employing Satellites", Interim Report - Contract NAS 12-539, (TRW No. 08710-6012-R000), TRW Systems Group, Redondo Beach, California, December 1967.

Anon., "Study of Future Oceanic Aviation Support Systems", ARCON Corp., Contract No. FA67WA-1680, May 1968.

Anon., "Navigation/Traffic Control Satellite Mission Study", Final Report - Contract NAS 12-596, Radio Corporation of America, Moorestown, New Jersey, December 1968.

Anon., "AINS-70 Area Inertial Navigation System", 523-0763395-0011P, Collins Radio Company, Cedar Rapids, Iowa, October 29, 1970.

Anon., "DRA-12 Doppler Radar System", Bendix Avionics Division, Manual Number 1.B 1012A, rev. January 1971.

Anon., "Omega Table: Area II, North America, Pair C-D", H.O. Pub. No. 224 (11 1) C-D, U.S. Navy Oceanographic Office, 1971.

Anon., "The Endless Signal", FAA Aviation News, March 1972, pp. 6-7.

Anon., "Doppler Navigation and Guidance System: SKK-1000A Doppler Radar and SKQ-601 Computer", Singer Kearfott Division, April 1972.

Anon., "Omega Navigation System - CMA-719(C)", Canadian Marconi Company, Montreal, Canada, May 1972.

APPENDIX A

LATITUDE AND LONGITUDE EXPRESSIONS FOR CONSTANT TRACK ANGLE

This appendix develops analytical expressions for latitude and longitude vs time to maintain a constant ground track between two waypoints. The latitude and longitude are related to the track angle χ by:

$$\dot{L} = \frac{V_N}{r} = \frac{V_g}{r} \cos \chi \tag{A1}$$

$$\dot{\ell} = \frac{V_E}{r \cos L} = \frac{V_g \sin \chi}{r \cos L} \tag{A2}$$

For constant airspeed and wind, the groundspeed V_g is also constant. Neglecting any perturbations in r, Equation (A1) can be integrated directly:

$$L(t) = L_0 + \frac{V_N}{r} (t - t_0) \tag{A3}$$

where the subscript zero denotes the initial conditions. To integrate Equation (A2), first divide by (A1):

$$\frac{d\ell}{dL} = \frac{V_E}{V_N \cos L} \tag{A4}$$

Equation (A4) can now be integrated to obtain, with some manipulation,

$$\ell(t) = \ell_0 + \frac{V_E}{V_N} \ln \left[\frac{(1 + \sin L) \cos L_0}{(1 + \sin L_0) \cos L} \right] \tag{A5}$$

where L = L(t) is obtained from Equation (A3).

To determine the track angle between two waypoints, we have

$$\chi = \tan^{-1} (V_E/V_N) \tag{A6}$$

Using Equation (A5), this becomes

$$\chi = \tan^{-1} \left\{ (\ell - \ell_0)/\ln \left[\frac{(1 + \sin L) \cos L_0}{(1 + \sin L_0) \cos L} \right] \right\} \tag{A7}$$

where the waypoint coordinates are (L_0, ℓ_0) and (L, ℓ).

Equations (A5) and (A7) are indeterminate if $L = L_0$ (i.e. $V_N = 0$). However, in this constant latitude case, Equation (A2) can be integrated directly:

$$\ell(t) = \ell_0 + \frac{V_E}{r \cos L_0} (t - t_0) \tag{A8}$$

The track angle is simply:

$$\chi = \begin{cases} 90^\circ & , \quad \ell > \ell_0 \\ 270^\circ & , \quad \ell < \ell_0 \end{cases} \tag{A9}$$